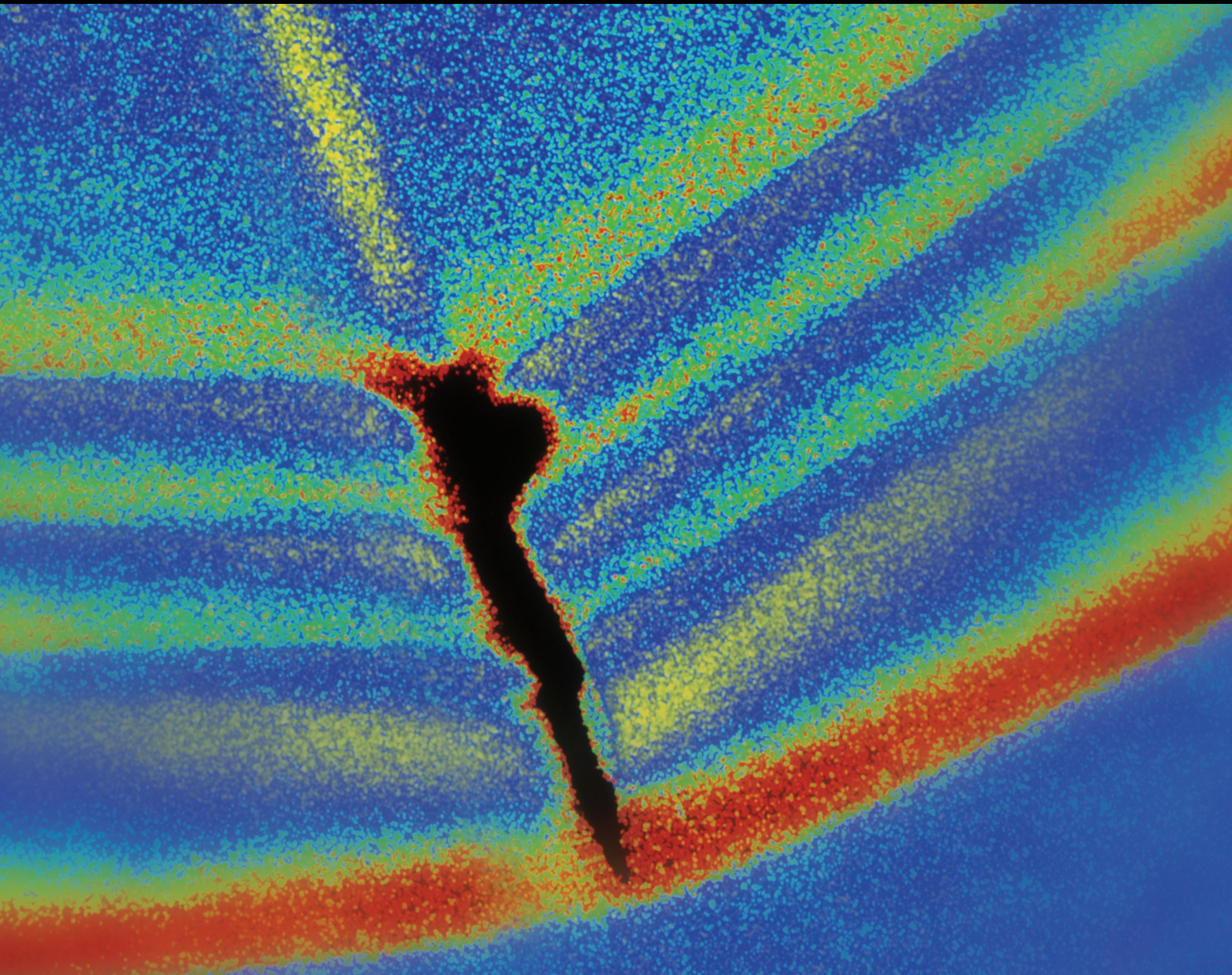


Applications of Magnetorheological Technology to Semiactive Vibration Control Systems

Guest Editors: Miao Yu, Seung-Bok Choi, Weihua Li, Jeong-Hoi Koo, and Xinchun Guan





Applications of Magnetorheological Technology to Semiactive Vibration Control Systems

Shock and Vibration

Applications of Magnetorheological Technology to Semiactive Vibration Control Systems

Guest Editors: Miao Yu, Seung-Bok Choi, Weihua Li,
Jeong-Hoi Koo, and Xinchun Guan



Copyright © 2015 Hindawi Publishing Corporation. All rights reserved.

This is a special issue published in "Shock and Vibration." All articles are open access articles distributed under the Creative Commons Attribution License, which permits unrestricted use, distribution, and reproduction in any medium, provided the original work is properly cited.

Associate Editors

Brij N. Agrawal, USA
Marco Alfano, Italy
Farbod Alijani, Canada
Sumeet S. Aphale, UK
Hassan Askari, Canada
Matteo Aureli, USA
Ranjan Banerjee, UK
José Villanueva, Spain
Subhamoy Bhattacharya, UK
Ivo Caliò, Italy
Antonio Carcaterra, Italy
Dumitru I. Caruntu, USA
Noël Challamel, France
Peng Chen, Japan
Ashwin Chinnayya, France
Giorgio Dalpiaz, Italy
Farhang Daneshmand, Canada
Sergio De Rosa, Italy
Longjun Dong, China
Mohamed El badaoui, France
Mohammad Elahinia, USA
Francesco Franco, Italy
Alessandro Gasparetto, Italy
Anindya Ghoshal, USA

Alicia Gonzalez-Buelga, UK
Hassan Haddadpour, Iran
María I. Herreros, Spain
Hamid Hosseini, Japan
Reza Jazar, Australia
Sakdirat Kaewunruen, UK
Jeong-Hoi Koo, USA
Georges Kouroussis, Belgium
Mickaël Lallart, France
Kenneth J. Loh, USA
Nuno M. Maia, Portugal
Giuseppe C. Marano, Italy
Laurent Mevel, France
Emiliano Mucchi, Italy
Tony Murmu, UK
Sundararajan Natarajan, India
Toshiaki Natsuki, Japan
Miguel Neves, Portugal
Coral Ortiz, Spain
Gyuhae Park, Korea
Evgeny Petrov, UK
Antonina Pirrotta, Italy
Didier Rémond, France
Francesco Ripamonti, Italy

Salvatore Russo, Italy
Edoardo Sabbioni, Italy
Jerzy T. Sawicki, USA
Vadim V. Silberschmidt, UK
Kumar V. Singh, USA
Isabelle Sochet, France
Alba Sofi, Italy
Jussi Sopanen, Finland
Narakorn Srinil, UK
Salvatore Strano, Italy
Chao Tao, China
Mario Terzo, Italy
Tai Thai, Australia
Carlo Trigona, Italy
Federica Tubino, Italy
Nerio Tullini, Italy
Marcello Vanali, Italy
Jörg Wallaschek, Germany
Peijun Xu, USA
Zaili L. Yang, UK
Stana Živanović, UK
Lei Zuo, USA

Contents

Applications of Magnetorheological Technology to Semiactive Vibration Control Systems, Miao Yu, Seung-Bok Choi, Norman M. Wereley, Weihua Li, Jeong-Hoi Koo, and Xinchun Guan
Volume 2015, Article ID 424368, 2 pages

Design of a Real-Time Adaptively Tuned Dynamic Vibration Absorber with a Variable Stiffness Property Using Magnetorheological Elastomer, Toshihiko Komatsuzaki and Yoshio Iwata
Volume 2015, Article ID 676508, 11 pages

Magnetic Circuit Analyses and Turning Chatter Suppression Based on a Squeeze-Mode Magnetorheological Damping Turning Tool, Yongliang Zhang, Norman M. Wereley, Wei Hu, Ming Hong, and Wei Zhang
Volume 2015, Article ID 304698, 7 pages

Wavelet Adaptive Algorithm and Its Application to MRE Noise Control System, Zhang Yulin and Zhao Xiuyang
Volume 2015, Article ID 968082, 8 pages

Damping Force Tracking Control of MR Damper System Using a New Direct Adaptive Fuzzy Controller, Xuan Phu Do, Kruti Shah, and Seung-Bok Choi
Volume 2015, Article ID 947937, 16 pages

Adaptive Vibration Control System for MR Damper Faults, Juan C. Tudón-Martínez and Ruben Morales-Menendez
Volume 2015, Article ID 163694, 17 pages

Thermodynamic Behaviors of a Kind of Self-Decoupling Magnetorheological Damper, Guojun Yu, Chengbin Du, and Tiger Sun
Volume 2015, Article ID 502747, 9 pages

Frequency Dependent Spencer Modeling of Magnetorheological Damper Using Hybrid Optimization Approach, Ali Fella Jahromi, Rama B. Bhat, and Wen-Fang Xie
Volume 2015, Article ID 382541, 8 pages

Editorial

Applications of Magnetorheological Technology to Semiactive Vibration Control Systems

Miao Yu,¹ Seung-Bok Choi,² Norman M. Wereley,³ Weihua Li,⁴
Jeong-Hoi Koo,⁵ and Xinchun Guan⁶

¹Department of Optoelectronics, Chongqing University, Chongqing 400044, China

²Smart Structures and Systems Laboratory, Department of Mechanical Engineering, Inha University, Incheon 402-751, Republic of Korea

³Department of Aerospace Engineering, University of Maryland, College Park, MD 20742, USA

⁴School of Mechanical, Materials and Mechatronic Engineering, University of Wollongong, Wollongong, NSW2522, Australia

⁵Department of Mechanical and Manufacturing University, Miami University, Oxford, OH 45056, USA

⁶School of Civil Engineering, Harbin Institute of Technology, Harbin, China

Correspondence should be addressed to Miao Yu; yumiao@cqu.edu.cn

Received 12 May 2015; Accepted 12 May 2015

Copyright © 2015 Miao Yu et al. This is an open access article distributed under the Creative Commons Attribution License, which permits unrestricted use, distribution, and reproduction in any medium, provided the original work is properly cited.

Semiactive vibration control systems possess both the simplicity and inherent reliability of passive systems while maintaining the adaptability of active vibration control systems integrated with an appropriate control algorithm. One of the recent and promising technologies in semiactive vibration control is to utilize magnetorheological (MR) fluids (MRFs) [1] and MR elastomers (MREs) [2]. The well-known remarkable feature of MR materials is the continuous controllability of stiffness and damping properties under external magnetic field. The unique controllable characteristic of MR materials has catalyzed comprehensive research and development focusing on vibration control systems including vehicle dampers, engine mounts, adaptive tuned vibration absorber, and seismic bearings [3–10]. The major goal of this special issue is to provide recent research in applications utilizing MR materials. In particular, the special issue focuses on the MR techniques that deal with configuration design, dynamic modeling, and semiactive controller implementation along with simulation or/and experimental works. Therefore, the papers published in this special issue will be innovative references for the development of more advanced application devices or systems utilizing MR materials.

In this special issue, all the papers have been accepted and published after strict review process by the worldwide

experts on the MR materials technology. The published papers cover characteristic analysis and design of the devices, new modeling approaches, and control algorithms used in vibration control systems. A brief summary of each application proposed in the published papers is given as follows.

J. C. Tudon-Martinez and R. Morales-Menendez proposed a new adaptive vibration control system (AVCS) based on the linear parameter-varying (LPV) control theory to reduce the lack of damping force of MR damper particularly caused by oil leakages and compared the estimation error of the fault with the model of damping force in which the static equations are used. Y. Zhang et al. presented an MR damping turning tool based on the squeeze-mode to improve the vibration resistance of the tool system on the lathe in which the parameters of MR damper were chosen by the 3D finite element simulations. The effectiveness of MR damping turning tool was verified by undertaking the chattering suppressive experiment. A. F. Jahromi et al. proposed a frequency dependent MR damper model where the viscosity of MR damper was modeled by exponential and Gaussian functions. They experimentally investigated the accuracy and consistency of the model in force simulation. G. Yu et al. developed a self-decoupling magnetorheological damper and established a theoretical model based on

conservation of energy and the constraint equation. They also explored the influence of temperature changes on the damper performance. T. Komatsuzaki and Y. Iwata applied a frequency-tunable dynamic absorber which was fabricated with MRE to the vibration control of a one-DOF structure, controlled with a real-time stiffness switching algorithm. They compared the damping performance with the passive-type absorber. X. P. Do et al. developed a new direct adaptive fuzzy controller based on a model of interval type 2 fuzzy and H^∞ tracking techniques and the effectiveness of controller was verified by investigating the field-dependent damping force and the stable robustness of MR damper system. Z. Yulin and Z. Xiuyang proposed the decomposition least mean square (LMS) algorithm and reconstruction LMS algorithm based on Wavelet. The noise reduction performance of the proposed algorithms was compared with traditional LMS algorithm by application to MRE noise control system.

Acknowledgments

We very much appreciate all the authors' excellent contributions to this special issue and the reviewers' efforts to strictly examine the submitted papers.

Miao Yu
Seung-Bok Choi
Norman M. Wereley
Weihua Li
Jeong-Hoi Koo
Xinchun Guan

References

- [1] M. Yu, X. M. Dong, S. B. Choi, and C. R. Liao, "Human simulated intelligent control of vehicle suspension system with MR dampers," *Journal of Sound and Vibration*, vol. 319, no. 3–5, pp. 753–767, 2009.
- [2] Y. C. Li, J. C. Li, T. F. Tian, and W. H. Li, "A highly adjustable magnetorheological elastomer base isolator for applications of real-time adaptive control," *Smart Materials and Structures*, vol. 22, no. 9, Article ID 095020, 2013.
- [3] P. F. Guo, X. C. Guan, and J. P. Ou, "Physical modeling and design method of the hysteretic behavior of magnetorheological dampers," *Journal of Intelligent Material Systems and Structures*, vol. 25, no. 6, pp. 680–696, 2014.
- [4] M. Yu, B. X. Ju, J. Fu, X. Liu, and Q. Yang, "Influence of composition of carbonyl iron particles on dynamic mechanical properties of magnetorheological elastomers," *Journal of Magnetism and Magnetic Materials*, vol. 324, no. 13, pp. 2147–2152, 2012.
- [5] S.-B. Choi, M.-H. Nam, and B.-K. Lee, "Vibration control of a MR seat damper for commercial vehicles," *Journal of Intelligent Material Systems and Structures*, vol. 11, no. 12, pp. 936–944, 2001.
- [6] M. Yu, C. R. Liao, W. M. Chen, and S. L. Huang, "Study on MR semi-active suspension system and its road testing," *Journal of Intelligent Material Systems and Structures*, vol. 17, no. 8–9, pp. 801–806, 2006.
- [7] Y.-T. Choi and N. M. Wereley, "Semi-active magnetorheological refueling probe systems for aerial refueling events," *Smart Materials and Structures*, vol. 22, no. 9, Article ID 092001, 2013.
- [8] H. Mansour, S. Arzanpour, M. F. Golnaraghi, and A. M. Parameswaran, "Semi-active engine mount design using auxiliary magneto-rheological fluid compliance chamber," *Vehicle System Dynamics*, vol. 49, no. 3, pp. 449–462, 2011.
- [9] Y. Zhou, W. H. Li, and M. N. S. Hadi, "Performance comparison between an MRF damper and an MRE isolator incorporated with a building structure," *Applied Mechanics and Materials*, vol. 37–38, pp. 862–865, 2010.
- [10] S.-H. Eem, H.-J. Jung, and J.-H. Koo, "Application of MR elastomers for improving seismic protection of base-isolated structures," *IEEE Transactions on Magnetics*, vol. 47, no. 10, pp. 2901–2904, 2011.

Research Article

Design of a Real-Time Adaptively Tuned Dynamic Vibration Absorber with a Variable Stiffness Property Using Magnetorheological Elastomer

Toshihiko Komatsuzaki and Yoshio Iwata

Institute of Science and Engineering, Kanazawa University, Kakuma-machi, Kanazawa, Ishikawa 920-1192, Japan

Correspondence should be addressed to Toshihiko Komatsuzaki; toshi@se.kanazawa-u.ac.jp

Received 21 October 2014; Accepted 10 December 2014

Academic Editor: Miao Yu

Copyright © 2015 T. Komatsuzaki and Y. Iwata. This is an open access article distributed under the Creative Commons Attribution License, which permits unrestricted use, distribution, and reproduction in any medium, provided the original work is properly cited.

An elastomer composite with controllable stiffness, known as a magnetorheological elastomer (MRE), is used in a dynamic vibration absorber whose natural frequency is tuned adaptively to the disturbance frequency through the application of an external magnetic field. The field-dependent property test of the fabricated MRE sample shows that the stiffness changes by more than six times compared to the baseline property value at a 40% iron powder volume concentration. The MRE is then used to fabricate a frequency-tunable dynamic absorber for mitigating transient vibrations of a one-degree-of-freedom system. Investigations show that the proposed absorber outperforms a conventional passive-type absorber throughout the tunable frequency range.

1. Introduction

A passive-type dynamic vibration absorber (DVA) is basically a mass-spring system that suppresses the vibration of a structure at a particular frequency. Since the natural frequency of the DVA is usually tuned to a frequency of particular excitation, the DVA is especially effective when the excitation frequency is close to the natural frequency of the structure. Fixing the physical properties of the DVA limits the application to a narrowband, harmonically excited vibration problem. The design of the absorber, adhering to a well-known optimal tuning and damping theory, can extend the effective frequency range [1]. However, the damping performance remains at a certain level irrespective of whether the vibration is harmonic or not, and the performance may become worse for vibrations caused by transient disturbances. A frequency-tunable DVA that can modulate its stiffness provides adaptability to the vibration control device against nonstationary disturbances. Several studies have been reported in this regard [2–5] but the implementation of such adaptability would be complex and the response time may become a design issue.

The magnetorheological elastomer (MRE) belongs to the class of smart materials whose elastic property can be varied according to an externally applied magnetic field. The robustness and structural simplicity, stiffness variability, and fast response properties of MREs hold promise for the new design of semiactive adaptive vibration control devices, following numerous publications of a number of studies on this topic [6–16].

Komatsuzaki et al. [6] and Liao et al. [7] have developed an MRE-based vibration isolator where real-time semiactive vibration control techniques are applied in order to reduce vibration in the structure or the payload. Previously published studies also include development of the adaptive absorbers using MREs. Deng and Gong [8] have proposed a tunable dynamic absorber using MRE where a natural frequency shift of 155% could be obtained when a magnetic field of 1 T was applied that consequently damped the beam vibration effectively. Lerner and Cunefare [9] have studied MRE-based vibration absorbers in which MREs are deformed under three different configurations. They have found the configuration and the iron concentration of MREs that maximize the natural frequency shift of the absorber.

While extending the frequency shift property of the absorber, possible influences on the damper performance of the ratio of the primary and the adjacent masses, the tunable range modulations, and the damping property of the material itself have not yet been elucidated. Furthermore, these prior studies have been completed under a harmonic disturbance condition that is less likely to be observed in real applications such as the transient vibration in vehicles. On this issue, Hoang et al. [10] have analytically investigated the real-time control of transient vibration in vehicular power trains using an MRE-based, adaptively tuned dynamic absorber; however, the implementation of such a scheme to the actual equipment has not been realized thus far.

In this paper, an effective design of the adaptively tuned dynamic absorber is shown against the target structure in order to maximize the performance of the absorber with a frequency-tunable feature. The performance of the proposed MRE-based DVA is evaluated by comparison to a passive-type absorber with fixed properties. Additionally, the study aims to show numerically as well as experimentally that the real-time adaptive control is quite possible for a transient vibration caused by excitation, whose frequency changes with time. Field-dependent properties of the fabricated MREs are first shown. The MREs are then introduced into a DVA whose frequency adjustability is evaluated. Finally, the real-time vibration control performance of the frequency-tunable absorber for a base-excited, one-degree-of-freedom system is evaluated. Investigations show that the vibration of the structure can be effectively reduced with an improved performance by the DVA in comparison to the conventional passive-type absorber.

2. Description of Magnetorheological Elastomer

A magnetorheological fluid (MRF) is a well-known kind of functional material, where the ferromagnetic particles—whose size is usually distributed between 1 and 10 μm —are homogeneously dispersed within the carrier fluid, in the absence of an external magnetic field. Under the presence of a magnetic field, magnetically polarized particles form chain-like structures according to the attractive forces amongst each other that produce changes in the apparent viscosity of the fluid. A number of engineering applications are investigated regarding the fluid owing to its highly variable and responsive properties [17, 18]. However, the fluid causes several problems, such as sealing, sedimentation, or aggregation of particles.

The elastomer composites incorporating ferrous particles, known as MREs, have been developed with the aim of overcoming the problems associated with the fluid. Fixation of iron particles within the elastomeric matrix provides MREs with acquired advantages when installed as mechanical elements, in which the sedimentation problems can be avoided and the sealing problems can be neglected. Moreover, their shape is sustained permanently and it is easily molded to fit various configurations. On the other hand, the particles are

strongly immobilized and therefore the characteristic variation range in MREs usually becomes smaller compared to MRFs. It should also be noted that the MRE is characterized by an elastic property rather than a viscous property and hence a viscoelastic evaluation is necessary.

Several studies have been reported regarding MREs [6–16]. Prior research work includes a fundamental investigation of the material in order to improve the property variation range of MREs. For example, Gong et al. [12] have studied isotropic MREs where the silicone oil was introduced in the mixture of silicone rubber and iron particles to improve mobility of particles within the elastomeric material, and their shear storage modulus was evaluated by changing their compositions. Zhang et al. [13] have proposed the fabrication process to form the patterned structure within MREs and have investigated the structural effect on their stress-strain relationship. Others have numerically predicted the mechanical response of MREs in the presence of a magnetic field, as described in [14–16]. It seems that a well-defined fabrication process, a reliable evaluation, and the analytical models of MREs have not yet been determined. However, MREs are obviously the prospective materials for new engineering applications especially in the field of mechanical and structural vibrations.

2.1. Fabrication of MRE. The fabricated MRE samples are composed of carbonyl iron powder of an approximate diameter of 10 μm dispersed within the room-temperature-vulcanizing (RTV) rubber matrix. They are fabricated based on the expertise acquired in earlier studies [12, 13]. The stiffness of the elastomeric matrix should be kept low to ensure a range in property variation when exposed to an external magnetic field. Additionally, the application of the magnetic field during the curing process of MRE is known to be effective for expanding the shear modulus variation. Elastomers are formed in square cuboids with a size of 25 mm and a thickness of 10 mm and with different iron volume contents ranging from 30 to 50%.

2.2. Dynamic Property Test. The viscoelastic properties of the fabricated MREs are investigated by measuring their dynamic response using the experimental setup shown in Figure 1. The upper part of the electromagnet (whose mass is 1.56 kg) and two MREs placed between the upper and the lower parts of the electromagnet are assumed to emulate a mass and two springs, respectively, and they constitute a one-degree-of-freedom (DOF) vibration system. While exciting the system horizontally by an exciter, the base and mass accelerations are measured and processed in the form of a transfer function by an FFT analyzer. The frequency response of the system is measured through a random excitation at the cutoff frequency of 100 Hz, while the applied electric current is varied from 0 to 4 A.

Based on the measured acceleration transfer function, the complex spring constant is calculated according to the

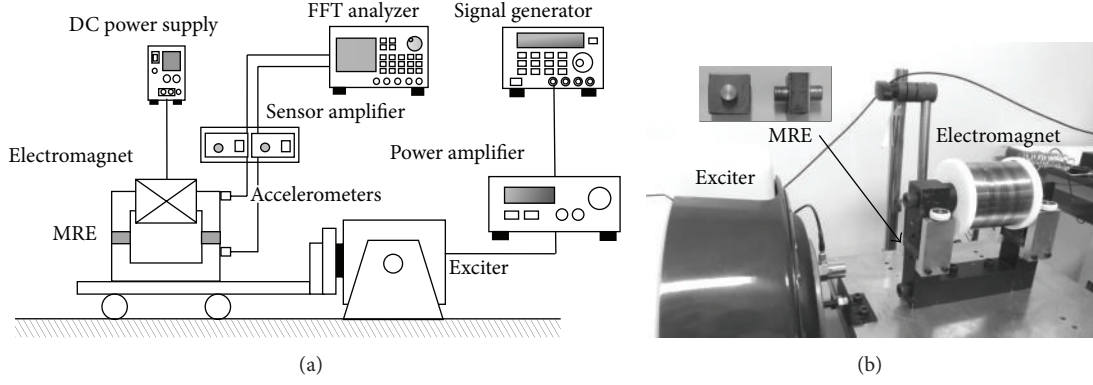


FIGURE 1: Viscoelastic property measurement system: (a) schematic and (b) photograph.

TABLE 1: The identified spring constants of MREs listed against applied current. All values are represented in units of N/mm. Numbers shown in parentheses are the elastic shear moduli in MPa.

MRE composition	Current				
	0 A	1 A	2 A	3 A	4 A
30 vol% MRE	17.1 (0.27)	27.3 (0.44)	40.3 (0.65)	54.3 (0.87)	62.4 (1.00)
40 vol% MRE	28.5 (0.46)	53.9 (0.86)	91.8 (1.47)	135 (2.15)	157 (2.51)
50 vol% MRE	62.2 (1.00)	98.2 (1.57)	163 (2.61)	254 (4.06)	301 (4.81)

following equation. The equation of motion of the one-DOF system is thus written as

$$m\ddot{x} = -k^*(x - u), \quad (1)$$

where the symbols x , u , m , and k^* represent the displacement of the system, the displacement of the shaking table, the mass, and the complex spring constant, respectively. Introduction of the relative displacement, y , between the mass and the shaking table leads to a modified form of (1) as follows:

$$m\ddot{y} + k^*y = -m\ddot{u}. \quad (2)$$

The frequency-dependent complex spring constant, k^* , is defined in accordance with the following manner:

$$k^*(\omega) = k_0 \cdot v(\omega) \{1 + j\eta(\omega)\}. \quad (3)$$

In (3), k_0 signifies the reference spring constant calculated by the natural frequency ω_0 of the system when no magnetic field is applied, $v(\omega)$ is the frequency-dependent normalized spring constant, and $\eta(\omega)$ is the loss factor. From (2) and (3), the acceleration transfer function is derived according to the following equation [19]:

$$G(j\omega) = \frac{v(\omega) + j\eta(\omega)v(\omega)}{\{v(\omega) - \lambda^2\} + j\eta(\omega)v(\omega)}. \quad (4)$$

In (4), $\lambda = \omega/\omega_0$. By separating the real and the imaginary parts of the transfer function as $G(j\omega) = G_R + jG_I$, $v(\omega)$ and $\eta(\omega)$ can be expressed using G_R and G_I , as

$$\begin{aligned} v(\omega) &= \frac{G_R(G_R - 1) + G_I^2\lambda^2}{(G_R - 1)^2 + G_I^2}, \\ \eta(\omega) &= \sqrt{-1 + \frac{(2G_R - 1)\lambda^2}{(G_R - 1)v(\omega)} - \frac{G_R\lambda^4}{(G_R - 1)v(\omega)^2}}. \end{aligned} \quad (5)$$

Figure 2 shows the viscoelastic property of MREs at different iron concentrations. The normalized stiffness and the loss factor are calculated using (5) for each sample. Both properties are almost independent of frequency in all cases. In this study, the nominal value of the spring constant in the absence of a magnetic field is 15.9 N/mm for an MRE of 30% iron volume content (vol%), 24.6 N/mm for that with a 40 vol%, and 58.2 N/mm for that with a 50 vol%. Based on the nominal value, the identified stiffness values for each MRE and for various applied currents are listed in Table 1. Indicated values are averaged over the frequency range of 20 to 80 Hz. The normalized stiffness has the lowest value when no magnetic field is applied, and it becomes larger in value according to the strength of the field owing to the increase in interparticle forces within the elastomeric matrix. On the other hand, the change of the loss factor seems to be small enough in comparison to the change of the stiffness, irrespective of the presence of the magnetic field, whose value becomes approximately 0.4 in all cases. Such a high damping value is attributed to the viscous property of the host elastomer. The same holds true for the average

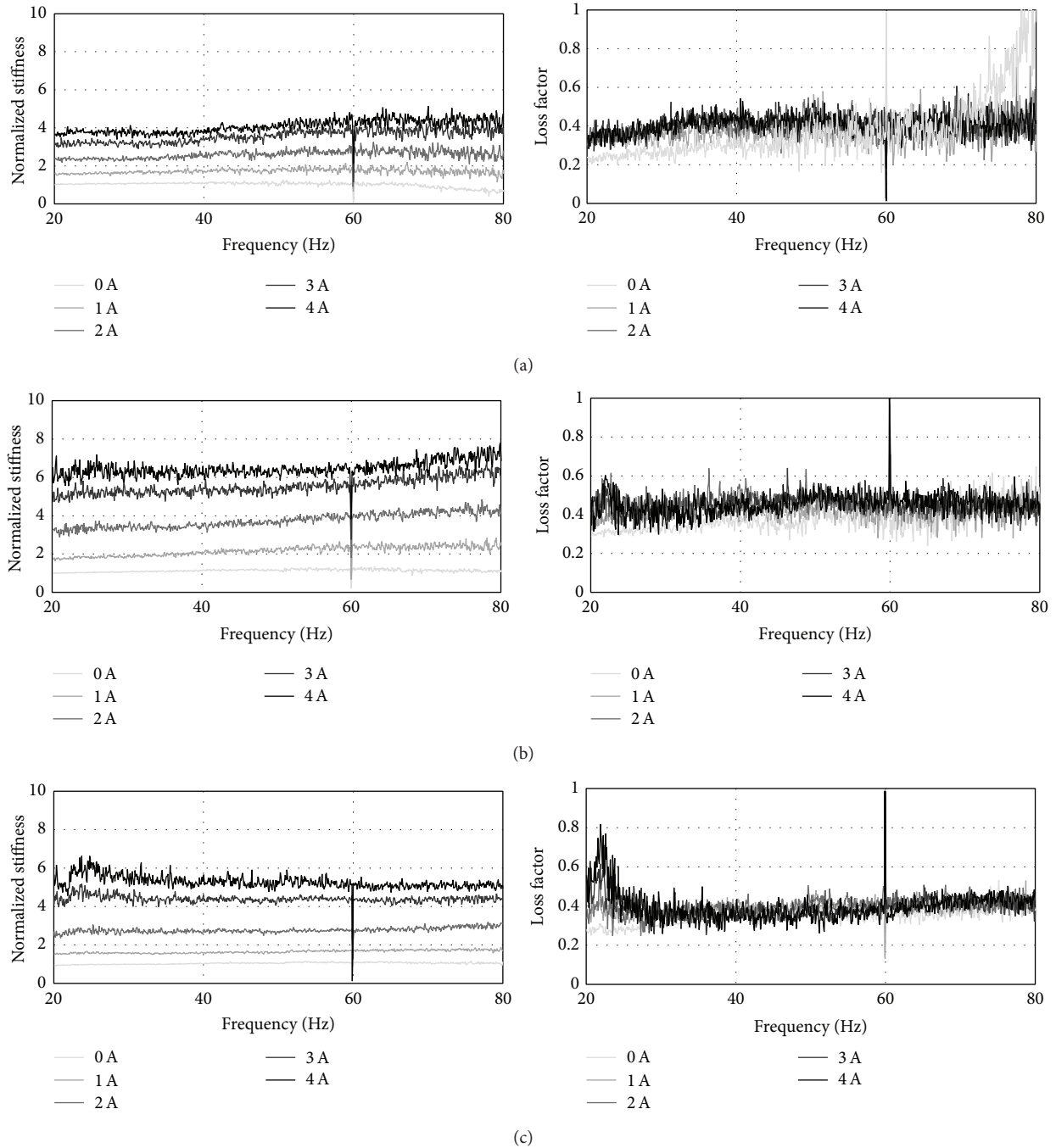


FIGURE 2: Complex stiffness constant of magnetorheological elastomer (MRE) samples: (a) MRE of 30 vol% iron content, (b) 40 vol%, and (c) 50 vol%. The left figures in the left column show the normalized spring constant and the figures in the right column show the loss factor.

stiffness magnification and the loss factor shown in Figure 3. Additionally, the maximum stiffness variation is observed for the MRE sample with 40 vol% iron content. The higher volume content of iron particles leads to the expression of the stronger interparticle forces, whereas the base hardness of the elastomer itself also becomes high. Hence, the largest magnification of stiffness is provided by a certain optimum composition between the elastomeric matrix and the iron particles.

3. Numerical Prediction of Performance of the Dynamic Absorber

In this section, the damping performance of a dynamic absorber with a variable stiffness is numerically predicted for a harmonically excited response of a two-DOF vibration system incorporating the absorber, where the tuning capacity is based on the measured property of the prototypes.

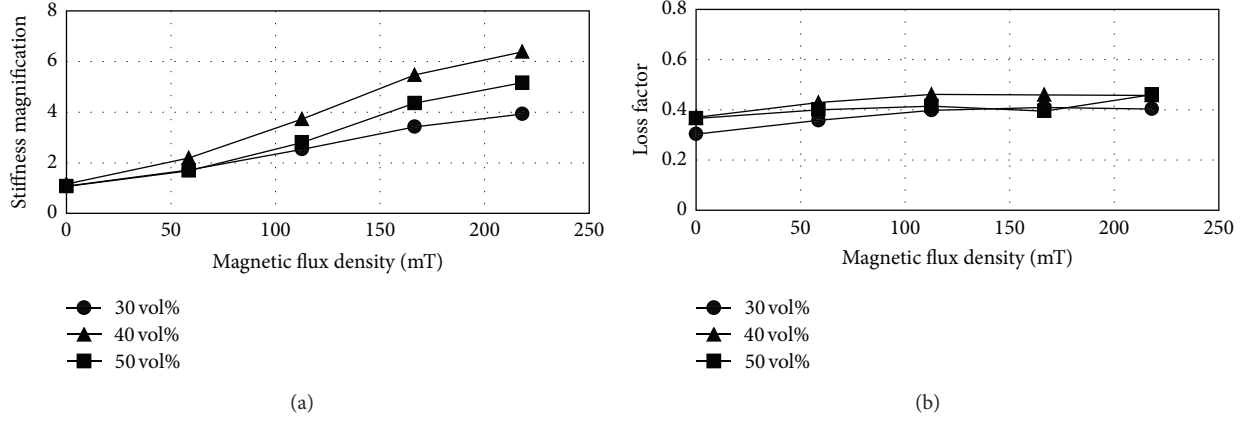


FIGURE 3: Average stiffness magnification and loss factor of magnetorheological elastomers (MREs) plotted against the magnetic flux density: (a) the stiffness variation and (b) the loss factor variation.

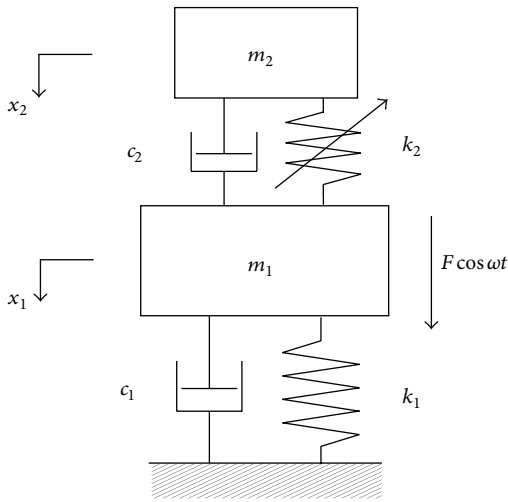


FIGURE 4: Analytical model of dynamic absorber with variable stiffness attached to a primary system.

3.1. Numerical Model of Two-DOF System Including a Variable Stiffness Absorber. A mathematical model of a two-DOF vibration system consisted of a primary system and a secondary system, and having a variable stiffness property, as shown in Figure 4. The primary system, having a mass of m_1 , a spring constant, k_1 , and a damping coefficient, c_1 , is excited harmonically by the external force $F \cos \omega t$, whereas the stiffness variability is assigned to the spring element, k_2 , of the adjacent system, whose property changes according to the actual measured characteristic. Assuming that the stiffness k_2 is constant, the equations of motion for the two-DOF system are written as follows, using symbols shown in Figure 4:

$$\begin{aligned} m_1 \ddot{x}_1 + (c_1 + c_2) \dot{x}_1 + (k_1 + k_2) x_1 \\ - c_2 \dot{x}_2 - k_2 x_2 &= F \cos \omega t, \\ m_2 \ddot{x}_2 + c_2 \dot{x}_2 + k_2 x_2 - c_2 \dot{x}_1 - k_2 x_1 &= 0. \end{aligned} \quad (6)$$

Equation (6) is further transformed into a nondimensional form with respect to time and displacement, in order to illustrate the effect of the variable frequency range on the damping performance in a qualitative manner. By dividing the real displacements and time by the characteristic length $x_{st} = F/k_1$ and the characteristic time $T_c = \sqrt{m_1/k_1}$, a nondimensional form of (6) is derived as follows:

$$\begin{aligned} \ddot{p} + 2(\zeta_1 + \mu z \zeta_2) \dot{p} + (1 + \mu z^2) p \\ - 2\mu z \zeta_2 \dot{q} - \mu z^2 q &= \cos \Omega \tau, \\ \ddot{q} + 2z \zeta_2 (\dot{q} - \dot{p}) + z^2 (q - p) &= 0. \end{aligned} \quad (7)$$

The parameters in (7) are defined as $\Omega = \omega/\omega_1$, $z = \omega_2/\omega_1$, $p = x_1/x_{st}$, $q = x_2/x_{st}$, $\omega_1^2 = k_1/m_1$, $\omega_2^2 = k_2/m_2$, $\mu = m_2/m_1$, $\zeta_1 = c_1/2\sqrt{m_1 k_1}$, and $\zeta_2 = c_2/2\sqrt{m_2 k_2}$.

3.2. Optimal Design of the Damped Dynamic Vibration Absorber. The optimal tuning and damping theory is well known for the design of the fundamental mass-linear spring type, damped dynamic absorber [1]. In the subsequent section, the performance of the variable tuned absorber is compared with the performance of the optimally tuned absorber with fixed properties. Defining the mass ratio between the primary and the adjacent systems as μ , the conclusive form of the optimally tuned condition is expressed as follows:

$$\frac{\omega_2}{\omega_1} = \frac{1}{1 + \mu}. \quad (8)$$

Additionally, the optimal damping ratio, ζ_{opt} , with respect to the damped vibration absorber is determined by (9), where the maximum amplitude of the primary system response curve is found at either location of two fixed points:

$$\zeta_{opt} = \sqrt{\frac{3\mu}{8(1 + \mu)^3}}. \quad (9)$$

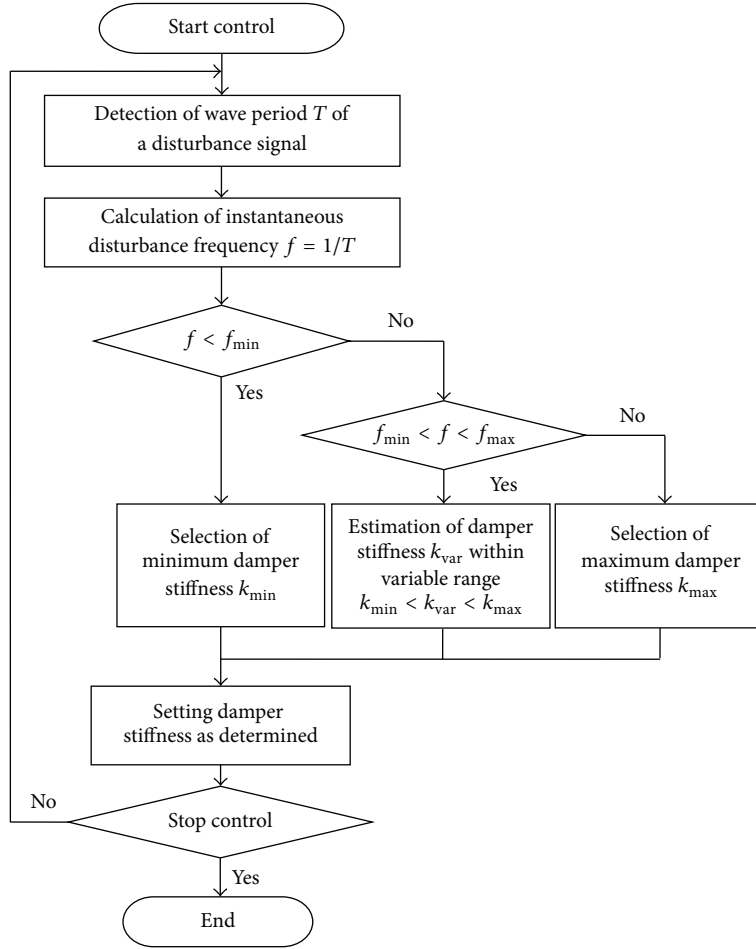


FIGURE 5: Flow diagram of the stiffness switching rules for the tuned dynamic absorber.

3.3. *Calculated Response of Two-DOF System Incorporating Variable Stiffness Absorber.* Based on the nondimensional (7) and on the measured frequency variation range of the absorber (that will be described later), the damping performance of the absorber with variable stiffness is numerically predicted. In the calculation, three different mass ratios $\mu = 0.1, 0.2,$ and 0.3 are configured. The variable frequency range of the absorber for each mass ratio is shown in Table 2 in conjunction with the optimal design parameters of the case with fixed property. Considering that the actual frequency-tunable range extended to 1.4 times the baseline value, the natural frequency of a one-DOF system is located at the middle of the range when the absorber is fixed rigidly to the primary system. As shown in Figure 5, the natural frequency of the adjacent system is tuned adaptively to match the frequency of a harmonic external force within the variable range, whereas the damper property is fixed at the minimum or the maximum stiffness value for the lower and upper outer bounds.

Figure 6 shows the primary system response for the case of a mass ratio $\mu = 0.2$, when the external harmonic force is applied to the primary system as an input. The response amplitudes are expressed in nondimensional form using

the static deflection $\delta_0 = F/k_1$. In this figure, the optimally tuned damper response is also shown. It is shown from the figure that the overall response for the variable stiffness case can be minimized. Each tuned frequency of the response curve approximately corresponds to the frequency of the antinode of the primary system response at the respective damper stiffness variations, within the tunable frequency range. On the other hand, in the case of an optimally tuned absorber, the amplitude of the response curve remains at the level of the amplitude of the two fixed points within the target frequency range.

The responses of the variable stiffness absorbers at three different mass ratios are further compared in Figure 7. Even though the overall response can be improved, a distinct peak will appear for the case of a mass ratio of 0.1. If the mass of the adjacent system is relatively small while the damping ratio is kept constant, the response at the antinode cannot be fully reduced. In contrast, the primary system can be damped more effectively by increasing the damper mass. The response can be improved by reducing the damping ratio of the absorber by combining the MRE with other lightly damped high-stiffness elements, such as metals, or by setting the appropriate mass ratio in the vicinity of 0.2.

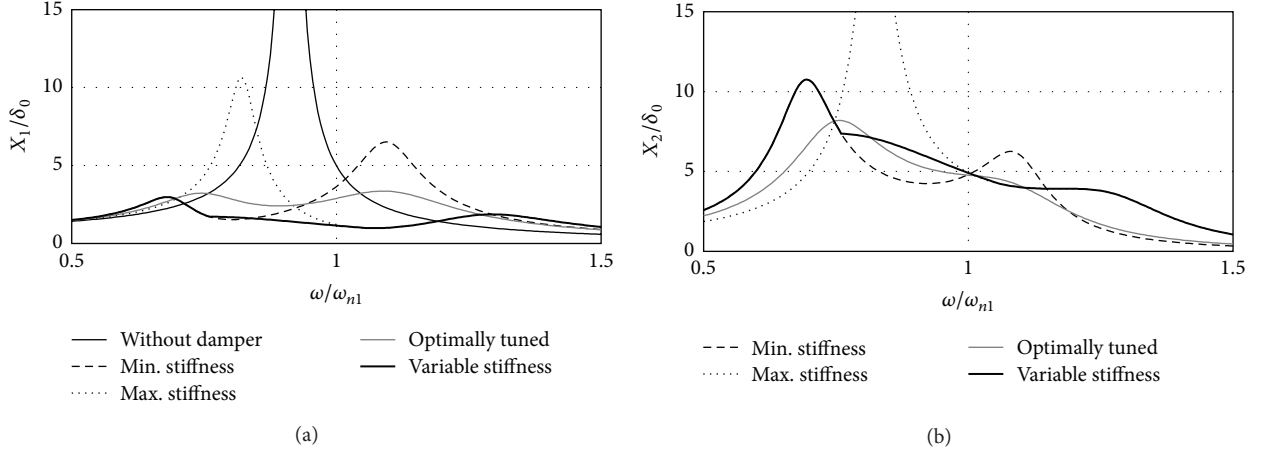


FIGURE 6: Calculated frequency response of a two-degree-of-freedom (DOF) system under harmonic excitation: (a) the primary system and (b) the stiffness-variable dynamic vibration absorber.

TABLE 2: System parameter used in numerical calculation.

Mass ratio (absorber/primary)	0.1	0.2	0.3
Tuned frequency ratio (absorber/primary)	0.91	0.83	0.77
Optimal damping ratio (for absorber)	0.17	0.21	0.23
Frequency ratio (when absorber is immobilized)	0.95	0.91	0.88
Variable frequency range of absorber	0.79–1.11	0.76–1.06	0.73–1.03
Damping ratio (primary system)		0.008	
Damping ratio (absorber)		0.12	

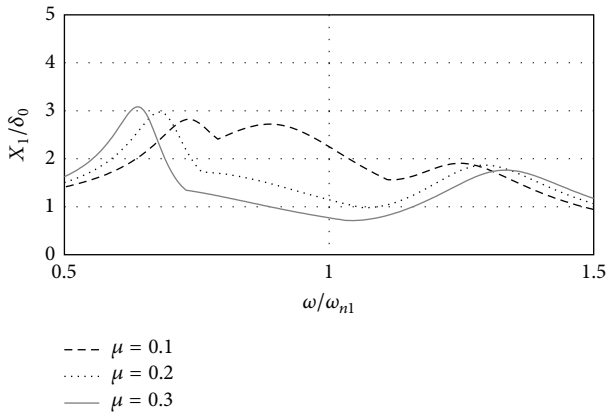


FIGURE 7: Frequency responses of a primary system compared by mass ratio between the primary and the secondary masses.

4. Development of a Dynamic Absorber with Variable Stiffness Using MRE

4.1. Fundamental Property of the Dynamic Absorber. A frequency-tunable DVA is further developed using the aforementioned MRE. A photograph of the dynamic absorber incorporating the MRE as a variable stiffness element is shown in Figure 8. The outer frame is made of steel and constitutes a closed magnetic path. A magnetic coil located at the center works as the mass (370 g) of the absorber that also generates the magnetic flux. Two MREs with thicknesses

of 10 mm and diameters of 20 mm are mounted on the upper and lower parts of the coil so that the stiffness will change owing to the magnetic flux penetration. A 1 mm diameter wire is used to wind the coil with five hundred and forty turns.

The ability of the proposed absorber to change both natural frequency and damping ratio against the applied magnetic field was evaluated. The impulse response of the absorber was measured in the form of a time history at each applied current varying from 0 to 4 A, and the natural frequency and the damping ratio are then calculated.

The measurement results of the fundamental properties of the dynamic absorber with variable stiffness are summarized in Figure 9 and Table 3, for each type of absorber with MREs of different iron concentrations. In the case of MRE with 40 vol% iron content, the largest natural frequency magnification ratio is observed. In this case, the baseline frequency of 25.8 Hz in the absence of a magnetic field is extended by a factor of 1.4 when a 4 A current is applied. In addition to the fact that the induced magnetic flux density at the same level of the applied current is about half of the density induced in the dynamic property test apparatus, all of the tightness of joints among elastomers, the core frame, and the electric coil affect the resulting frequency variation characteristics. On the other hand, the observed damping ratio is thought to have a constant value of 0.12 on average.

4.2. Investigation of the Damping Performance of the Real-Time Tuned Dynamic Absorber. Based on the numerical prediction and the measured results of the fundamental

TABLE 3: Tunable frequency range of the dynamic absorber with variable stiffness.

Iron concentration	Frequency variation range [Hz]	Bandwidth [Hz]	Magnification to the baseline	Damping ratio
30 vol%	21.1–29.2	8.1	1.38	0.13
40 vol%	25.8–36.0	10.2	1.39	0.12
50 vol%	36.6–46.8	10.2	1.28	0.18

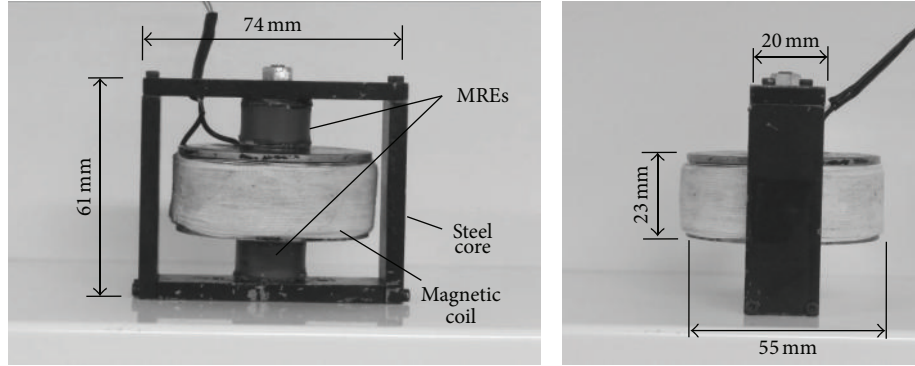


FIGURE 8: Schematic of the dynamic absorber with variable stiffness.

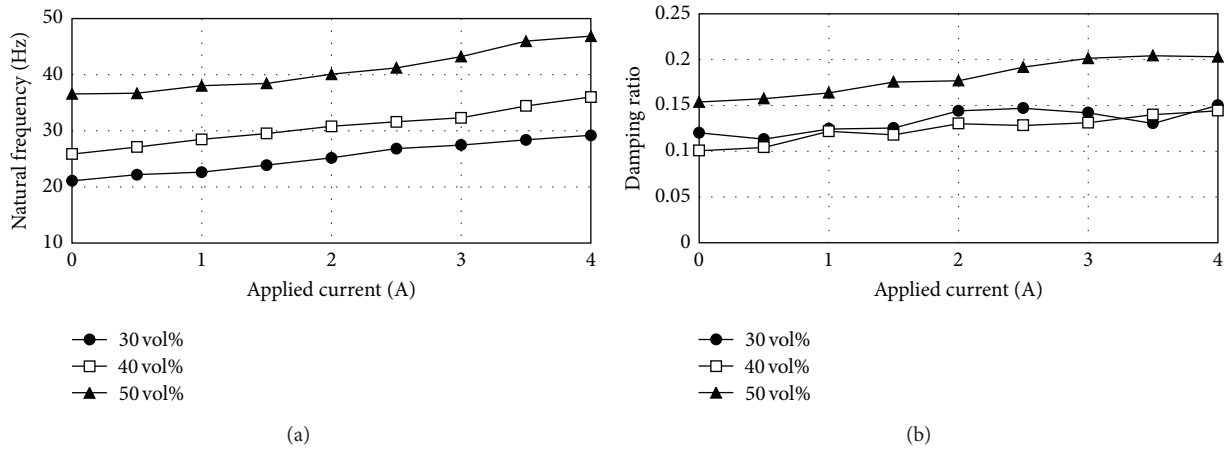


FIGURE 9: Fundamental property of the dynamic absorber with variable stiffness: (a) natural frequency variation and (b) damping ratio variation.

property of the absorber with variable stiffness, the damping performance is experimentally evaluated for the vibration control of a one-DOF system, as shown in Figure 10. The absorber incorporating an MRE with 40 vol% iron content is adopted. The ratio between the primary and the damper masses is chosen to be 0.25. The damping ratio of the primary system alone is also found to be 0.01. Since it is difficult to assign the optimal damping property to the absorber for the present configuration, the optimally damped case is not considered in the experiment. The transient response of the system is measured when the entire structure is excited by a swept-sine input at the shaking table, whose frequency varies from 10 to 50 Hz at the speed of 2 Hz/s. The block diagram of the real-time control scheme is shown in Figure 11. The same real-time stiffness switching rule is applied as in the case of the numerical model.

The frequency responses obtained by the experiment are shown in Figure 12. The curve with a single resonant peak in Figure 12(a) corresponds to the case where the absorber mass is rigidly fixed to the primary structure, whereas the other solid lines correspond to responses when the damper stiffness is fixed at the respective applied currents. The remaining curve with dashed lines represents the response when the natural frequency of the absorber is adaptively tuned to the instantaneous frequency of the disturbance. The figure shows that the tunable absorber sustainably reduces the primary system response amplitude to as small as the minimum amplitude, within the variable range of 25 to 35 Hz. The same can be said for the time histories shown in Figure 13, where an increase of amplitude near the resonance is constantly suppressed by the tuned absorber. In Figure 12, the optimally tuned case approximately corresponds to the response curve

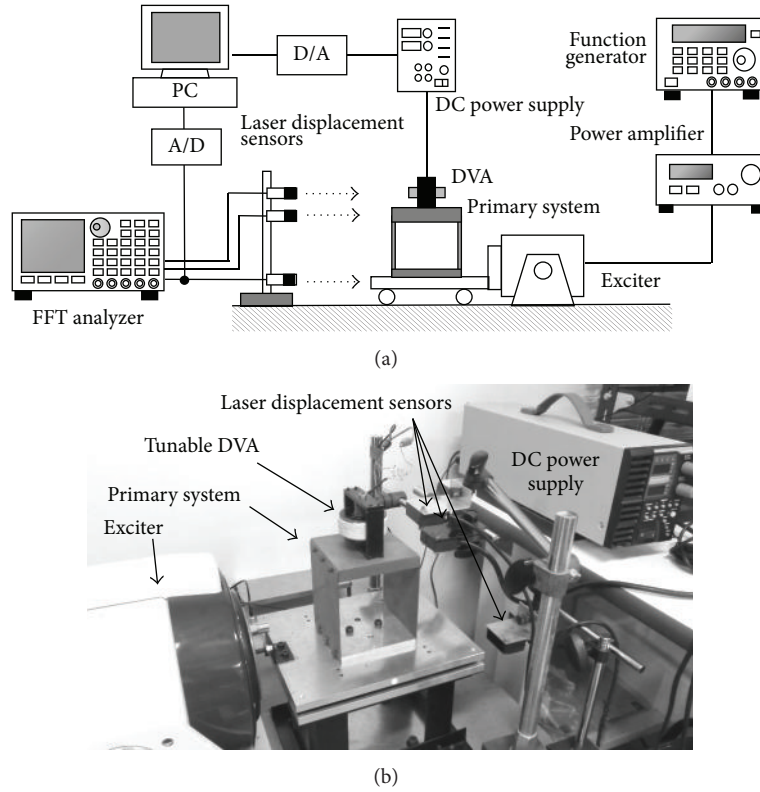


FIGURE 10: Experimental setup of base-excited primary system damped by stiffness-variable DVA: (a) schematic and (b) photograph.

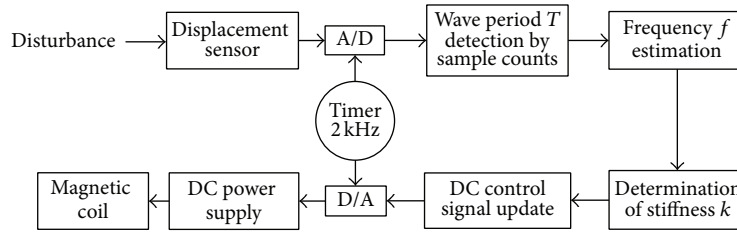


FIGURE 11: Block diagram of the controller for real-time frequency tuning of the absorber.

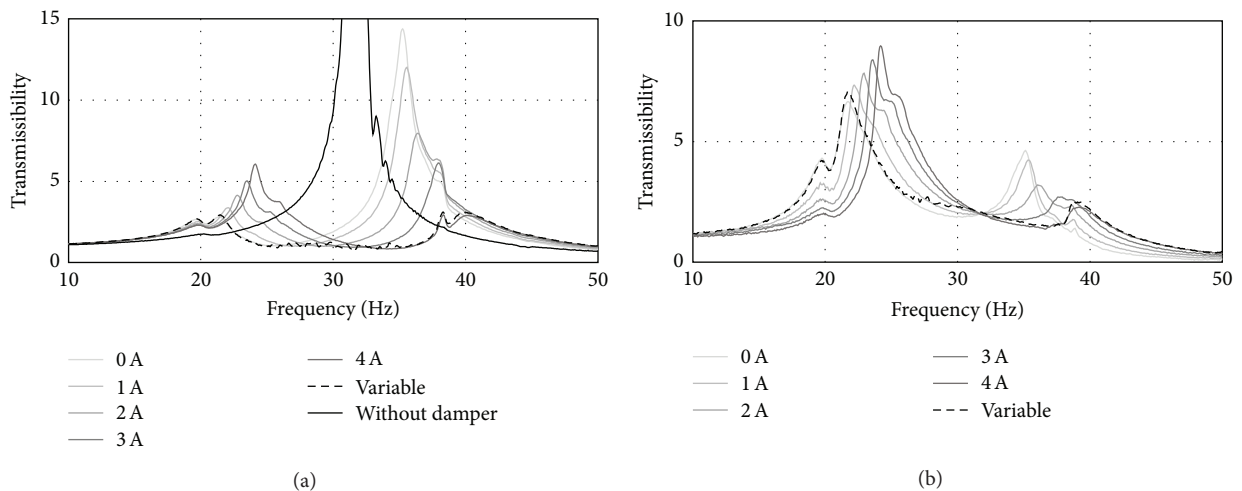


FIGURE 12: Response curves when the tunable DVA with MRE composed of 40% iron concentration is applied: (a) the primary system response and (b) the damper response.

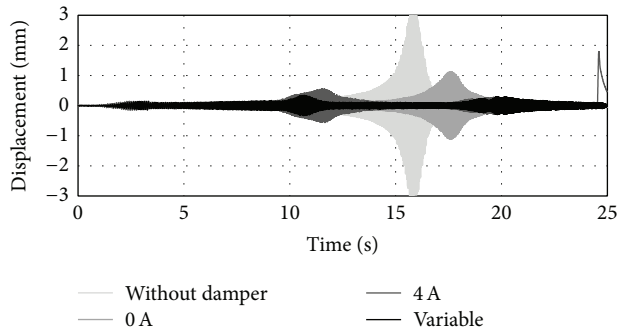


FIGURE 13: Time histories of the primary system response excited by swept-sine input at the speed of 2 Hz/sec.

obtained when an electric current of 4 A is applied. If we assume use of a damper with an optimal damping property, the amplitudes of the two distinct resonance peaks may decrease to the level of the two fixed points, while the amplitude within the frequency range between the points will increase, as predicted by the numerical investigation. On the other hand, outside the range, the amplitude will stay at the same level as the case where only the optimal tuning is considered. Consequently, the overall response of the adaptively tuned absorber is thought to outperform the response of the optimally tuned and damped absorber.

These results demonstrate that the frequency-tunable dynamic absorber using MRE works effectively for the vibration control of structures, while keeping the mechanism simple.

5. Conclusions

In this study, the dynamic property of the stiffness controllable elastomer, known as MRE, is experimentally evaluated. The dynamic property test shows that a certain optimal composition of materials within the mixture, in this case a 40 vol% iron content, leads to a maximum stiffness property change. On the other hand, the loss factor is found to be almost constant irrespective of the presence of the magnetic field. The MRE is then used in a DVA in order to provide natural frequency tunability. The absorber is further applied to the vibration control of a one-DOF structure in conjunction with a real-time stiffness switching algorithm, where the damping performance of the absorber is evaluated numerically and experimentally. To attain the effective design of the adaptive dynamic absorber and maximize the damping performance, the natural frequency of a target structure must be located at the middle of the variable frequency range of the absorber. Moreover, the swept-sine excitation results of a target structure demonstrate that better damping performance can be obtained by the real-time frequency-tunable dynamic absorbers than by passive-type absorbers. The proposed tunable dynamic absorber using MREs therefore enhances the damping performance with simple alteration of the stiffness element in the conventional passive-type absorber that works effectively for the vibration control of structures.

Conflict of Interests

The authors declare that there is no conflict of interests regarding the publication of this paper.

Acknowledgment

The work was financially supported by the Japan Ministry of Education, Culture, Sports, Science and Technology, Grant-in-Aid for Research (J-KAKEN), Category (C), no. 24560256.

References

- [1] J. P. den Hartog, *Mechanical Vibrations*, McGraw-Hill, 1956.
- [2] J. Q. Sun, M. R. Jolly, and M. A. Norris, "Passive, adaptive and active tuned vibration absorbers—a survey," *Journal of Vibration and Acoustics*, vol. 117, pp. 234–242, 1995.
- [3] K. Nagaya, A. Kurusu, S. Ikai, and Y. Shitani, "Vibration control of a structure by using a tunable absorber and an optimal vibration absorber under auto-tuning control," *Journal of Sound and Vibration*, vol. 228, no. 4, pp. 773–792, 1999.
- [4] P. L. Walsh and J. S. Lamancusa, "A variable stiffness vibration absorber for minimization of transient vibrations," *Journal of Sound and Vibration*, vol. 158, no. 2, pp. 195–211, 1992.
- [5] S. Nagarajaiah and E. Sonmez, "Structures with semiactive variable stiffness single/multiple tuned mass dampers," *Journal of Structural Engineering*, vol. 133, no. 1, pp. 67–77, 2007.
- [6] T. Komatsuzaki, Y. Iwata, and S. Morishita, "Semi-active vibration control of structures using MR elastomers," in *Proceedings of the 14th Asia-Pacific Vibration Conference (APVC '11)*, S. S. Law, L. Cheng, Y. Xia, and Z. Su, Eds., vol. 4, pp. 1875–1884, Hong Kong, China, 2011.
- [7] G. J. Liao, X.-L. Gong, S. H. Xuan, C. J. Kang, and L. H. Zong, "Development of a real-time tunable stiffness and damping vibration isolator based on magnetorheological elastomer," *Journal of Intelligent Material Systems and Structures*, vol. 23, no. 1, pp. 25–33, 2012.
- [8] H. X. Deng and X. L. Gong, "Adaptive tuned vibration absorber based on magnetorheological elastomer," *Journal of Intelligent Material Systems and Structures*, vol. 18, no. 12, pp. 1205–1210, 2007.
- [9] A. A. Lerner and K. A. Cunefare, "Performance of MRE-based vibration absorbers," *Journal of Intelligent Material Systems and Structures*, vol. 19, no. 5, pp. 551–563, 2008.
- [10] N. Hoang, N. Zhang, and H. Du, "An adaptive tunable vibration absorber using a new magnetorheological elastomer for vehicular powertrain transient vibration reduction," *Smart Materials and Structures*, vol. 20, no. 1, Article ID 015019, 2011.
- [11] A. V. Chertovich, G. V. Stepanov, E. Y. Kramarenko, and A. R. Khokhlov, "New composite elastomers with giant magnetic response," *Macromolecular Materials and Engineering*, vol. 295, no. 4, pp. 336–341, 2010.
- [12] X. L. Gong, X. Z. Zhang, and P. Q. Zhang, "Fabrication and characterization of isotropic magnetorheological elastomers," *Polymer Testing*, vol. 24, no. 5, pp. 669–676, 2005.
- [13] X. Zhang, S. Peng, W. Wen, and W. Li, "Analysis and fabrication of patterned magnetorheological elastomers," *Smart Materials and Structures*, vol. 17, no. 4, Article ID 045001, pp. 1–5, 2008.
- [14] M. R. Jolly, J. D. Carlson, B. C. Muñoz, and T. A. Bullions, "The magnetoviscoelastic response of elastomer composites

- consisting of ferrous particles embedded in a polymer matrix,” *Journal of Intelligent Material Systems and Structures*, vol. 7, no. 6, pp. 613–622, 1996.
- [15] L. C. Davis, “Model of magnetorheological elastomers,” *Journal of Applied Physics*, vol. 85, no. 6, pp. 3348–3351, 1999.
- [16] G. Y. Zhou, “Shear properties of a magnetorheological elastomer,” *Smart Materials and Structures*, vol. 12, no. 1, pp. 139–146, 2003.
- [17] S. J. Dyke, B. F. Spencer Jr., M. K. Sain, and J. D. Carlson, “Modeling and control of magnetorheological dampers for seismic response reduction,” *Smart Materials and Structures*, vol. 5, no. 5, pp. 565–575, 1996.
- [18] J. D. Carlson and M. R. Jolly, “MR fluid, foam and elastomer devices,” *Mechatronics*, vol. 10, no. 4, pp. 555–569, 2000.
- [19] N. Shimizu and H. Yamazaki, “Development of vibration insulator using a new material, silicone gel,” *Transactions of the Japan Society of Mechanical Engineers, Series C*, vol. 59, no. 568, pp. 3717–3724, 1993.

Research Article

Magnetic Circuit Analyses and Turning Chatter Suppression Based on a Squeeze-Mode Magnetorheological Damping Turning Tool

Yongliang Zhang,^{1,2} Norman M. Wereley,² Wei Hu,² Ming Hong,¹ and Wei Zhang¹

¹ Department of Mechanical Engineering, University of Shanghai for Science and Technology, Shanghai 200093, China

² Department of Aerospace Engineering, University of Maryland, College Park, MD 20742, USA

Correspondence should be addressed to Yongliang Zhang; yongliangz7377@163.com

Received 25 June 2014; Accepted 5 September 2014

Academic Editor: Weihua Li

Copyright © 2015 Yongliang Zhang et al. This is an open access article distributed under the Creative Commons Attribution License, which permits unrestricted use, distribution, and reproduction in any medium, provided the original work is properly cited.

As a smart material, magnetorheological fluid (MRF) has been utilized in fields including civil engineering and automotive engineering, and so on. In this study, the MR damping turning tool based on the squeeze-mode was developed to improve the vibration resistance of the tool system on the lathe. The 3D magnetic circuit simulations of the damper were performed. The influences of damper structural parameters, such as coil positions, plate thicknesses, and others, on the magnetic induction strength were investigated. Orthogonal experiments were carried out and the optimal combination of damper parameters was determined. The chatter suppressive experiments were carried out to evaluate the performance of the MR damping turning tool.

1. Introduction

Turning is a primary machining method in manufacturing industries. However, turning vibration is a significant factor limiting machining efficiency and preventing improvements in product quality. To reduce turning vibration, various dampers have been proposed in succession, including damping absorbers, dynamic vibration absorbers, friction dampers, and impact dampers [1]. In recent years, with the development of intelligent materials, the corresponding dampers have been developed by using unique properties of these kinds of material and researchers have paid more attention to this field.

As a semiactive control damper, magnetorheological (MR) dampers provide both adaptive and fail-safe passive force. In addition, they also possess advantages such as simplicity of structure, continuous adjustability of damping force, quick response, large output force, and low power consumption [2]. MR dampers have been utilized in fields including civil engineering, machine control, and automotive engineering [3–7]. It was reported that a magnetorheological semiactive suspension system installed on a heavy

Humvee increased cross-country speed by 30% to 40%. Jiang and Christenson proposed a large-scale MR damper for highway bridges, and the simulation and experimental results indicated that the peak and dynamic responses of a bridge were effectively reduced and the fatigue life of the structure was extended. Mei et al. developed an innovative magnetorheological (MR) fluid-controlled boring bar for chatter suppression.

The magnetic circuit design of a magnetorheological damper is critical to improve the working performance of the damper. A rational design of the circuit provides sufficient magnetic flux density for the damper in its operational environment, subsequently generating the required damping force [8–12]. Meanwhile, it is also necessary to avoid magnetic saturation. Nguyen and Choi generated braking force with a hybrid concept of magnetic circuit (using both axial and radial magnetic flux). Aiming at a flow-mode magnetorheological damper, by combining the power consumption of the coil and the piston volume as objective functions, Zheng et al. studied the optimal structural design of magnetorheological dampers which minimized the objective functions. Nguyen and Choi proposed a new approach to analyze the magnetic

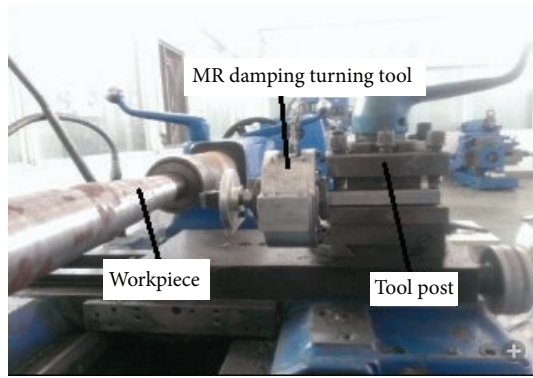


FIGURE 1: The photograph of MR damping turning tool.

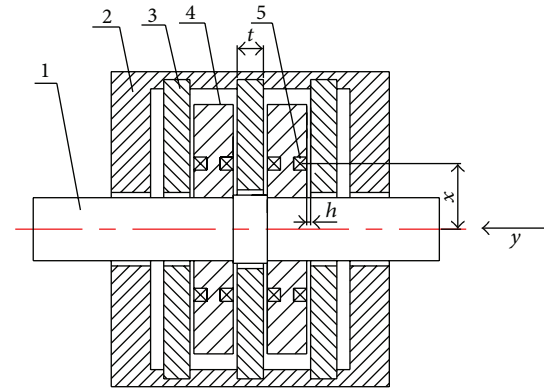


FIGURE 2: Structural diagram of MR damping turning tool.

circuit of an MR brake and used the approach to explore an engineering optimization problem.

Currently, much research on MR dampers has been carried out based on shearing and flow modes [13, 14]. The contribution of this work lies in two aspects. One is that a squeeze-mode magnetorheological damping turning tool was developed to effectively reduce vibrations in cylindrical turning since the yield strength of magnetorheological materials generated in squeeze mode is larger than that in shear mode, and the volume of a squeezed-mode MRF damper is smaller than that in other working modes. The other contribution is that the three-dimensional (3D) finite element simulations of the magnetic circuit of the damper were conducted, and the orthogonal experimental analyses were used to investigate the magnetic induction strength. With this method, the influence of different structural parameters on the magnetic flux density in the pole gap of the damper can be evaluated, which is helpful for the determination of the structural parameters MRF dampers. In this study, the key parameters influencing the damper were determined subsequently. Finally, cylindrical turning damping experiments were carried out using the MR damping turning tool with above key parameters to verify its effectiveness.

2. The Structure and Working Principle of the Magnetorheological Damping Turning Tool

In the cylindrical turning process of axis parts, major vibration exists in the normal direction of the turning surface of the parts, namely, the y -direction in Figure 2. In this study, a magnetorheological damper was installed on the rod of a turning tool to improve the vibration resistance of the tool system. The installation photograph of the magnetorheological damping turning tool is shown in Figure 1.

Since the yield stress of a magnetorheological fluid in squeeze mode is higher than that in the shear mode in a magnetic field, the squeeze mode was used as the working mode of this magnetorheological turning tool. The structure of the magnetorheological damper is depicted in Figure 2. In the damper, the rod axle (1) replaced the original rod of the cylindrical turning tool and was rigidly connected to the cylindrical turning tool head using a Morse taper,

the iron core (4) was interference fitted with the rod axle (1) and synchronously vibrated with the turning tool during the turning process, and the pole plate (3) was rigidly connected to the shell (2).

After applying current on the coil (5), magnetic field was generated in the damper. The direction of the magnetic flux lines between the two poles, namely, iron core (4) and pole plate (3), parallels the y -direction in Figure 2. Under action of the magnetic field, the magnetorheological fluid was polarised to chains along the y -direction. When vibration occurred during cylindrical turning, the iron core (4) and the turning tool underwent reciprocal motion along the y -direction relative to pole plate (3), and subsequently this motion squeezed the polarized chains of magnetorheological fluid. With the change of the applied current the squeeze yield strength of the magnetorheological fluid varied such that the damping and stiffness generated by MR damping turning tool could be controlled, thus restraining the vibration of the iron core (4) and the turning tool.

3. Simulation Analyses of the Magnetic Circuit under Different Parameters

The magnetic induction in the pole gap of the magnetorheological damper was influenced by varied parameters, such as coil position, rod axis material, pole plate thickness, and pole gap. In order to investigate the effect of these parameters on magnetic induction, the 3D simulations of magnetic induction were performed under different parameters using Ansoft Maxwell software.

3.1. Preprocessing. A 3D model of the damper was established using Solidworks software. Figure 3(a) shows the meshing results of the outside surface, and Figure 3(b) shows the meshing results of the axial section shown in Figure 2 after 3D meshing. In simulation, the type of current was defined as stranded, and the total current was inputted by $NI = 120 \times 2 \text{ A} = 240 \text{ A}$.

3.2. The Influence of Coil Position. The simulations of magnetic induction strength under different coil positions were

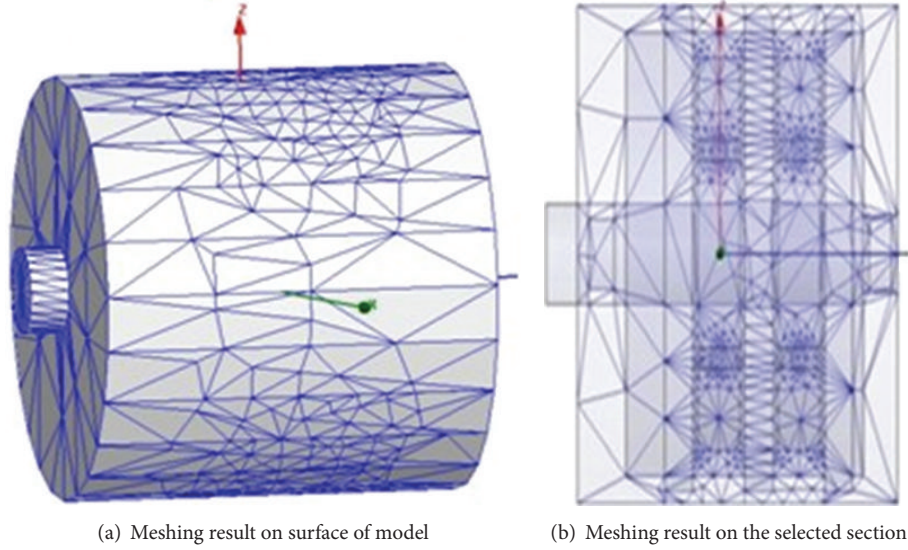
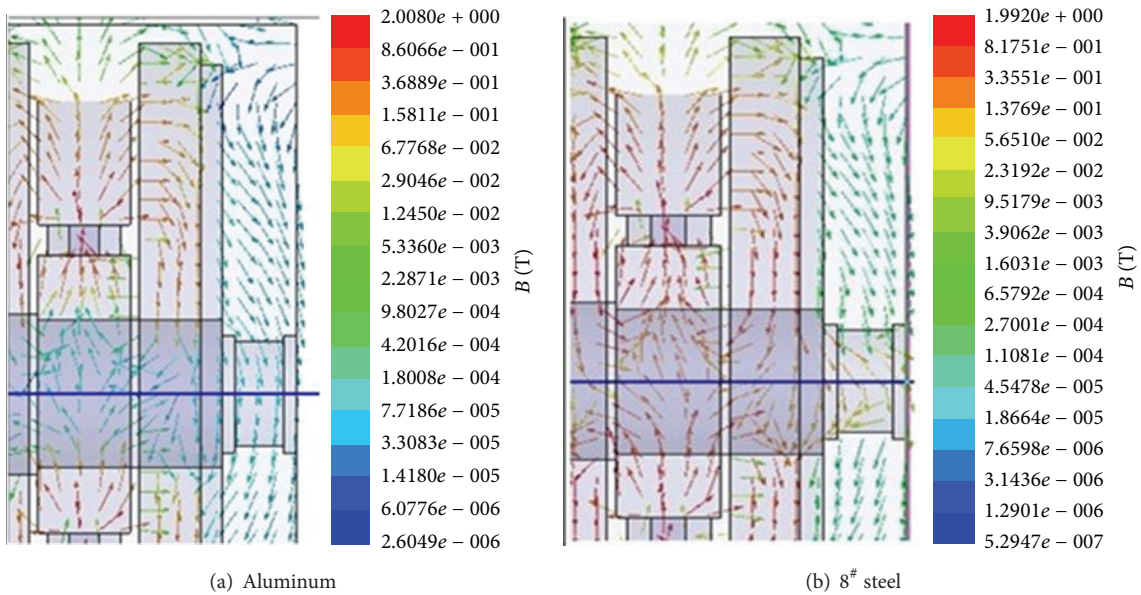


FIGURE 3: Chart of 3D meshing results.

FIGURE 4: Cloud charts of magnetic lines of force for arbor shaft in aluminum and 8[#] steel.

carried out, and their maximum values of magnetic induction strength between the gaps are listed in Table 1. The x indicates the radial distance from the axis of rod axle to the coil, shown in Figure 2. The results display that the magnetic induction strength increases as the distance between the coil and the axis increases.

3.3. The Influence of Rod Axle Material. The permeability of material has strong effect on the magnetic induction strength. The magnetic induction strengths with different material of rod axle are simulated and their maximum values at gap are listed in Table 2, in which the permeability of varied materials

TABLE 1: Simulated results of magnetic induction strength at coil's different positions.

Number	Position of coil x/mm	Magnetic induction strength B_{\max}/T
1	20	0.258
2	22.5	0.369
3	25	0.476

tends to increase in order of aluminium, 45[#], and 8[#]. The results show that the lower the permeability of rod axle's material, the higher the magnetic induction strength.

TABLE 2: Simulated results of magnetic induction strength for different material of rod axle.

Number	Material of rod axle	Magnetic induction strength	
		B_{\max}/T	
1	Aluminium	0.369	
2	45 [#]	0.354	
3	8 [#]	0.336	

TABLE 3: Simulated results of magnetic induction strength for different plate thickness.

Number	Plate thickness t/mm	Magnetic induction strength	
		B_{\max}/T	
1	8	0.252	
2	10	0.369	
3	12	0.269	

TABLE 4: Simulated results of magnetic induction strength for different width of gap.

Number	Width of gap h/mm	Magnetic induction strength	
		B_{\max}/T	
1	1.5	0.369	
2	1.8	0.278	
3	2.0	0.246	

The cloud charts of magnetic lines of force with aluminium and 8[#] are, respectively, given in Figures 4(a) and 4(b). In Figure 4(a), the strength of magnetic lines of force is weak through the rod axle and only reaches the 10^{-4} orders of magnitude. On the other hand, when the material of the rod axle is 8[#], the strength of magnetic lines of force through the rod axle increases about 100 times.

3.4. The Influence of Plate Thickness. The simulations of magnetic induction strength with different value of plate thickness were performed, and their maximum values are listed in Table 3. The plate thickness t is given in Figure 2. In Table 3, the relationship between plate thickness and magnetic induction strength is not monotonic. For the damper in this paper, the magnetic induction strength is maximized when the plate thickness is 10 mm, and the magnetic induction strength decreases when the plate thickness either increases or decreases.

3.5. The Influence of the Width of Pole Gap. The magnetic induction strengths with different width of gap were simulated, and the results are listed in Table 4, in which the thickness of plate is 10 mm. The results demonstrate that the narrower the gap is, the larger the magnetic induction strength is. The width of gap h is displayed in Figure 2.

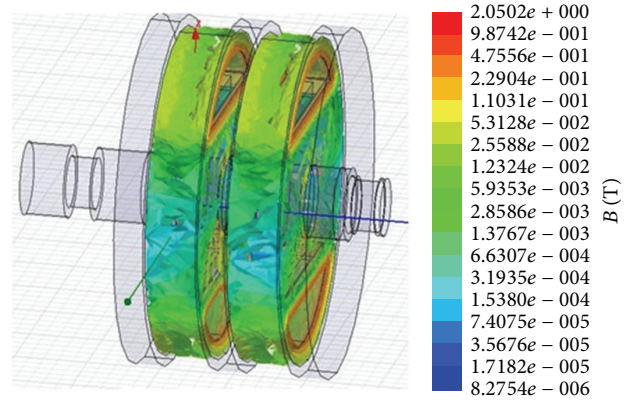


FIGURE 5: 3D simulated result of magnetic induction strength.

4. Magnetic Circuit Analyses Using Multifactor Orthogonal Experiment

To determine the optimal structural size of the damper, an orthogonal experiment was carried out using orthogonal table of four factors and three levels $L_9(3^4)$. With this experiment, the structural parameter of damper with the strongest or weakest effect on the magnetic induction B can be analysed, and the optimal combination of different parameters can be achieved. Table 5 shows the factors and levels in the experiment, and Table 6 lists the experimental scheme and the simulating results under corresponding factors and levels.

In Table 6, the variances are used to evaluate the impact of each factor on magnetic induction strength. Generally, the larger variance demonstrates that the corresponding factor has a stronger influence on the experimental results. The data in Table 6 indicate that the material of rod axle is the main factor influencing the magnetic induction strength, and the factors influencing the magnetic induction in the descending order were the material of rod axle, pole gap, coil position, and pole plate thickness. The optimal combination to acquire the appropriate magnetic induction was as follows: the rod axle's material is aluminium and the distance from coil to the axial symmetry centre of the damper was $x = 25$ mm at pole plate thickness of 10 mm and pole gap of 1.5 mm.

Figures 5 and 6 show the 3D simulated distribution of the magnetic induction of the damper and the distribution of the magnetic induction on the section displayed in Figure 2 according to the optimal structural parameters stated above, respectively. It can be observed that the maximum magnetic induction in the pole gap reached 0.54 T, which complied with design requirements.

5. Damping Experiments Based on the Magnetorheological Damping Turning Tool

To verify the chatter suppressive effect of the magnetorheological damping turning tool, it was manufactured and installed on a CA6140 lathe carriage, and the chatter suppressive experiments were carried out. The experimental

TABLE 5: The factors and levels.

Level	Factor			
	Coil position x/mm	Plate thickness t/mm	Pole gap h/mm	Rod axle material
1	20	8	1.5	Aluminum
2	22.5	10	1.8	45 [#]
3	25	12	2.0	8 [#]

TABLE 6: The experimental scheme and results.

Factor	x	t	h	Material	Magnetic induction B/T
Test number	Level number				
1	1	1	1	1	0.35728
2	1	2	2	2	0.31623
3	1	3	3	3	0.29431
4	2	1	2	3	0.28730
5	2	2	3	1	0.34744
6	2	3	1	2	0.32650
7	3	1	3	2	0.33056
8	3	2	1	3	0.35822
9	3	3	2	1	0.34830
k_1	0.32261	0.32505	0.34733	0.35101	
k_2	0.32041	0.34063	0.31728	0.32443	
k_3	0.34569	0.32304	0.32410	0.31477	
Variance	0.02528	0.01759	0.03005	0.03624	
Descending order	Material, h , x , t				
Optimal scheme	material ₁ $h_1x_3t_2$				

Note: $k_i = \text{sum}(B_i)/s$, where B_i is magnetic induction when the level number is i and s is the number of level i in that column, $i = 1, 2, 3$.

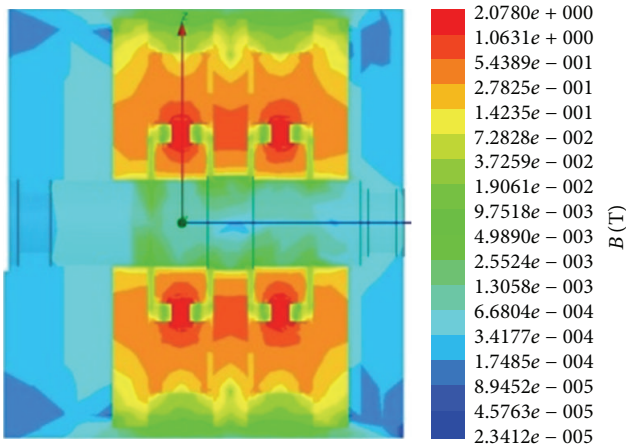


FIGURE 6: Results of magnetic induction strength on the selected section.

system block diagram is shown in Figure 7. The MRF-132DG developed by the American LORD company was used in the experiments, and the workpiece was 45[#] steel bar stock (600 mm in length and 60 mm in diameter). The turning parameters were spindle speed $n = 320$ rpm, feed rate $f = 0.08$ mm/r, and depth of turning $a_p = 0.4$ mm.

Figures 8(a) and 8(b) show the time-domain signals of the acceleration of the magnetorheological damping turning

tool in the y -direction without current and with 2 A applied current on each coil, respectively. Figure 8(a) shows that the vibration amplitude of the acceleration signal increased at time $t = 4$ s and the amplitude increased with the continuation of the process. Figure 8(b) shows the results of imposing 2 A on the damper at $t = 6$ s. The amplitude of the acceleration signal decreased at $t = 20$ s after imposing current and a substantially reduced amplitude was maintained thereafter.

In the frequency domain, Figure 9(a) indicates that the main vibration frequency of the vibration signal before imposing current was approximately 255 Hz and the peak of power spectrum density was approximately 1.1×10^7 V. Figure 9(b) shows the dominant frequency of the vibration signal after imposing current, increased to approximately 466 Hz. This indicated that the stiffness of the system was enhanced and the peak of the dominant mode of the system had been reduced to 7.1×10^4 V, which was 7% of the peak value when the current was not applied.

These time- and frequency-domain analyses showed that the developed magnetorheological damping turning tool exhibited a significant restraining effect on turning vibration.

6. Conclusions

To reduce the vibration in cylindrical turning, a magnetorheological damping turning tool based on the squeeze mode was designed and manufactured. On the basis of

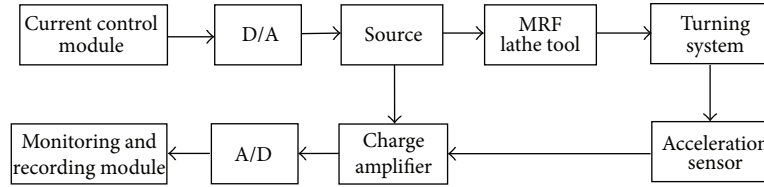


FIGURE 7: The system block diagram of turning damping experiment.

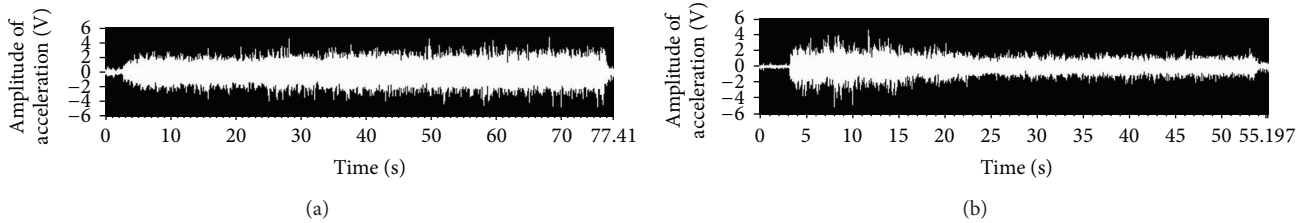


FIGURE 8: The time-domain signals of acceleration without current and 2 A current on each coil.

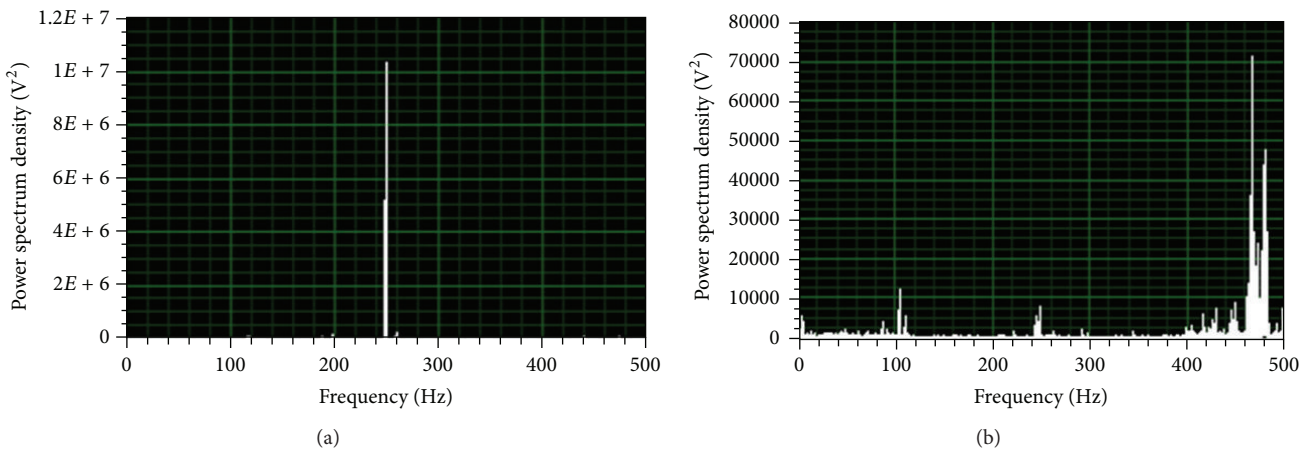


FIGURE 9: The power spectrum density of corresponding acceleration signals before and after imposing current.

its structural design, 3D finite element simulations of the magnetic induction of the damper were carried out with different parameters according to the basic principles of electromagnetism. It shows that the magnetic field strength in the gap increases as the distance between the axis of the rod axle and coil increases, the permeability of the rod axle decreases and the gap thickness decreases. As to the magnetic pole thickness, the relationship between it and magnetic induction strength is not monotonous.

Furthermore, these simulation data were utilized in the orthogonal experiment. The results indicated that the factors influencing the magnetic induction of this magnetorheological damping turning tool, in decreasing order, were pole gap, coil position, and plate thickness. Therefore, the optimal structural parameters of the damping turning tool were determined.

Afterwards, chatter suppression experiments were undertaken during cylindrical turning using the prototyped magnetorheological damping turning tool. The experimental data from both time- and frequency-domains verified that

the magnetorheological damping turning tool, based on the squeeze mode, can significantly reduce turning vibration.

Conflict of Interests

The authors declare that there are no conflicts of interests regarding the publication of this paper.

Acknowledgment

The project “Magnetorheological fluid mechanics modeling and its coupled damping mechanism of turning system with variable parameters” was supported by the National Natural Science Foundation of China (no. 51205255).

References

- [1] M. Siddhpura and R. Paurobally, “A review of chatter vibration research in turning,” *International Journal of Machine Tools and Manufacture*, vol. 61, pp. 27–47, 2012.

- [2] G. Park, M. T. Bement, D. A. Hartman, R. E. Smith, and C. R. Farrar, "The use of active materials for machining processes: a review," *International Journal of Machine Tools & Manufacture*, vol. 47, no. 15, pp. 2189–2206, 2007.
- [3] S. H. Ha, M.-S. Seong, and S.-B. Choi, "Design and vibration control of military vehicle suspension system using magnetorheological damper and disc spring," *Smart Materials and Structures*, vol. 22, no. 6, Article ID 065006, 2013.
- [4] A. Farjoud, R. Taylor, E. Schumann, and T. Schlangen, "Advanced semi-active engine and transmission mounts: tools for modelling, analysis, design, and tuning," *Vehicle System Dynamics*, vol. 52, no. 2, pp. 218–243, 2014.
- [5] Z. Jiang and R. Christenson, "Experimental verification of an MR damper controlled highway bridge," in *Proceedings of the 19th Analysis and Computation Specialty Conference*, pp. 347–358, Orlando, Fla, USA, May 2010.
- [6] D. Sathianarayanan, L. Karunamoorthy, J. Srinivasan, G. S. Kandasami, and K. Palanikumar, "Chatter suppression in boring operation using magnetorheological fluid damper," *Materials and Manufacturing Processes*, vol. 23, no. 4, pp. 329–335, 2008.
- [7] D. Mei, Z. Yao, T. Kong, and Z. Chen, "Parameter optimization of time-varying stiffness method for chatter suppression based on magnetorheological fluid-controlled boring bar," *International Journal of Advanced Manufacturing Technology*, vol. 46, no. 9–12, pp. 1071–1083, 2010.
- [8] Q. H. Nguyen and S. B. Choi, "Optimal design of a novel hybrid MR brake for motorcycles considering axial and radial magnetic flux," *Smart Materials and Structures*, vol. 21, no. 5, Article ID 055003, 2012.
- [9] Z. Ling, L. Xiaohui, and L. Yinong, "Optimization of magnetorheological damper based on a combination of objective function," *Journal of Vibration Engineering (Chinese Journal)*, vol. 24, no. 6, pp. 600–605, 2011.
- [10] Z. Parlak, T. Engin, and I. Çalli, "Optimal design of MR damper via finite element analyses of fluid dynamic and magnetic field," *Mechatronics*, vol. 22, no. 6, pp. 890–903, 2012.
- [11] B. Yang, J. Luo, and L. Dong, "Magnetic circuit FEM analysis and optimum design for MR damper," *International Journal of Applied Electromagnetics and Mechanics*, vol. 33, no. 1-2, pp. 207–216, 2010.
- [12] P. B. Nguyen and S. B. Choi, "A new approach to magnetic circuit analysis and its application to the optimal design of a bi-directional magnetorheological brake," *Smart Materials and Structures*, vol. 20, no. 12, Article ID 125003, 2011.
- [13] T. Pranoto, K. Nagaya, Y. Ebara, and Q. Q. Long, "Vibration suppression device using permanent-electromagnet and MRF shear damper," *Journal of Materials Processing Technology*, vol. 181, no. 1–3, pp. 235–240, 2007.
- [14] W. Hu, G. J. Hiemenz, G. Ngatu, and N. M. Wereley, "Performance evaluation of shear mode and flow mode magnetorheological (MR) energy absorbers for adaptive seat suspension systems," in *Proceedings of the 53rd AIAA/ASME/ASCE/AHS/ASC Structures, Structural Dynamics and Materials Conference*, Collection of Technical Papers, 2012.

Research Article

Wavelet Adaptive Algorithm and Its Application to MRE Noise Control System

Zhang Yulin and Zhao Xiuyang

School of Information Science and Engineering, University of Jinan, Jinan 250022, China

Correspondence should be addressed to Zhao Xiuyang; zhaoxy@ujn.edu.cn

Received 24 January 2015; Accepted 21 March 2015

Academic Editor: Seung-Bok Choi

Copyright © 2015 Z. Yulin and Z. Xiuyang. This is an open access article distributed under the Creative Commons Attribution License, which permits unrestricted use, distribution, and reproduction in any medium, provided the original work is properly cited.

To address the limitation of conventional adaptive algorithm used for active noise control (ANC) system, this paper proposed and studied two adaptive algorithms based on Wavelet. The twos are applied to a noise control system including magnetorheological elastomers (MRE), which is a smart viscoelastic material characterized by a complex modulus dependent on vibration frequency and controllable by external magnetic fields. Simulation results reveal that the Decomposition LMS algorithm (D-LMS) and Decomposition and Reconstruction LMS algorithm (DR-LMS) based on Wavelet can significantly improve the noise reduction performance of MRE control system compared with traditional LMS algorithm.

1. Introduction

The most popular algorithm used to adapt FIR filters is the Widrow-Hoff LMS [1], which is shown in Figure 1. Its popularity is due to its low computational complexity and robustness to implementation errors.

As in Figure 1, $x(n)$, $d(n)$, $e(n)$, and $y(n)$ denote the reference of system, disturbance, control error, and control signal, respectively. The system control signal can be expressed as

$$y(n) = X^T(n)W(n), \quad (1)$$

where $W(n) = [w_0, w_1, \dots, w_{N-1}]^T$ is the weight vector of the N order control filter, $X^T(n) = x(n) \sum_{i=0}^{N-1} z^{-i}$, and T denotes the vectors transpose. The goal is to minimize the output error:

$$e(n) = d(n) - y(n). \quad (2)$$

According to the Widrow-Hoff LMS algorithm [1], the weight of control filter can be adjusted by

$$W(n+1) = W(n) + 2\mu X(n)e(n), \quad (3)$$

where μ is the step-size parameter. The convergence rate of this algorithm depends on the condition numbers of

the autocorrelation R_x of the reference signal. When the eigenvalues of R_x are widely spread, the excess mean square error produced by LMS algorithm is primarily determined by the largest eigenvalue, and the time taken by the average tap-weight vector $E[\widehat{W}(k)]$ to converge is limited by the smallest eigenvalue. However, the speed of convergence of the mean square error is affected by the spread of the eigenvalues of R_x .

The speed of convergence of the LMS algorithm may slow down when the correlation matrix of the inputs is ill-conditioned, which implies that the control system with Widrow-Hoff LMS adaptive algorithm might become unstable when inputs change indefinitely. In order to enhance the performance of the algorithm, Wavelet Transform is proposed in this study due to its time-frequency localization [2, 3]. This paper presents two kinds of adaptive wavelet algorithm: Decomposition LMS algorithm (D-LMS) and Decomposition and Reconstruction LMS algorithm (DR-LMS).

2. Decomposition LMS Algorithm (D-LMS)

In D-LMS algorithm, the input signal is decomposed into various wavelet spaces according to various scales to form the input vector, and then the adaptive filter weight

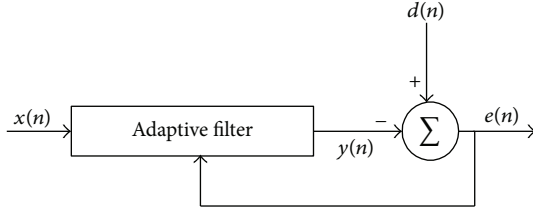


FIGURE 1

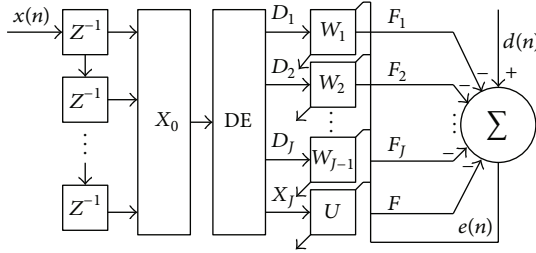


FIGURE 2: Decomposition LMS algorithm.

corresponding to a certain frequency component is adjusted. This means that the proportion of each frequency of input signal is altered so as to reconstruct the output signal to approximate the desired signal [4–6].

2.1. Structure of D-LMS. Schematic of the D-LMS is provided in Figure 2. Here, $x(n)$ is the input signal, $X_0 = x(n) \sum_{i=0}^{N-1} z^{-i}$ represents the input vector of the D-LMS algorithm, and DE denotes the signal decomposition with MALLAT algorithm [7]. $D_j = [d_{j,0}, d_{j,1}, \dots, d_{j,2^{-j}N-1}]^T$ ($j = 1, \dots, J$) is the j th level detail signal of original signal, $X_J = [x_0, x_1, \dots, x_{2^{-j}N-1}]^T$ is the J th level approximation signal of original signal, $W_j = [w_{j,0}, w_{j,1}, \dots, w_{j,2^{-j}N-1}]^T$ ($j = 1, \dots, J$) is the weight vector of j th level details signal, and $U = [u_0, u_1, \dots, u_{2^{-j}N-1}]^T$ is weight vector of the J th level approximation signal.

2.2. Adaptation of Weight Vectors. As seen in Figure 2,

$$F_j = D_j^T W_j \quad (j = 1, \dots, J), \quad (4)$$

$$F = X_J^T U, \quad (5)$$

$$e(n) = d_n - \sum_{j=1}^J F_j - F. \quad (6)$$

Equation (6) also can be written as follows:

$$e(n) = d_n - \sum_{j=1}^J D_j^T W_j - X_J U. \quad (7)$$

According to the LMS algorithm, the equations of W and U are as follows:

$$W_j = W_j + \mu_j (-\hat{\nabla}_j) \quad (j = 1, \dots, J), \quad (8)$$

$$U = U + \mu (-\hat{\nabla}_J), \quad (9)$$

where μ_j ($j = 1, \dots, J$) and μ represent the step-size of the j th level detail signal and J th level approximation signal, respectively. $\hat{\nabla}_j$ and $\hat{\nabla}_J$, which denote the instantaneous estimation gradient vectors with $e^2(n)$ to W_j and U separately, can be expressed as follows:

$$\hat{\nabla}_j = 2e(n) \frac{\partial e(n)}{\partial W_j} \quad (j = 1, \dots, J) \quad (10)$$

$$\hat{\nabla}_J = 2e(n) \frac{\partial e(n)}{\partial U}.$$

In this study, we can place the emphasis only on the adjustment of W_j as U resembles W_j in the adjustment way.

First, rewrite (10) as follows:

$$\hat{\nabla}_j = 2e(n) \left[\frac{\partial e(n)}{\partial w_{j,0}}, \frac{\partial e(n)}{\partial w_{j,1}}, \dots, \frac{\partial e(n)}{\partial w_{j,2^{-j}N-1}} \right]^T, \quad (11a)$$

$$\hat{\nabla}_J = 2e(n) \left[\frac{\partial e(n)}{\partial u_0}, \frac{\partial e(n)}{\partial u_1}, \dots, \frac{\partial e(n)}{\partial u_{2^{-j}N-1}} \right]^T. \quad (11b)$$

According to (4) and (5), the following equation is obtained:

$$\frac{\partial e(n)}{\partial w_{i,k}} = -\sum_{j=0}^J D_j^T \frac{\partial W_j}{\partial w_{i,k}} - X_J^T \frac{\partial U}{\partial w_{i,k}} = -d_{i,k}. \quad (12)$$

Then, the adaptation of W can be given by

$$w_{j,k} = w_{j,k} + 2\mu_j e(n) d_{j,k}. \quad (13)$$

Here, $i = 1, \dots, J$, $k = 0, \dots, 2^{-i}N - 1$. Similarly, the adaptation of U can be expressed by

$$u_k = u_k + 2\mu e(n) x_k. \quad (14)$$

Here, $0 \leq k < 2^{-j}N$.

3. Decomposition and Reconstruction LMS Algorithm (DR-LMS)

3.1. The Structure of DR-LMS. Schematic of the DR-LMS algorithm is shown in Figure 3, in which the signal is not only decomposed, but also reconstructed.

Where X_0 , DE , D_j ($j = 1, \dots, J$), X_J , W_j , and U are the same meanings as in Figure 2. V_j ($j = 1, \dots, J-1$) and Y_J are the vectors, which can be expressed, respectively, by

$$V_j = D_j \hat{\times} W_j \quad j = 1, \dots, J, \quad (15)$$

$$Y_J = X_J \hat{\times} U.$$

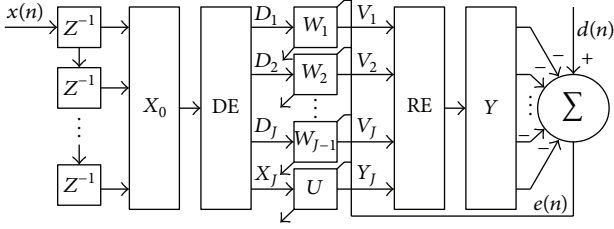


FIGURE 3: DR-LMS algorithm.

Here, $\hat{\times}$ denotes that each component of vector is multiplied by corresponding component of another vector. *RE* signifies the signal reconstruction. $Y = [y_0, y_1, \dots, y_{N-1}]^T$ represents the results of reconstruction.

It is obvious that the DR-LMS algorithm consists of three parts: firstly, the signal is decomposed into various levels, then each level detail signal and final approximation signal are multiplied by the corresponding weight vectors, and, finally, these signals are reconstructed by MALLAT algorithm to form the output of DR-LMS algorithm. In the process, the weight vectors are adapted to minimize the $e(n)$; therefore, the law of the adaptation is crucial.

3.2. Adaptation of Weight Vector. As indicated in Figure 3, the error $e(n)$ is represented by

$$e(n) = d(n) - Y^T T, \quad (16)$$

where $T = [1, 1, \dots, 1]_{1 \times N}^T$. According to LMS algorithm, in order to minimize the error $e(n)$, W_j and U can be adapted by (8) and (9). With the foregoing discussion, we only study the adaptation way of W_j and then can obtain the adaptation way of U in the same way.

According to MALLAT algorithm and Figure 3, the following equations are obtained:

$$\begin{aligned} Y(m) &= 2 \sum_k h(m-2k) Y_1(k) \\ &\quad + 2 \sum_k g(m-2k) V_1(k), \\ Y_1(m) &= 2 \sum_k h(m-2k) Y_2(k) \\ &\quad + 2 \sum_k g(m-2k) V_2(k), \\ Y_2(m) &= 2 \sum_k h(m-2k) Y_3(k) \\ &\quad + 2 \sum_k g(m-2k) V_3(k). \end{aligned} \quad (17)$$

Substitute (15) into (17):

$$\begin{aligned} Y(m) &= 2 \sum_k h(m-2k) Y_1(k) \\ &\quad + 2 \sum_k g(m-2k) (D_1 \hat{\times} W_1)(k), \end{aligned} \quad (18)$$

$$\begin{aligned} Y_1(m) &= 2 \sum_k h(m-2k) Y_2(k) \\ &\quad + 2 \sum_k g(m-2k) (D_2 \hat{\times} W_2)(k), \end{aligned} \quad (19)$$

$$\begin{aligned} Y_2(m) &= \sum_k h(m-2k) Y_3(k) \\ &\quad + \sum_k g(m-2k) (D_3 \hat{\times} W_3)(k). \end{aligned} \quad (20)$$

3.2.1. $\partial e(n)/\partial w_{j,k}$ and $\partial e(n)/\partial u_i$. According to (11a) and (11b) and (12), $\partial e(n)/\partial w_{j,k}$ should be first given so as to calculate \hat{V}_j . To address this problem, this study employs induction. Here, $\partial e(n)/\partial w_{1,i}$, $\partial e(n)/\partial w_{2,i}$, and $\partial e(n)/\partial w_{3,i}$ are given as follows.

(1) $\partial e(n)/\partial w_{1,i}$. By (16), $\partial e(n)/\partial w_{1,i}$ can be expressed as

$$\frac{\partial e(n)}{\partial w_{1,i}} = \sum_{m=0}^{N-1} \frac{\partial Y(m)}{\partial w_{1,i}}. \quad (21)$$

Substitute (18) into above equation:

$$\begin{aligned} \frac{\partial e(n)}{\partial w_{1,i}} &= 2 \sum_{m=0}^{N-1} \sum_{k_0} h(m-2k_0) \frac{\partial Y_1(k_0)}{\partial w_{1,i}} \\ &\quad + 2 \sum_{m=0}^{N-1} \sum_{k_0} g(m-2k_0) \frac{\partial (D_1 \hat{\times} W_1)(k_0)}{\partial w_{1,i}}. \end{aligned} \quad (22)$$

It is clear that Y_1 is not correlative with W_1 , so (22) can be rewritten as

$$\frac{\partial e(n)}{\partial w_{1,i}} = 2 \sum_{m=0}^{N-1} g(m-2i) D_1(i). \quad (23)$$

(2) $\partial e(n)/\partial w_{1,i}$. In the same way, $\partial e(n)/\partial w_{1,i}$ can be expressed by

$$\frac{\partial e(n)}{\partial w_{2,i}} = \sum_{m=0}^{N-1} \frac{\partial Y(m)}{\partial w_{2,i}}. \quad (24)$$

Substitute (18) into (23), and

$$\frac{\partial (D_1 \hat{\times} W_1)(k_0)}{\partial w_{2,i}} = 0. \quad (25)$$

Then (24) can be rewritten as

$$\frac{\partial e(n)}{\partial w_{2,i}} = 2 \sum_{m=0}^{N-1} \sum_{k_0} h(m-2k_0) \frac{\partial Y_1(k_0)}{\partial w_{2,i}}. \quad (26)$$

Substitute (19) into (26), and

$$\frac{\partial Y_2(k_1)}{\partial w_{2,i}} = 0. \quad (27)$$

So, the final expression of $\partial e(n)/\partial w_{1,i}$ is

$$\frac{\partial e(n)}{\partial w_{1,i}} = 2^2 \sum_{m=0}^{N-1} \sum_{k_0} h(m-2k_0) g(k_0-2i) D_1(i). \quad (28)$$

(3) $\partial e(n)/\partial w_{3,i}$. Similarly, $\partial e(n)/\partial w_{3,i}$ can also be obtained; it is represented by

$$\begin{aligned} & \frac{\partial e(n)}{\partial w_{3,i}} \\ &= 2^3 \sum_{m=0}^{N-1} \sum_{k_0} h(m-2k_0) \sum_{k_1} h(k_0-2k_1) g(k_1-2i) D_2(i). \end{aligned} \quad (29)$$

From the above, $\partial e(n)/\partial w_{1,i}$, $\partial e(n)/\partial w_{1,i}$, and $\partial e(n)/\partial w_{3,i}$ have been obtained. By comparing them with each other, the universal expression of $\partial e(n)/\partial w_{j,i}$ can be induced:

$$\begin{aligned} \text{If } j=1 & \quad \frac{\partial e(n)}{\partial w_{1,i}} = \sum_{m=0}^{N-1} g(m-2i) D_1(i), \\ \text{If } j \neq 1 & \quad \frac{\partial e(n)}{w_{ji}} = \sum_{m=0}^{N-1} Z_j(m,i) D_j(i), \end{aligned} \quad (30)$$

where $j=1, \dots, J$ and $i=0, \dots, 2^{-j}N-1$. Consider

$$\begin{aligned} & Z_j(m,i) \\ &= 2^j \sum_{k_0} \sum_{k_1} \dots \sum_{k_{j-1}} h(m-2k_0) \dots h(k_{j-3}-2k_{j-2}) g(k_{j-2}-2i). \end{aligned} \quad (31)$$

As U is the same as W_j in the adaptation way, we can easily obtain the expression of $\partial e(n)/\partial u_i$:

$$\frac{\partial e(n)}{\partial u_i} = 2^j \sum_{m=0}^{N-1} V_j(m,i) X_j(i), \quad (32)$$

where $i=0, \dots, 2^{-j}N-1$. Consider

$$\begin{aligned} & V_j(m,i) \\ &= 2^j \sum_{k_0} \sum_{k_1} \dots \sum_{k_{j-1}} h(m-2k_0) \dots h(k_{j-3}-2k_{j-2}) h(k_{j-2}-2i). \end{aligned} \quad (33)$$

3.2.2. Adaptation of W_j and U

(1) W_j

$$\text{If } j=1 \quad w_{1i} = w_{1i} + 2^2 \mu_1 e(n) \sum_{m=0}^{N-1} g(m-2i) D_1(i) \quad (34)$$

$$\text{If } j \neq 1 \quad w_{ji} = w_{ji} + 2^{j+1} \mu_j e(n) \sum_{m=0}^{N-1} Z_j(m,i) D_j(i),$$

where $1 \leq j \leq J$, $0 \leq i < 2^{-j}N$.

$Z_j(m,i)$ is the same meaning as expression above, and μ_j is the step-size of j th level detail signal.

(2) U

$$u_i = u_i + 2^{J+1} \mu_J e(n) \sum_{m=0}^{N-1} V_J(m,i) X_J(i), \quad (35)$$

where $V_J(m,i)$ is also the same meaning as the expression above and μ_J is the step-size of final approximation signal.

4. MRE Noise Control System

4.1. *Dynamics of MRE.* Magneto-rheological elastomers (MREs) are promising smart materials, which consist of magnetically polarizable particles in nonmagnetic solid or gel-like medium [8, 9]. As a compound of smart magneto-rheological (MR) fluid and viscoelastic materials, the MRE combines the salient features of both materials, including controllable stiffness and frequency-dependent viscoelastic behavior, which can be reversibly controlled under external magnetic fields in milliseconds.

The MRE is generally regarded as a viscoelastic material [10], so its dynamic behavior can be described with a complex modulus which depends on vibration frequency and be controllable by external magnetic fields. In order to analyze the mechanical properties of MRE in the magnetic field, the modal of MRE can be simplified to a general kelvin model of viscoelastic material in parallel with an adjustable spring which was controlled by the applied magnetic field, as shown in Figure 4. In the noise control system, as the strain caused by the noise is small, the modal of MRE can be treated as a linear modal, in which the magnetic-induced modulus is adjusted by the applied magnetic field.

As shown in Figure 4, when the MRE is subjected to the applied alternate strain where

$$\gamma(t) = \gamma_0 e^{i\omega t} = \gamma_0 (\cos \omega t + i \sin \omega t), \quad (36)$$

the corresponding stress will become

$$\tau(t) = G_0 \gamma + G_m \dot{\gamma} + \eta \ddot{\gamma} = \tau_0 e^{i(\omega t + \delta)}. \quad (37)$$

According to the definition of complex modulus and (1) and (2), the complex modulus of MRE can be expressed as below:

$$G(i\omega) = \frac{\tau(t)}{\gamma(t)} = G^I(i\omega) + iG^R(i\omega), \quad (38)$$

where γ and τ denote the shear strain and stress of the MRE, γ_0 and τ_0 represent amplitudes of strain and stress, respectively, and G_0 , G_m , and η express the initial modulus, variable modulus, and viscosity coefficient, respectively. ω is the vibration frequency; δ is the delayed phase between stress and strain.

The real part of the complex modulus $G^R(i\omega)$ is storage modulus which is representing the viscoelastic stiffness of the MRE. The imaginary part $G^I(i\omega)$ is loss modulus, and

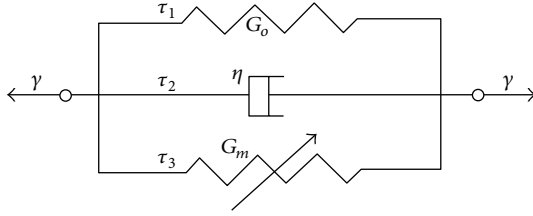


FIGURE 4: The viscoelastic model of MRE.

the ratio of $G^I(i\omega)$ to $G^R(i\omega)$ refers to the loss factor which is representing the viscoelastic damping and it is shown as

$$\tan \delta = \frac{G^I(i\omega)}{G^R(i\omega)}. \quad (39)$$

According to the corresponding references [11–13], experimental results showed that the storage modulus linearly increases with vibration frequency in most cases, and both the storage modulus and the loss modulus linearly increase with external magnetic field strength in a certain range. Therefore, the storage modulus $G^R(i\omega)$ and the loss factor $\tan \delta$ can be approximately expressed by

$$G^R(i\omega) = \alpha_0 + \alpha_1\omega, \quad (40a)$$

$$\tan \delta = \beta_0, \quad (40b)$$

where the coefficients α_0 , α_1 , and β_0 depend only on the applied magnetic field strength.

4.2. MRE Noise Control System. To test the feasibility of the algorithm stated before, an MRE noise control system is constructed as shown in Figure 5. The system included the MRE, an electromagnetic device (not given in the figure), a noise generation device, and a measurement system. The MRE is made of silicone rubber filled with randomly dispersed carbonyl iron particles. The external magnetic field applied to MRE is generated by a DC electrical source. The measurement system includes M and L sensors which are used to record the excitation and response signals, respectively.

4.3. Simulation Experiment. In order to verify the performance of the algorithm, simulations are investigated in this section. Here, we apply the D-LMS algorithm, DR-LMS algorithm, and LMS algorithm to system identification [6], as shown in Figure 6.

In Figure 6, $x(n)$ is the system input, and $H(z)$ is an unknown system. In this system, the output of adaptive filter is desired to track the output of $H(z)$, $e(n)$ is the identification error, and we also choose $e(n)$ as the criterion to judge the performance of the algorithms.

4.3.1. Linear System with Nonlinear Input. This system can be described by the difference equation as below:

$$y(n) = 0.3y(n-1) - 0.6y(n-2) + f(x(n)). \quad (41)$$

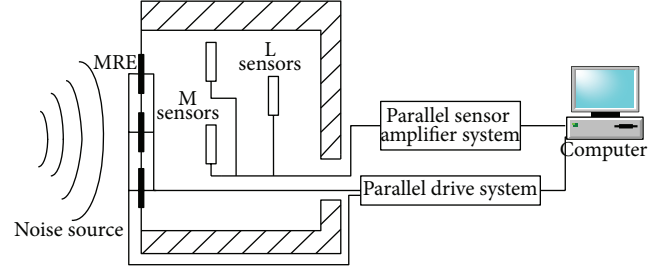


FIGURE 5: A sketch of the MRE noise control system.

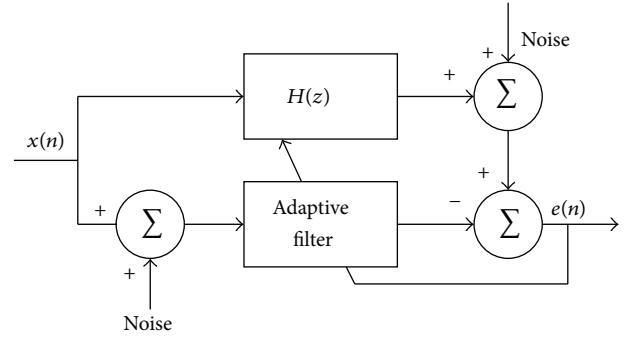


FIGURE 6: System identification.

TABLE 1: Simulation parameters.

Algorithm	Length	Step-size
LMS	32	0.0003
D-LMS	32	0.1185
DR-LMS	32	0.09

It is a linear dynamic system with a nonlinear input mapping $x(n)$ as the exciting signal. The nonlinear function $f(x)$ is shown as

$$f(x) = x^3 + 0.3x^2 - 0.4x. \quad (42)$$

Here,

$$x(n) = (\sin(2\pi n/20) + \sin(2\pi n/40) + \sin(2\pi n/50) + \sin(2\pi n/250)) \cdot 4.0^{-1}. \quad (43)$$

Table 1 shows the parameters chosen in this simulation. The simulation results are shown in Figures 7~9. The number of the iterations used to update weight vectors is different for different algorithm, while it takes 50 iterations for LMS algorithm but 20 iterations for D-LMS and DR-LMS algorithm. As seen in the figure, there is instability in system identification with LMS algorithm. Table 2 is the mean square error of system identification with different algorithm.

It is obvious that the MSE with D-LMS and DR-LMS algorithm are smaller for the same number of samples.

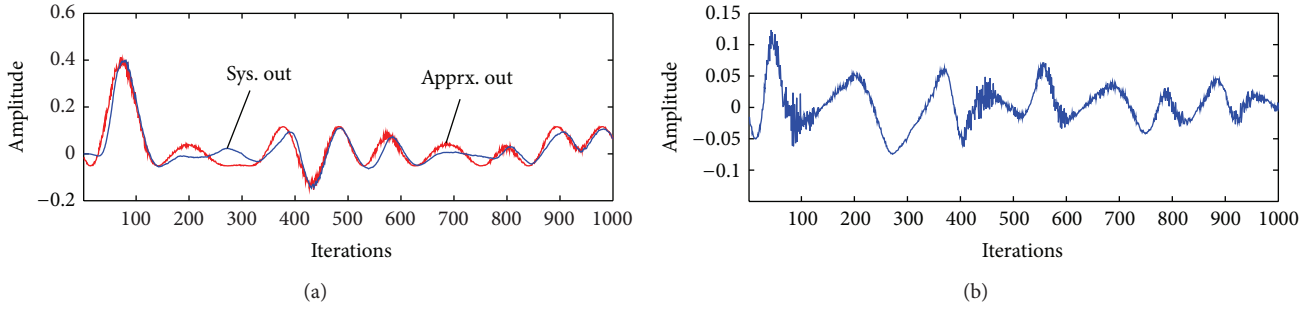


FIGURE 7: The simulation result with LMS algorithm. (a) Process of identification. (b) Error of identification.

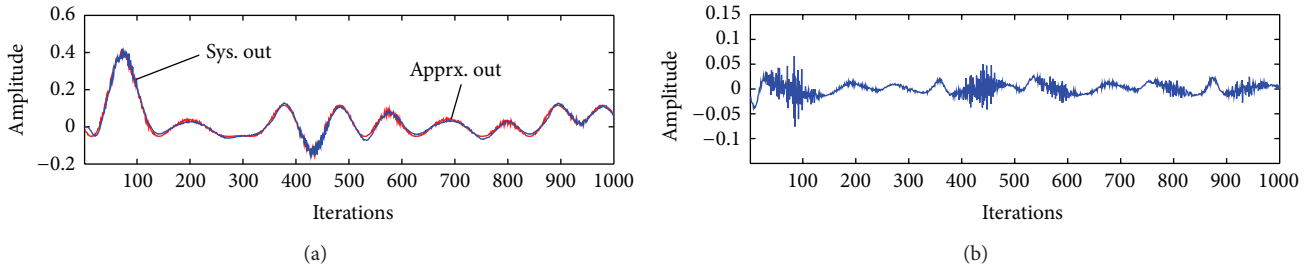


FIGURE 8: The simulation result with D-LMS algorithm. (a) Process of identification. (b) Error of identification.

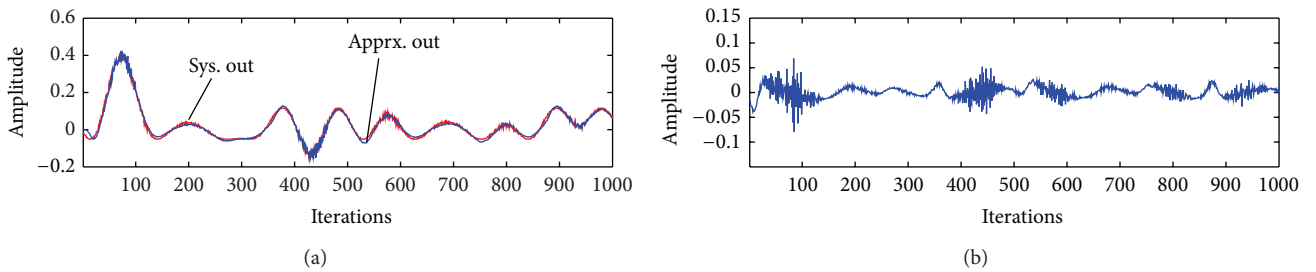


FIGURE 9: The simulation result with DR-LMS algorithm. (a) Process of identification. (b) Error of identification.

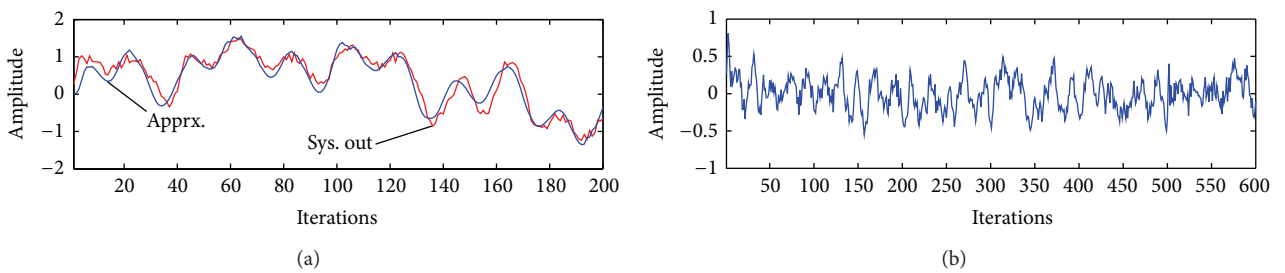


FIGURE 10: The simulation result with DLMS algorithm. (a) Process of identification. (b) Error of identification.

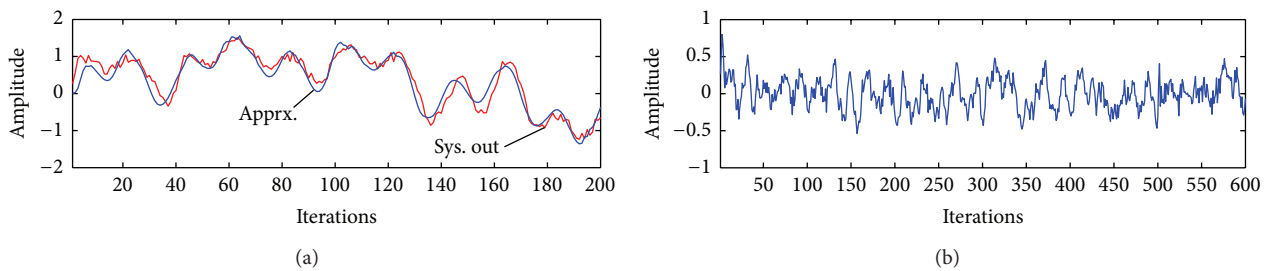


FIGURE 11: The simulation result with DR-LMS algorithm. (a) Process of identification. (b) Error of identification.

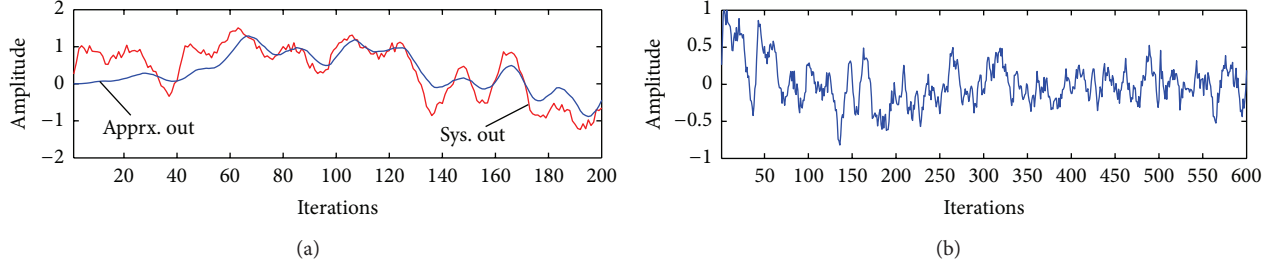


FIGURE 12: The simulation result with LMS algorithm. (a) Process of identification. (b) Error of identification.

TABLE 2: Mean square error (1024 data).

LMS	D-LMS	DR-LMS
4.662×10^{-4}	9.0604×10^{-5}	9.216×10^{-5}

4.3.2. *Nonlinear System with Linear Input.* This is an example of a nonlinear system which possesses nonlinear dynamics but linear input excitation. The system can be described by a nonlinear difference equation as

$$y(n) = \frac{y(n-1)}{1 + y^2(n-1)} + x(n) + w(n), \quad (44)$$

where $w(n)$ is the noise with uniform distribution and

$$x(n) = (\sin(2\pi n/20) + \sin(2\pi n/50) + \sin(2\pi n/250) + \sin(2\pi n/400)) \cdot 4^{-1}. \quad (45)$$

The simulation parameters are the same as the previous simulation in Table 1.

As shown in Figure 12, the convergence rate of identification with LMS algorithm is slow, which takes about 70 iterations to obtain stabilization. After about 100 iterations, the mean square error is 0.0628 for 1024 samples. Figures 10 and 11 show that the convergence rates with D-LMS and DR-LMS are much faster. After 15 iterations the system can reach stable state. After about 100 iterations, the mean square errors with D-LMS and DR-LMS are 0.0365 and 0.0355, respectively, for 1024 samples.

5. Summary

In this study, two adaptive algorithms based on Wavelet are proposed and studied. To investigate the performance of the algorithms, the simulation for their application to MRE noise control system is constructed and explored in details. The results indicate that the wavelet adaptive algorithm possesses a good control effectiveness though it requires a great deal of calculation. The implementation of MRE noise control system with DR-LMS algorithm can significantly improve the performance of the control system.

Conflict of Interests

The authors declare that there is no conflict of interests regarding the publication of this paper.

Acknowledgment

This paper was supported by the National Natural Science Foundation of China (61373054).

References

- [1] B. Widrow and J. M. McCool, "A comparison of adaptive algorithms based on the methods of steepest descent and random search," *IEEE Transactions on Antennas and Propagation*, vol. 24, no. 5, pp. 615–637, 1976.
- [2] D. F. Marshall, W. K. Jenkins, and J. J. Murphy, "The use of orthogonal transforms for improving performance of adaptive filters," *IEEE Transactions on Circuits and Systems*, vol. 36, no. 4, pp. 474–484, 1989.
- [3] J. C. Lee and C. K. Un, "Performance of transform-domain LMS adaptive digital filters," *IEEE Transactions on Acoustics, Speech and Signal Processing*, vol. 34, no. 3, pp. 499–510, 1986.
- [4] Y. Zhang and P. A. Ioannou, "A new linear adaptive controller: design, analysis and performance," *IEEE Transactions on Automatic Control*, vol. 45, no. 5, pp. 883–897, 2000.
- [5] J. O. Chapa and R. M. Rao, "Algorithms for designing wavelets to match a specified signal," *IEEE Transactions on Signal Processing*, vol. 48, no. 12, pp. 3395–3406, 2000.
- [6] A. Gupta, S. D. Joshi, and S. Prasad, "A new method of estimating wavelet with desired features from a given signal," *Signal Processing*, vol. 85, no. 1, pp. 147–161, 2005.
- [7] Y. Qin, J. Wang, B. Tang, and Y. Mao, "Higher density wavelet frames with symmetric low-pass and band-pass filters," *Signal Processing*, vol. 90, no. 12, pp. 3219–3231, 2010.
- [8] J. D. Carlson and M. R. Jolly, "MR fluid, foam and elastomer devices," *Mechatronics*, vol. 10, no. 4-5, pp. 555–569, 2000.
- [9] M. Kallio, T. Lindroos, and S. Aalto, "The elastic and damping properties of magnetorheological elastomers," *Applied Material Research at VTT*, vol. 565, pp. 110–120, 2006.
- [10] Y. Q. Ni, Z. G. Ying, and Z. H. Chen, "Magneto-rheological elastomer (MRE) based composite structures for micro-vibration control," *Earthquake Engineering and Engineering Vibration*, vol. 9, no. 3, pp. 345–356, 2010.
- [11] J. M. Ginder, M. E. Nichols, L. D. Elie, and J. L. Tardiff, "Magneto-rheological elastomers: properties and applications," in *Smart Structures and Materials 1999: Smart Materials Technologies*, vol.

3675 of *Proceedings of SPIE*, pp. 131–138, Newport Beach, Calif, USA, July 1999.

- [12] G. Y. Zhou, “Complex shear modulus of a magnetorheological elastomer,” *Smart Materials and Structures*, vol. 13, no. 5, pp. 1203–1210, 2004.
- [13] H. Böse, “Viscoelastic properties of silicone-based magnetorheological elastomers,” *International Journal of Modern Physics B*, vol. 21, no. 28-29, pp. 4790–4797, 2007.

Research Article

Damping Force Tracking Control of MR Damper System Using a New Direct Adaptive Fuzzy Controller

Xuan Phu Do, Kruti Shah, and Seung-Bok Choi

Smart Structures and Systems Laboratory, Department of Mechanical Engineering, Inha University, Incheon 402-751, Republic of Korea

Correspondence should be addressed to Seung-Bok Choi; seungbok@inha.ac.kr

Received 24 October 2014; Revised 4 January 2015; Accepted 5 January 2015

Academic Editor: Sakdirat Kaewunruen

Copyright © 2015 Xuan Phu Do et al. This is an open access article distributed under the Creative Commons Attribution License, which permits unrestricted use, distribution, and reproduction in any medium, provided the original work is properly cited.

This paper presents a new direct adaptive fuzzy controller and its effectiveness is verified by investigating the damping force tracking control of magnetorheological (MR) fluid based damper (MR damper in short) system. In the formulation of the proposed controller, a model of interval type 2 fuzzy controller is combined with the direct adaptive control to achieve high performance in vibration control. In addition, H^∞ (H infinity) tracking technique is used in building a model of the direct adaptive fuzzy controller in which an enhanced iterative algorithm is combined with the fuzzy model. After establishing a closed-loop control structure to achieve high control performance, a cylindrical MR damper is adopted and damping force tracking results are obtained and discussed. In addition, in order to demonstrate the effectiveness of the proposed control strategy, two existing controllers are modified and tested for comparative work. It has been demonstrated from simulation and experiment that the proposed control scheme provides much better control performance in terms of damping force tracking error. This leads to excellent vibration control performance of the semiactive MR damper system associated with the proposed controller.

1. Introduction

Recently, magnetorheological (MR) fluids based devices are actively studied and some of devices such as shock absorber for passenger vehicles are commercialized. Many MR devices or MR systems especially are popularized in the field of aerospace, ship, automobile, and civil engineering for effective control of unwanted vibrations. It is well known that MR fluid is considered as one of smart fluids in which the rheological properties can be controlled by external stimuli such as magnetic field. On the other hand, the development of new control system for MR devices or systems is also continuously undertaking in which the objective goal is to guarantee both stability and robustness against disturbances or/and uncertainties. Based on this objective, several types of robust controllers have been developed in both indirect adaptive control and direct adaptive control manners. A model of direct adaptive control for output tracking was studied in [1] where H infinity tracking technique was used for adaptive model. An adaptive fuzzy control for MIMO system was presented in [2] in which the Lyapunov function

and mean-value theorem were combined with a fuzzy model to build adaptive model. An observer of adaptive fuzzy controller was presented in [3] in which the back-stepping design and the supply changing function technique were applied. An input saturation problem was treated with adaptive feedback fuzzy control in [4] where the back-stepping technique and Lyapunov function were used in building the adaptive model. A direct adaptive control using type 2 fuzzy model was presented in [5] where H infinity tracking technique was applied to attenuate the fuzzy approximation error and the system uncertainty. The linear matrix inequality fuzzy Lyapunov method was also studied in [6] which concentrated on modeling errors between real system and fuzzy model. Recently, a novel of adaptive sliding mode control was developed by authors in [7] in which a sliding mode controller and Lyapunov method were used for high control performance. Vibration control of MR damper using an adaptive neurofuzzy inference system was also conducted by authors in [8].

In application of feedback/feed-forward controls for tracking force of MR devices, there are several researches.

An idealized hysteretic model for MR was studied in [9] using a nonlinear hysteretic bi-viscous model. For seismic response reduction, a clipped-optimal control using acceleration feedback was studied in [10] in which the properties of MR damper were tested to provide good vibration control performance. A model of MR damper for bridge application was derived in [11] using a semiactive tuned mass damper. A combination of the feed-forward and feedback control was also presented in [12] for torque control of MR brake. On the other hand, in research of interval type 2 fuzzy model (IT2FM), many studies on the development of controller type have been undertaken. A comprehensive research about type-reduction of three groups, Karnik-Mendel (KM), closed-form representation, and combined KM-closed form representation, were presented in [13]. In this study, EIASC (Enhanced Iterative Algorithm with Stopping Condition), Wu-Tan (WT) algorithm, and Nie-Tan (NT) algorithm were used to reduce calculation cost. Another research concentrating on KM algorithm in IT2FM was studied in [14] in which all methods were evaluated based on KM method. In order to solve the bottle-neck problem in calculating of type reduction of IT2FM, a new method of combination of KM and NT method was presented in [15]. It is recognized from the above survey that the development of a new adaptive fuzzy controller which is robust to disturbances or/and uncertainties is a hot issue in many control systems including MR device or MR systems. The development of new IT2FM especially is a new horizon in design of new controllers to guarantee both stability and robustness against disturbances and uncertainties [13–15].

Consequently, the technical originality of this work is to propose a new direct adaptive fuzzy controller using both IT2FM and adaptation method based on H -infinity tracking technique for the robust damping force tracking control of a cylindrical MR damper. Thus, a final goal is to demonstrate superior control performances of the proposed new direct adaptive fuzzy controller compared with two existing adaptive fuzzy controllers [1, 2]. In order to clarify the difference from the previous work done by the authors [7], it is noted here that the previous study deals with the indirect adaptive fuzzy controller, while current study treats the direct adaptive fuzzy controller whose structure is much different from the indirect method. In order to achieve the final goal of this work, as a first step, a new interval type 2 fuzzy control system is formulated. Then, a new type of adaptive controller is designed based on H infinity tracking technique and Lyapunov method. Based on the mathematical model, a closed-loop control structure is built and experimentally realized for a small-sized MR damper. MR fluid used in this work is manufactured in the laboratory using plate-like iron particles. Its field-dependent rheological characteristics are different from general MR fluid containing spherical iron particles. In order to demonstrate superior control performance of the proposed controller, both tracking control of desired damping force of MR damper and vibration control performance are evaluated and compared with existing two controllers.

2. Interval Type 2 Fuzzy Logic System and NT Algorithm

The model of interval type 2 fuzzy logic system (IT2FLS) has been developed from the type 1 fuzzy logic system (T1FLS). The structure of IT2FLS includes five components: fuzzifier, rule base, inference engine, type reducer, and defuzzifier. The rule base of IT2FLS can be expressed as follows:

$$RB^j: \text{If } a_1 \text{ is } \mathbf{A}_1^j \text{ and } \dots \text{ and } a_n \text{ is } \mathbf{A}_n^j \text{ Then } B^j, \quad (1)$$

where \mathbf{A}_i^j ($i = 1, \dots, n; j = 1, \dots, m$) are fuzzy sets and $\mathbf{B}^j = b^j$ is the centroid of a consequent IT2FLS.

In this study, NT algorithm is utilized for finding output of IT2FM. In general, NT algorithm shows the best algorithm in calculation with minimum computational cost. Hence, the application of NT algorithm will save time of fuzzy calculation. The relationship between NT algorithm and IT2FM is shown in Figure 1. The defuzzification of the IT2FLS-NT is calculated from several steps as follows.

Step 1. Set up input vector $a_v = (a_1, a_2, \dots, a_n)$. This vector is also vector state of the system whose component a_i is defined as $a_i = \mathbf{A}_i^j$.

Step 2. Find $\mathbf{A}_i^j = [\underline{\mu}(a_i), \bar{\mu}(a_i)]$, where $\underline{\mu}(a_i)$ is lower value and $\bar{\mu}(a_i)$ is upper value of IT2FLS a_i .

Step 3. Calculate lower and upper firing values of IT2FLS $[\underline{f}_j, \bar{f}_j] = [\prod_{i=1}^n \underline{\mu}(a_i), \prod_{i=1}^n \bar{\mu}(a_i)]$ where \underline{f}_j is lower firing value and \bar{f}_j is upper firing value.

Step 4. Use NT algorithm for calculating of $[y_l; y_u]$. Here y_l is lower interval type 1 value and y_u is upper interval type 1 value given by

$$y_l = \frac{\sum_{j=1}^m \underline{f}_j b^j}{\sum_{j=1}^m (\underline{f}_j + \bar{f}_j)}; \quad y_u = \frac{\sum_{j=1}^m \bar{f}_j b^j}{\sum_{j=1}^m (\underline{f}_j + \bar{f}_j)}. \quad (2)$$

Step 5. Calculate defuzzification y_0 of IT2FLS as follows:

$$y_0 = y_l + y_u = \boldsymbol{\theta}^T \boldsymbol{\xi}_l + \boldsymbol{\theta}^T \boldsymbol{\xi}_u, \quad (3)$$

where $\boldsymbol{\theta} = [b^1, b^2, \dots, b^m]$, $\boldsymbol{\xi}_l = [\xi_l^1, \xi_l^2, \dots, \xi_l^m]$, and $\boldsymbol{\xi}_u = [\xi_u^1, \xi_u^2, \dots, \xi_u^m]$. It is remarked that $\boldsymbol{\theta}$ is consequent vector and $\boldsymbol{\xi}_l, \boldsymbol{\xi}_u$ are lower and upper consequent membership vectors, respectively.

3. New Direct Adaptive Fuzzy Controller

Consider a nonlinear system is governed by the following equation:

$$\dot{\mathbf{x}} = \mathbf{f}(\mathbf{x}) + \mathbf{g}(\mathbf{x}) u(t) + \mathbf{d}(\mathbf{t}), \quad (4)$$

where $\mathbf{f}(\mathbf{x}) \in R^n$ and $\mathbf{g}(\mathbf{x}) \in R^n$ are two unknown nonlinear function vectors, $u(t) \in R^1$ is control function, $\mathbf{d}(t) \in R^n$ is an external disturbance vector, $|\mathbf{d}(t)| \leq \delta \mathbf{d}$, where $\delta \mathbf{d} \in R^n$ is upper bound of $\mathbf{d}(t)$, and $\mathbf{x} = [x_1, x_2, \dots, x_n]^T = [x_1, \dot{x}_1, \dots, x_1^{(n-1)}]^T \in R^n$ is the state vector of the system. The function $\mathbf{f}(\mathbf{x})$ and $\mathbf{g}(\mathbf{x})$ can be expressed in two parts. One is a nominal function and the other is unknown bounded uncertainty as follows:

$$\begin{aligned} \mathbf{f}(\mathbf{x}) &= \mathbf{f}_0(\mathbf{x}) + \delta \mathbf{f}(\mathbf{x}); \quad 0 < |\delta \mathbf{f}(\mathbf{x})| < \|\delta \mathbf{f}\|_\infty, \\ \mathbf{g}(\mathbf{x}) &= \mathbf{g}_0(\mathbf{x}) + \delta \mathbf{g}(\mathbf{x}); \quad 0 < |\delta \mathbf{g}(\mathbf{x})| < \|\delta \mathbf{g}\|_\infty, \end{aligned} \quad (5)$$

where $\mathbf{f}_0(\mathbf{x}) = [x_2, \dots, x_n, f_0]^T$, $\mathbf{g}_0(\mathbf{x}) = [0, \dots, 0, g_0]^T$, $\delta \mathbf{f} = [0, 0, \dots, \delta f_0]^T$, and $\delta \mathbf{g} = [0, 0, \dots, \delta g_0]^T$. $\delta \mathbf{f}$ and $\delta \mathbf{g}$ are two positive vectors. Hence, the system (4) can be rewritten as

$$\dot{\mathbf{x}} = \mathbf{f}_0(\mathbf{x}) + \mathbf{g}_0(\mathbf{x}) u(t) + \mathbf{D}, \quad (6)$$

where $\mathbf{D} = \delta \mathbf{f} + \delta \mathbf{g} u(t) + \mathbf{d}(t)$ is uncertain part (disturbance) which can be redefined as $\mathbf{D} = [0, 0, \dots, D_0]^T$. Then, the relationship between system (6) and IT2FLS is determined based on (3) as follows:

$$\begin{aligned} \mathbf{f}_{00}(\mathbf{x}) &= \mathbf{f}_0(\mathbf{x}) \gamma_0 = \boldsymbol{\theta}_f \boldsymbol{\xi}_f, \\ \mathbf{g}_{00}(\mathbf{x}) &= \mathbf{g}_0(\mathbf{x}) \gamma_0 = \boldsymbol{\theta}_g \boldsymbol{\xi}_g, \end{aligned} \quad (7)$$

where $\boldsymbol{\theta}_f = [\boldsymbol{\theta}_f^l, \boldsymbol{\theta}_f^u]^T$ and $\boldsymbol{\theta}_g = [\boldsymbol{\theta}_g^l, \boldsymbol{\theta}_g^u]^T$, $\boldsymbol{\xi}_f = \boldsymbol{\xi}_g = [\xi_l, \xi_u]$. Note that $\boldsymbol{\theta}_f, \boldsymbol{\theta}_g$ are the centroids of consequent vectors and $\boldsymbol{\xi}_f, \boldsymbol{\xi}_g$ are consequent membership vectors of \mathbf{f}, \mathbf{g} , respectively. The difference between a desired output x_d and the measure output x is defined by $e = x_d - x$. Thus, the error vector for the system is defined as $\mathbf{E} = [e_0, e_1, e_2, \dots, e_{n-1}]^T = [e, \dot{e}, \ddot{e}, \dots, e^{(n-1)}]$, and a vector $\mathbf{K} = [k_n, k_{n-1}, k_{n-2}, \dots, k_0]$ is the chosen coefficients such that all of the roots of the polynomial $\sigma^n + k_{n-1}\sigma^{n-1} + k_{n-2}\sigma^{n-2} + \dots + k_0$ are located in the open left-half complex plane [1, 2].

In relation with fuzzy control, by assuming the disturbance of a direct adaptive fuzzy control is expressed as follows:

$$u = \frac{1}{g_f} (-f_{00}(x) + \dot{x}_d + \mathbf{K}^T \mathbf{E}), \quad (8)$$

where g_f is a fuzzified value of g . Using (6) and (8), the derivative of \mathbf{E} is expressed as follows:

$$\dot{\mathbf{E}} = \dot{\mathbf{x}}_d - \dot{\mathbf{x}} = \Lambda_1 \mathbf{E} + \Lambda_2 [(g_f - g)u + (f_{00}(x) - f(x))], \quad (9)$$

where

$$\Lambda_1 = \begin{bmatrix} 0 & 1 & 0 & \cdots & \cdots & 0 \\ 0 & 0 & 1 & \cdots & \cdots & 0 \\ \vdots & \vdots & \vdots & \vdots & \vdots & \vdots \\ 0 & 0 & 0 & \cdots & \cdots & 1 \\ -k_n & -k_{n-1} & -k_{n-2} & \cdots & \cdots & -k_1 \end{bmatrix}, \quad \Lambda_2 = \begin{bmatrix} 0 \\ 0 \\ \vdots \\ 0 \\ 1 \end{bmatrix}. \quad (10)$$

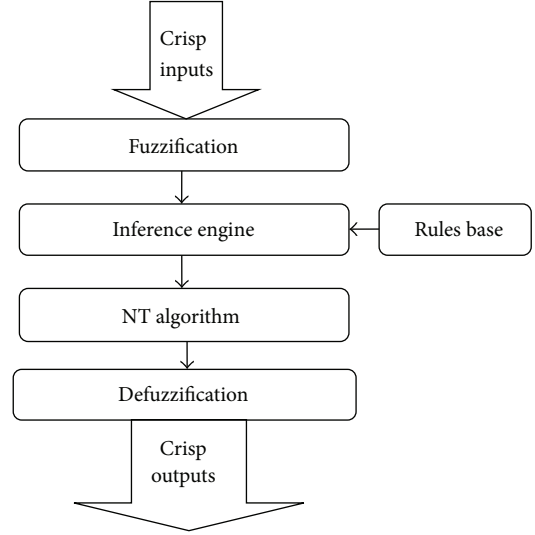


FIGURE 1: Relationship between IT2FLS model and NT algorithm.

Now, define the minimum approximation error as follows:

$$w = (f_{00}^*(x) - f(x)) + g_f u. \quad (11)$$

Then, substituting (11) into (9) yields the following equation:

$$\dot{\mathbf{E}} = \Lambda_1 \mathbf{E} + \Lambda_2 [(f_f^* - \theta_f) \xi_f - g u + w]. \quad (12)$$

Let $\gamma_f = (f_f^* - \theta_f)$. From (12), the equivalence control u_1 is defined as

$$u_1 = \frac{1}{g} (\hat{\gamma}_f \xi_f), \quad (13)$$

where $\hat{\gamma}_f$ is the estimates of γ_f . It is noteworthy that the equation u_1 is established without the minimum approximation error w . Due to the presence of fuzzy approximation error and equivalent control term, using only u_1 is not sufficient to ensure the stability of the closed-loop system. Therefore, it is necessary to add a robust compensator to deal with it as follows:

$$u_2 = \Gamma \xi_{fz} \frac{1}{g} \mathbf{E}^T \mathbf{P} \Lambda_2, \quad (14)$$

where Γ is an adaptive parameter, and $\mathbf{P} = \mathbf{P}^T \geq 0$ is a solution of the following Riccati-like equation:

$$\mathbf{P} \Lambda_1 + \Lambda_1^T \mathbf{P} + \mathbf{Q} - \Gamma \xi_{fz} \mathbf{P} \Lambda_2 \Lambda_2^T \mathbf{P} + \rho \mathbf{P} \Lambda_2 \Lambda_2^T \mathbf{P} = 0, \quad (15)$$

where $\rho \geq \Gamma$, ρ is a prescribed attenuation level, and $\mathbf{Q} = \mathbf{Q}^T \geq 0$, ξ_{fz} is consequent membership value of the IT2FLS. The resulting fuzzy control is determined as follows:

$$u = u_1 + u_2 = \frac{1}{g} (\hat{\gamma}_f \xi_f) + \Gamma \xi_{fz} \frac{1}{g} \mathbf{E}^T \mathbf{P} \Lambda_2. \quad (16)$$

By substituting (16) into (12), (16) can be rewritten as

$$\dot{\mathbf{E}} = \Lambda_1 \mathbf{E} + \Lambda_2 [\tilde{\gamma}_f \xi_f - \Gamma \xi_{fz} \mathbf{E}^T \mathbf{P} \Lambda_2 + w], \quad (17)$$

where $\tilde{\gamma}_f = \gamma_f - \hat{\gamma}_f$.

Now, in order to prove the stability of the control system, consider the Lyapunov function candidate as follows:

$$V = \frac{1}{2} \mathbf{E}^T \mathbf{P} \mathbf{E} + \frac{1}{2\alpha_1} \tilde{\gamma}_f^2 + \frac{1}{2\alpha_2} \Gamma^2. \quad (18)$$

Then, the derivative of (18) is expressed as follows:

$$\begin{aligned} \dot{V} = & -\frac{1}{2} \mathbf{E}^T \mathbf{Q} \mathbf{E} - \rho \mathbf{E}^T \mathbf{P} \Lambda_2 \Lambda_2^T \mathbf{P} \mathbf{E} \\ & + \left(\frac{1}{\alpha_2} \dot{\Gamma} - \frac{1}{2} \xi_{fz} \Gamma \mathbf{E}^T \mathbf{P} \Lambda_2 \Lambda_2^T \mathbf{P} \mathbf{E} \right) \\ & + \frac{1}{2} (w^T \Lambda_2^T \mathbf{P} \mathbf{E} + \mathbf{E}^T \mathbf{P} \Lambda_2 w) \\ & + \frac{1}{\alpha_1} (\alpha_1 \mathbf{E}^T \mathbf{P} \Lambda_2 \xi_f + \dot{\tilde{\gamma}}_f) \tilde{\gamma}_f. \end{aligned} \quad (19)$$

From (19), adaptation laws are established as follows:

$$\dot{\tilde{\gamma}}_f = -\alpha_1 \mathbf{E}^T \mathbf{P} \Lambda_2 \xi_f, \quad \dot{\Gamma} = \frac{\alpha_2}{2} \xi_{fz} \mathbf{E}^T \mathbf{P} \Lambda_2 \Lambda_2^T \mathbf{P} \mathbf{E}. \quad (20)$$

Applying (20), (19) is determined as follows:

$$\dot{V} \leq -\frac{1}{2} \mathbf{E}^T \mathbf{Q} \mathbf{E} + \frac{1}{4\rho} w^2. \quad (21)$$

By integrating (21) from $t = 0$ to $t = T$, the following equation is obtained:

$$V(T) - V(0) + \frac{1}{2} \int_0^T \mathbf{E}^T \mathbf{Q} \mathbf{E} dt - \frac{1}{4\rho} \int_0^T w^2 dt \leq 0, \quad (22)$$

where $V(0) = (1/2) \mathbf{E}^T(0) \mathbf{P} \mathbf{E}(0) + (1/2\alpha_1) \tilde{\gamma}_f^2(0) + (1/2\alpha_2) \Gamma^2(0)$. The group $[V(T) - V(0)]$ is always more than or equal to zero value. Hence, from (22), the remained group $[(1/2) \int_0^T \mathbf{E}^T \mathbf{Q} \mathbf{E} dt - (1/4\rho) \int_0^T w^2 dt]$ is analyzed as follows:

$$\frac{1}{2} \int_0^T \mathbf{E}^T \mathbf{Q} \mathbf{E} dt \leq \frac{1}{2} \|\mathbf{E}_Q\|^2 \leq \frac{1}{4\rho} \int_0^T w^2 dt \leq \left(\frac{1}{2\sqrt{\rho}} \right)^2 \|w\|^2. \quad (23)$$

Since the value is set by $\rho > 0$ and $Q > 0$, the error of matrix \mathbf{E} and the gain of w must be equal to or less than $(1/2\sqrt{\rho})$. Hence, the H infinity tracking form is satisfied [2, 16], and then (21) is always less than zero value (Lyapunov stability). Now, from the boundedness of parameters of $\tilde{\gamma}_f$, Γ is guaranteed by closed sets defined as follows:

$$\begin{aligned} \Omega_1 = & \{ \tilde{\gamma}_f \mid \|\tilde{\gamma}_f\| \leq L_f \}, \quad \Omega_2 = \{ \Gamma \mid \|\Gamma\| \leq L_\Gamma, \Gamma \xi_{fz} \leq \rho \}, \\ \Omega_{\delta_1} = & \{ \tilde{\gamma}_f \mid \|\tilde{\gamma}_f\| \leq L_f + \delta_1 \}, \\ \Omega_{\delta_2} = & \{ \Gamma \mid \|\Gamma\| \leq L_\Gamma + \delta_2, \Gamma \xi_{fz} + \delta_3 \leq \rho + \delta_2 \}, \end{aligned} \quad (24)$$

where $L_f, L_\Gamma, \delta_1, \delta_2$ are the choosing parameters. Hence the adjusted adaptation laws are redefined as

$$\dot{\tilde{\gamma}}_f = \begin{cases} -\alpha_1 \mathbf{E}^T \mathbf{P} \Lambda_2 \xi_f & \text{if } \|\tilde{\gamma}_f\| < L_f \text{ or } (\|\tilde{\gamma}_f\| = L_f, \mathbf{E}^T \mathbf{P} \Lambda_2 \xi_f \tilde{\gamma}_f \geq 0) \\ -\alpha_1 \mathbf{E}^T \mathbf{P} \Lambda_2 \xi_f + \alpha_1 \frac{(\|\tilde{\gamma}_f\|^2 - L_f)}{\delta_1 \|\tilde{\gamma}_f\|^2} \mathbf{E}^T \mathbf{P} \Lambda_2 \xi_f \tilde{\gamma}_f & \text{if } \|\tilde{\gamma}_f\| = L_f, \mathbf{E}^T \mathbf{P} \Lambda_2 \xi_f \tilde{\gamma}_f < 0, \end{cases} \quad (25)$$

$$\dot{\Gamma} = \begin{cases} \frac{\alpha_2}{2} \mathbf{E}^T \mathbf{P} \Lambda_2 \Lambda_2^T \mathbf{P} \mathbf{E} \xi_{fz} & \text{if } \|\Gamma\| < L_\Gamma \\ \text{or } (\|\Gamma\| = L_\Gamma + \delta_2, \mathbf{E}^T \mathbf{P} \Lambda_2 \Lambda_2^T \mathbf{P} \mathbf{E} \xi_{fz} \Gamma \geq 0) \\ \frac{\alpha_2}{2} \mathbf{E}^T \mathbf{P} \Lambda_2 \Lambda_2^T \mathbf{P} \mathbf{E} \xi_{fz} & \text{if } \|\Gamma\| = \rho, \mathbf{E}^T \mathbf{P} \Lambda_2 \Lambda_2^T \mathbf{P} \mathbf{E} \xi_{fz} \Gamma < 0. \\ -\alpha_2 \frac{(\|\Gamma\|^2 - L_\Gamma) \mathbf{E}^T \mathbf{P} \Lambda_2 \Lambda_2^T \mathbf{P} \mathbf{E} \xi_{fz} \Gamma}{\delta_2 \|\Gamma\|^2} \end{cases} \quad (26)$$

To observe the states of system, an observer for the nonlinear system is needed to converge the estimated state of $\tilde{x}(t)$. In this work, the observer is constructed by the Luenberger observer [17] which is defined as follows:

$$\dot{\tilde{x}}(t) = \mathbf{f}(\tilde{x}(t)) + \mathbf{g}\tilde{u}(t) + [\mathbf{Q}_{\text{ob}}(\tilde{x}(t))]^{-1} \mathbf{W} [y(t) - \tilde{y}(t)], \quad (27)$$

where $\mathbf{W} = [W_1, W_2, \dots, W_n]$ is a finite gain vector, $\mathbf{W} \in R^n$, \mathbf{Q}_{ob} is the observability matrix of the system. From the above analysis, the closed-loop of the proposed controller is shown in Figure 2. In Figure 2, adaptation laws use output of IT2FLS-NT model and error of system for calculating adaptive values of f and Γ . These values are input of fuzzy controller u which is input of observer and plant modules. Output of plant is input of IT2FLS-NT model and base for finding error of system which is also input of IT2FLS-NT model. Value of output observer is also base for calculating error of system.

4. MR Fluid and MR Damper

4.1. New MR Fluid. As mentioned in Introduction, MR fluid is suspension of microsized magnetic particles dispersed in a nonmagnetic carrier liquid [18–20]. It is smart fluid whose properties can be controlled by the magnetic field intensity. In the absence of magnetic field, the properties of the fluid are isotropic, while in the presence of magnetic field the magnetized particles form chain aligned in the direction of the field which results in the appearance of the field-dependent yield stress. Reversible transition from solid to liquid is also possible. Most of MR fluids developed so far have spherical iron particles. Recently, it has been reported

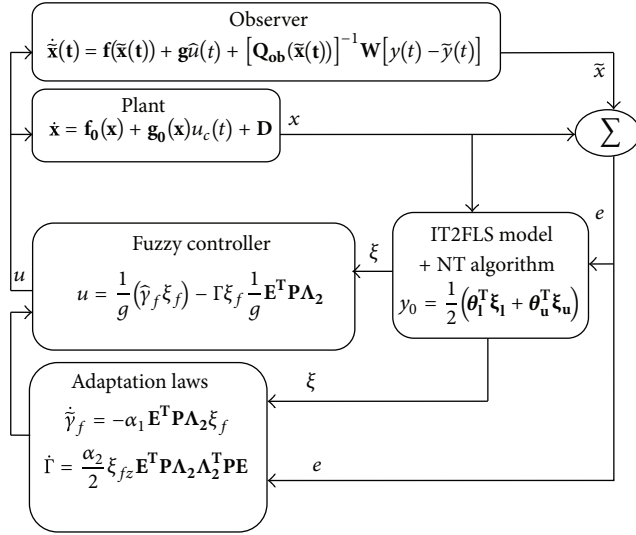


FIGURE 2: Closed-loop structure of the proposed controller.

that MR fluid containing plate-like iron particles provides better performance than MR fluid featuring spherical iron particle in terms of sedimentation characteristic [21, 22]. Therefore, in this work, a new type of bidisperse MR fluid is used for the application to MR damper. In order to undertake this work, two different sizes of plate-like iron particles are prepared. It consists of iron plate-like particles by weight of two different average diameters suspended in a heavy paraffin oil (64cSt) using mechanical stirrer. Iron microsized particles (Industrial Metal Powder, Pune, India) having average particle size $2 \mu\text{m}$ (small size) and $19 \mu\text{m}$ (large size) are used to prepare MR fluid. The structural property of micron-sized magnetic particle is characterized by an X-ray diffractometer, D2-phaser (Bruker XRD, Germany). Bidisperse MR fluid sample is prepared with a variable weight fraction (weigh of small size particles (W_s)/weight of large size particles (W_L)) of 4.00. The particle density is about 7.8 g cm^{-3} . A small amount of stabilizer is then added, stirred, and homogenized for a long time till good dispersion is achieved. Figure 3 shows the X-ray diffraction pattern of plate-like iron particles recorded at room temperature. The XRD result matches with the reported value of Fe given in the literature [23]. The magnetization measurement is carried out using a home-built magnetometer. The magnetization saturation of the particles used in this work is about $1250 \pm 15 \text{ kA m}^{-1}$. In a field gradient, alignment of the magnetic moment of large size particle is faster compared with the small-sized particle. Under this condition, initial susceptibility and saturation magnetization of larger particles is higher compared with the smaller particle. As a result, the fraction magnetization rises as the weight fraction increases.

Rheological properties in static mode for the MR sample are measured using a Physica MCR 301 (Anton Paar, GmbH, Austria) parallel plate rheometer coupled with a commercial magnetorheological device (MRD 180/IT magnetorheological cell). A diameter of plate is 20 mm and a gap between parallel disks is kept to 1 mm during whole

experiment. The magnetic circuit is designed so that the magnetic flux lines are normal to the parallel disk. Magnetic field is perpendicular to the velocity direction. When the magnetic field is applied the shear stress increases quickly with increasing shear rate as shown in Figure 3(a). The shear stress increases with increasing magnetic field strength due to enhancement of magnetic dipole-dipole interactions between the particles. This means that the MR fluid behaves as a Bingham fluid, where a yield stress is needed to initiate flow in the fluid. The Bingham model only applies for the linear portion of the stress-shear rate curve at high shear rate where the suspension flows like a Newtonian liquid [24]. According to this model shear stress is obtained by

$$\tau = \tau_B + \eta_p \dot{\gamma}, \quad (28)$$

where τ is the shear stress, τ_B is the Bingham yield stress caused by the applied magnetic field strength H , and η_p is the field independent plastic viscosity defined as the slope of the shear-stress curve at higher shear rate. The dynamic yield stress value increases with increasing magnetic field strength as shown in Figure 3(b). The data fitted in the second order polynomial equation is expressed as follows:

$$\tau_B = C_0 + C_1 H + C_2 H^2. \quad (29)$$

In the case of bidisperse suspension of micron-sized magnetic particles due to low applied magnetic field, a pair of short-chain segments forms from the large size particles first. When the external field increases, the substitution of small particles by large particles in a chain would have the effect of weakening the chain structure formed under shearing. The main reason to use bidisperse MR fluid is because it produces a higher yield stress compared with monodisperse suspension. The maximum yield stress generated is 38 kPa at 228 kA m^{-1} . In application point of view, the yield stress is the most important rheological parameter. The sedimentation rate of this MR fluid is 0.3% per day. The characteristics of bidisperse MR fluids are listed in Table 1.

4.2. Model of MR Damper. In this work, a simple dynamic system model installed with MR damper shown in Figure 4 is considered. From Figure 4, the equation of motion can be derived by

$$m\ddot{x}_s + c\dot{x}_s + kx_s = F_s(t), \quad (30)$$

where m is the mass of piston inside damper, c is viscous damping, k is the accumulator stiffness, $F_s(t)$ is external force, and x_s is displacement. The value of c belongs to the damping force of MR damper given by

$$F_{MR} = \text{sgn}(\dot{x}_1) c |\dot{x}_1|^\Theta = \text{sgn}(x_2) c |x_2|^\Theta, \quad (31)$$

where sgn is signum function, $\Theta \in (0; 1]$. Substituting (31) into (30) and by defining the displacement x_s as a state

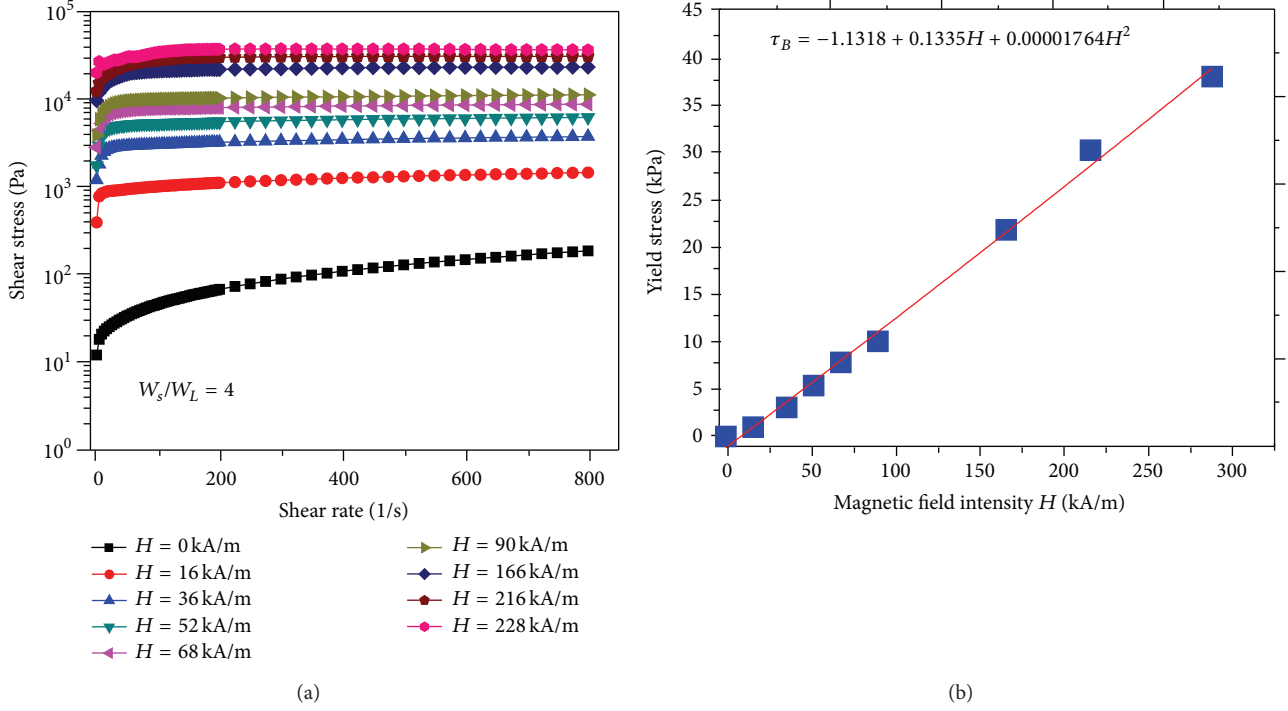


FIGURE 3: The field-dependent characteristics of the bidisperse MR fluid: (a) shear stress and (b) yield stress.

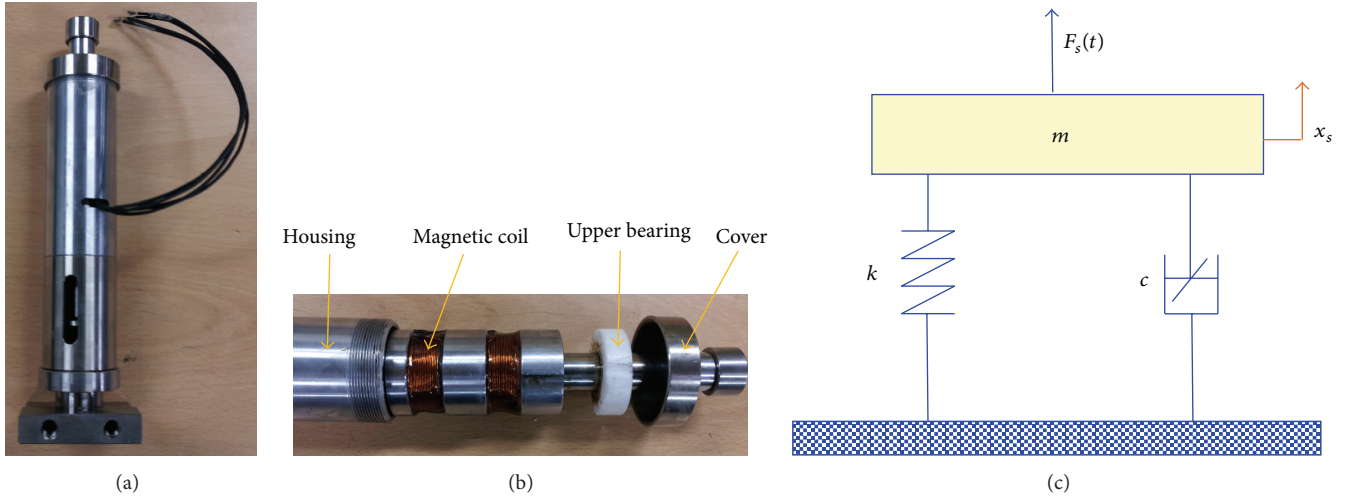


FIGURE 4: (a) MR damper, (b) inside core of MR damper, and (c) simple mechanical model.

variable x_1 yields the following equation of motion in a state space form:

$$\begin{aligned} \frac{dx_1}{dt} &= x_2, \\ \frac{dx_2}{dt} &= -\frac{k}{m}x_1 - \frac{x_2}{m|x_2|^\ominus}F_{MR} \operatorname{sgn}(x_2) + F_s. \end{aligned} \quad (32)$$

From (32), control u_c of the system is expressed by $u_c = F_{MR} \operatorname{sgn}(x_2)$, $f(x) = -(k/m)x_1$, and $g(x) = -[x_2/(m|x_2|^\ominus)]$. To change the system (32) into direct controller, the value

θ is chosen by 1. In this application, the semiactive control is applied in damping force control of MR damper. Hence, the damping force due to the yield stress of MR fluid can be expressed as follows [9]:

$$F_{MR} = \begin{cases} c_{p0}v - F & v \leq -v_1, \dot{v} > 0 \\ c_{pr}(v - v_0) & -v_1 \leq v \leq v_2, \dot{v} > 0 \\ c_{p0}v + F & v_2 \leq v, \dot{v} > 0 \\ c_{p0}v + F & v_1 \leq v, \dot{v} < 0 \\ c_{pr}(v + v_0) & -v_2 \leq v \leq v_1, \dot{v} < 0 \\ c_{p0}v - F & v \leq -v_2, \dot{v} < 0, \end{cases} \quad (33)$$

TABLE 1: Characteristics of MR fluid.

Properties	Value/limits
Base fluid	Hydrocarbon oil
System	Open or closed
Operating temperature	-23°C to 210°C
Viscosity [Pa·s]	
Shear rate 10 s ⁻¹	1.84 Pa·s
Shear rate 80 s ⁻¹	0.51 Pa·s
Setting (depend on device design)	The fluid is developed to settle softly and will remix with manual stirring 0.3% per day
Specific heat @ 25°C	
Density	2.04 gm/cm ³
Color	Dark gray
Weight percent of solids	63.82%
Flash point	>150°C

where c_{po} is the postyield viscous damping, c_{pr} is the preyield viscous damping, F is the yield force, v is velocity, v_1 is the decelerating velocity, and v_2 is the accelerating velocity. Values of v_1 and v_2 are found by parameters of c_{po} , c_{pr} , F . The u_c can be seen as the desired damping force of the system. From (32), the control u_c is the semiactive controller for damping force control of MR damper. On the other hand, the observer of the system to estimate the states can be designed by

$$\dot{\hat{\mathbf{x}}}(t) = \begin{bmatrix} \hat{x}_2 \\ f(\hat{x}_1, \hat{x}_2) \end{bmatrix} + \begin{bmatrix} 0 \\ g \end{bmatrix} u_c(t) + \begin{bmatrix} 1 & 0 \\ 0 & 1 \end{bmatrix} \begin{bmatrix} W_1 \\ W_2 \end{bmatrix} [Y - \tilde{Y}]. \quad (34)$$

The values of W_1 , W_2 are properly chosen by considering both stability and robustness of MR damper control system.

Now, the closed-loop control system for damping force control of MR damper is established as shown in Figure 5. Adaptation laws are used as the outputs of IT2FLS-NT model and the error of system to find adaptive values related f function and Γ in Riccati-like equation. The values of output of adaptation laws are input of the fuzzy controller module. The result of the fuzzy controller is input of damper controller, plant, and observer. It is remarked that damper controller supports the plant (MR damper) in control action. The measured force from the output of plant is used as the input for damper controller and IT2FLS-NT modules. The dynamical responses such as displacement and velocity of plant are used for IT2FLS-NT modules and for calculating error system. On the other hand, the output of the observer is also used for calculating error system and the value of error system is used for the input of IT2FLS-NT model.

TABLE 2: Centroid and rule of IT2FLS.

(a) Centroid of IT2FLS for controlling MR damper				
Rule base	\mathbf{e}_{21}	\mathbf{e}_{22}		
\mathbf{v}_{11}	$[-100 \ -80]$	$[-30 \ 0]$		
\mathbf{v}_{12}	$[0 \ 30]$	$[80 \ 100]$		
(b) Rule table of IT2FLS for controlling MR damper				
\mathbf{v}/\mathbf{e}	NL	NS	PS	PL
NL	1	0.67	0.33	0
NS	0.67	0.33	0	-0.33
PS	0.33	0	-0.33	-0.67
PL	0	-0.33	-0.67	-1

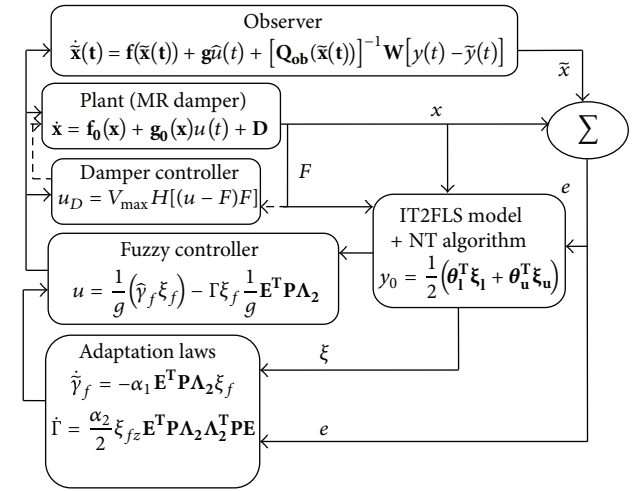


FIGURE 5: Closed-loop control structure for damping force control of MR damper.

5. Results and Discussions

5.1. Simulation Results. In order to verify high control performance of the proposed direct adaptive fuzzy controller, in this work both computer simulation and experimental realization are undertaken. The fuzzy rules are shown in Tables 2(a) and 2(b). The centroid of four rule bases of IT2FLS is formed by experiment tests based on trial and error method with considering maximal limit of damping force of MR damper. It is here remarked that the relationship between the centroids and rule bases in Table 2(b) has been clearly analyzed in [25, 26] in which the objective of controlled velocities is equal to or less than the exciting velocity, and the error force is also equal to or less than the limited force. The fuzzy models used in this work are shown in Figures 6(a) and 6(b). There are two parameters for these models: velocity of system and error of damping force. The values of fuzzy sets for velocity of \mathbf{v}_{11} , \mathbf{v}_{12} and error force of \mathbf{e}_{21} , \mathbf{e}_{22} are chosen as follows:

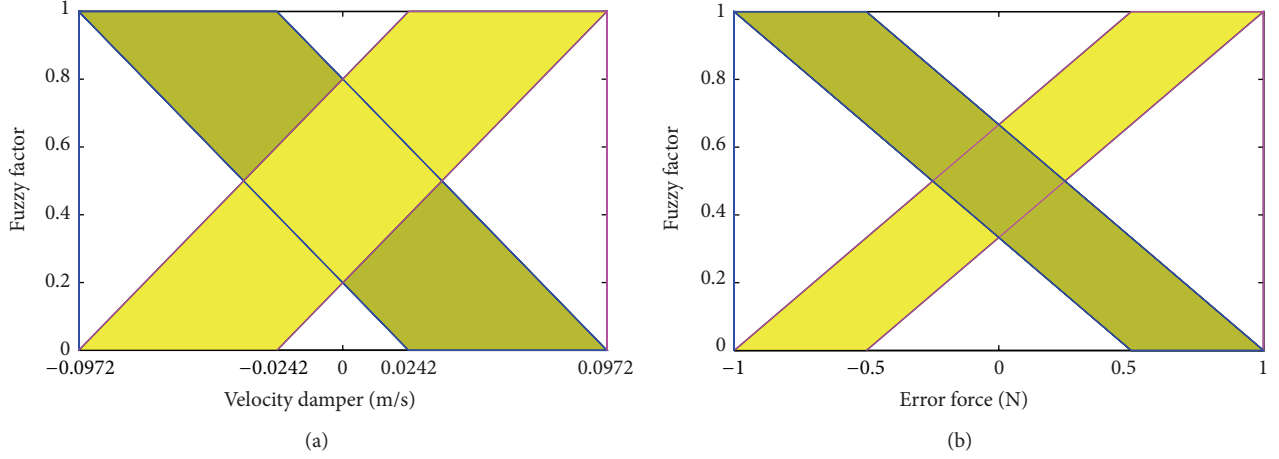


FIGURE 6: Definition of membership function: (a) velocity and (b) error.

$$\begin{aligned}
 \mathbf{v}_{11} &= [-0.0972 \quad -0.0972 \quad -0.0242 \quad 0.0972 \quad -0.0972 \quad -0.0972 \quad -0.0972 \quad 0.0242 \quad 1] \text{ (m/s)}, \\
 \mathbf{v}_{12} &= [-0.0972 \quad 0.0242 \quad 0.0972 \quad 0.0972 \quad -0.0242 \quad 0.0972 \quad 0.0972 \quad 0.0972 \quad 1] \text{ (m/s)}, \\
 \mathbf{e}_{21} &= [-1 \quad -1 \quad -0.5 \quad 1 \quad -1 \quad -1 \quad -1 \quad 0.5 \quad 1] \text{ (N)}, \\
 \mathbf{e}_{21} &= [-1 \quad 0.5 \quad 1 \quad 1 \quad -0.5 \quad 1 \quad 1 \quad 1 \quad 1] \text{ (N)}.
 \end{aligned} \tag{35}$$

In simulation of the proposed controller, the value Θ is chosen as 1 for direct controller and vector $\mathbf{K} = [1; 6]$. The initial value of Γ is chosen as 10, and the matrix \mathbf{Q} of Riccati-like equation is chosen as $\mathbf{Q} = [-10 \quad 0; 0 \quad -10]$. The constants α_1, α_2 are chosen as 20, 10, respectively. The excited frequency is set by 3 Hz. The matrix $[W_1 \quad W_2]^T$ for observer of the system is used by $[10 \quad 10]^T$. From the relation of damping force and control u_c in (32), the stability and robustness of the system will be evaluated by observing tracking performance of actual damping force to the desired force.

In this simulation, the desired force function for the system is chosen as $F_d = F_D \sin \omega_f t$, where F_D is desired magnitude of force set by $F_D = 70$ N, and ω_f is angular velocity where the frequency of the system f_f is set by 3 Hz. Based on the tracking performance of the damping force, the proposed controller is evaluated in terms of stability and robustness to disturbances. In progress of simulation, the output of control u_c is always evaluated with the desired value of the damping force. This guarantees that the output strictly appears according to the desired value. The external force F_s is chosen as $5 \sin(2\pi f_s t)$ where the frequency f_s is also used as 3 Hz. The initial states of the system are used as $[0 \quad 0.1]$ for both dynamic and observer states. The values of L_f, L_Γ are chosen as 20, 20, respectively. The values of δ_1, δ_2 are used as 0.05, 0.05, respectively. The simulation results on the damping force tracking of the proposed controller are shown in Figure 7. Actual force of the system tracks well the desired damping force as shown in Figures 7(a) and 7(b) which show

in 1 cycle. The stability of the system after nearly 60 s is shown in Figure 7(c). In this figure, the time of stability is long because the function $g(x)$ becomes a constant of the system, and the variable control u is applied directly into the system. This progress will take a longer time than indirect adaptive control. The stability is shown in Figure 7(d) in which the velocity of the system becomes small and stable. The applied current of the proposed control in 1 cycle and 100 s is shown in Figures 7(e) and 7(f), respectively. It is seen from Figure 7(a) that the input current is applied in the first time of cycle and holds its value throughout the control process.

In order to highlight good control performance of the proposed controller, a comparative work between the proposed and existing controllers is undertaken. In this work, two existing controllers which are similar to the proposed one are adopted and modified: Tong and Li [1] and Liu and Wang [2]. Adaptation laws in [1, 2] are modified by considering the dynamic model of MR damper which is used in the proposed control system. In simulation for Tong et al. controller, the control vector is used as $\mathbf{K} = [1; 13]$, value of Γ is set by 10, and the initial states of the system are used by $[0.01 \quad 0.1]$ for both dynamic and observer states. The values of L_f, δ_1 are chosen as 20, 0.05, respectively. The control results of Tong et al. controller are shown in Figure 8. It is seen from Figures 8(a) and 8(b) that the actual force is tracking well to the desired force. But the dynamic parameters such as displacement and velocity are unstable as shown in Figures 8(c) and 8(d). This phenomenon is from the performance of adaptation laws of Tong et al. controller

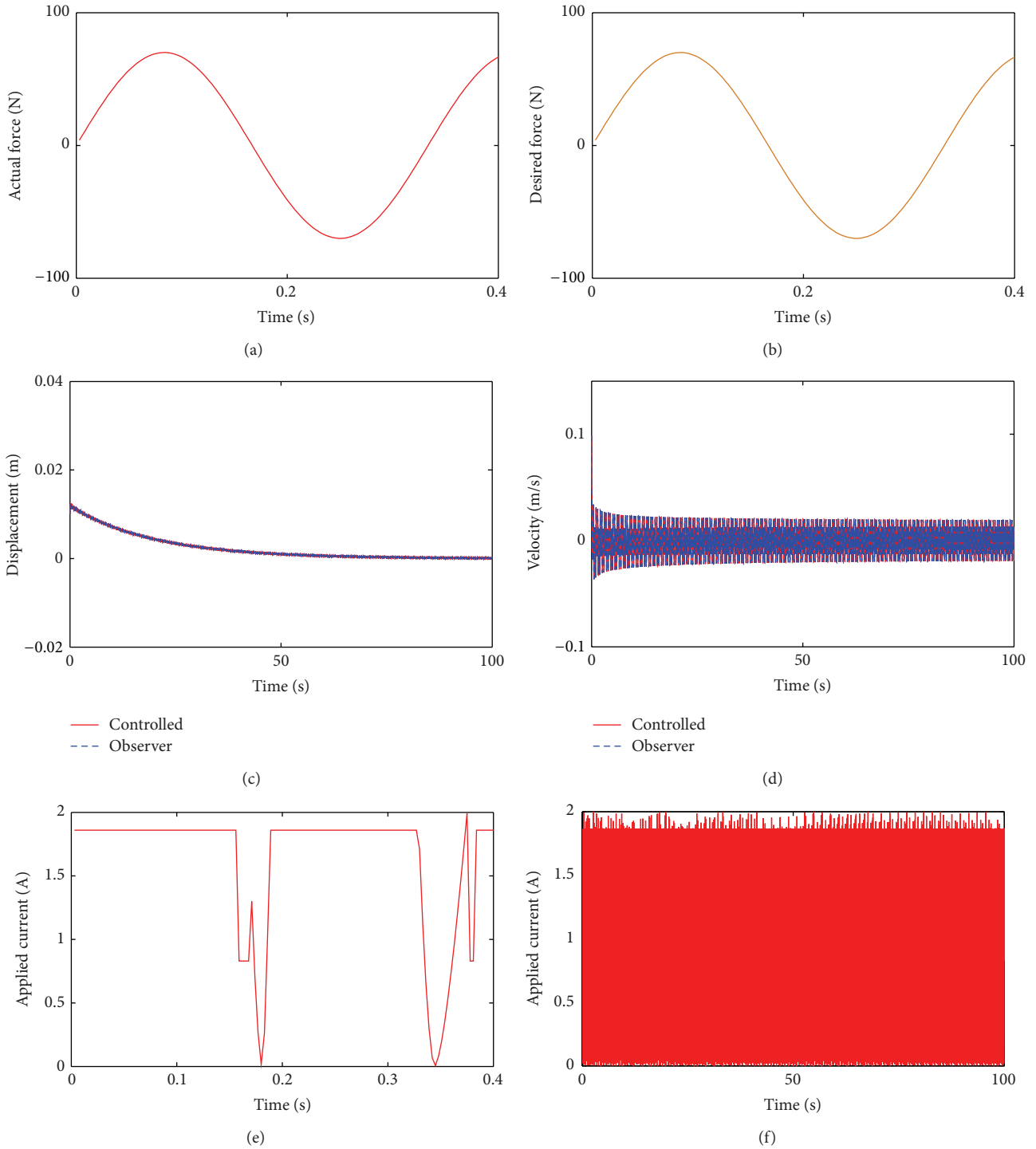


FIGURE 7: Simulation results at desired force 70 N and excited frequency 3 Hz (proposed controller): (a) actual force, (b) desired force, (c) displacement, (d) velocity, (e) applied current at 1 cycle (for 0.4 s), and (f) applied current for 100 s.

in which all parameters of Riccati-like equation are constant and are not changed through the control process. The applied current of Tong et al. controller is shown in Figures 8(e) and 8(f). It is observed that the results are different from the results shown in Figures 7(e) and 7(f) in which the current input is held and changed a little throughout the control

process. The second controller for comparison, Chen et al. controller, is adopted and modified in a same way of Tong et al. controller. It is noted that all setup parameters of Chen et al. controller are similar to Tong et al. controller. The control results of Chen et al. controller are shown in Figure 9. It is observed from results that control results of Chen et al.

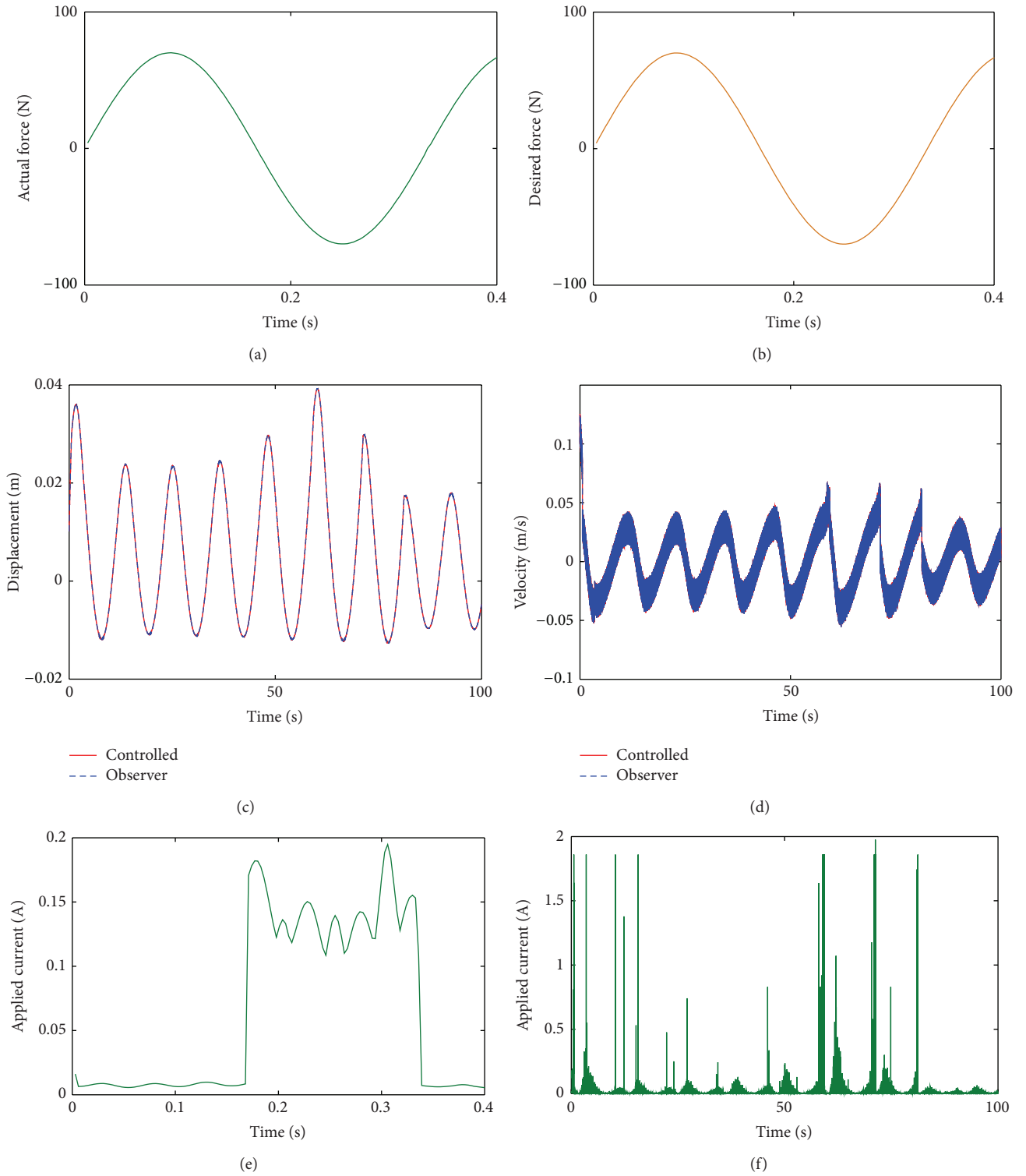


FIGURE 8: Simulation results at desired force 70 N and excited frequency 3 Hz (Tong et al.'s controller): (a) actual force, (b) desired force, (c) displacement, (d) velocity, (e) applied current at 1 cycle (for 0.4 s), and (f) applied current for 100 s.

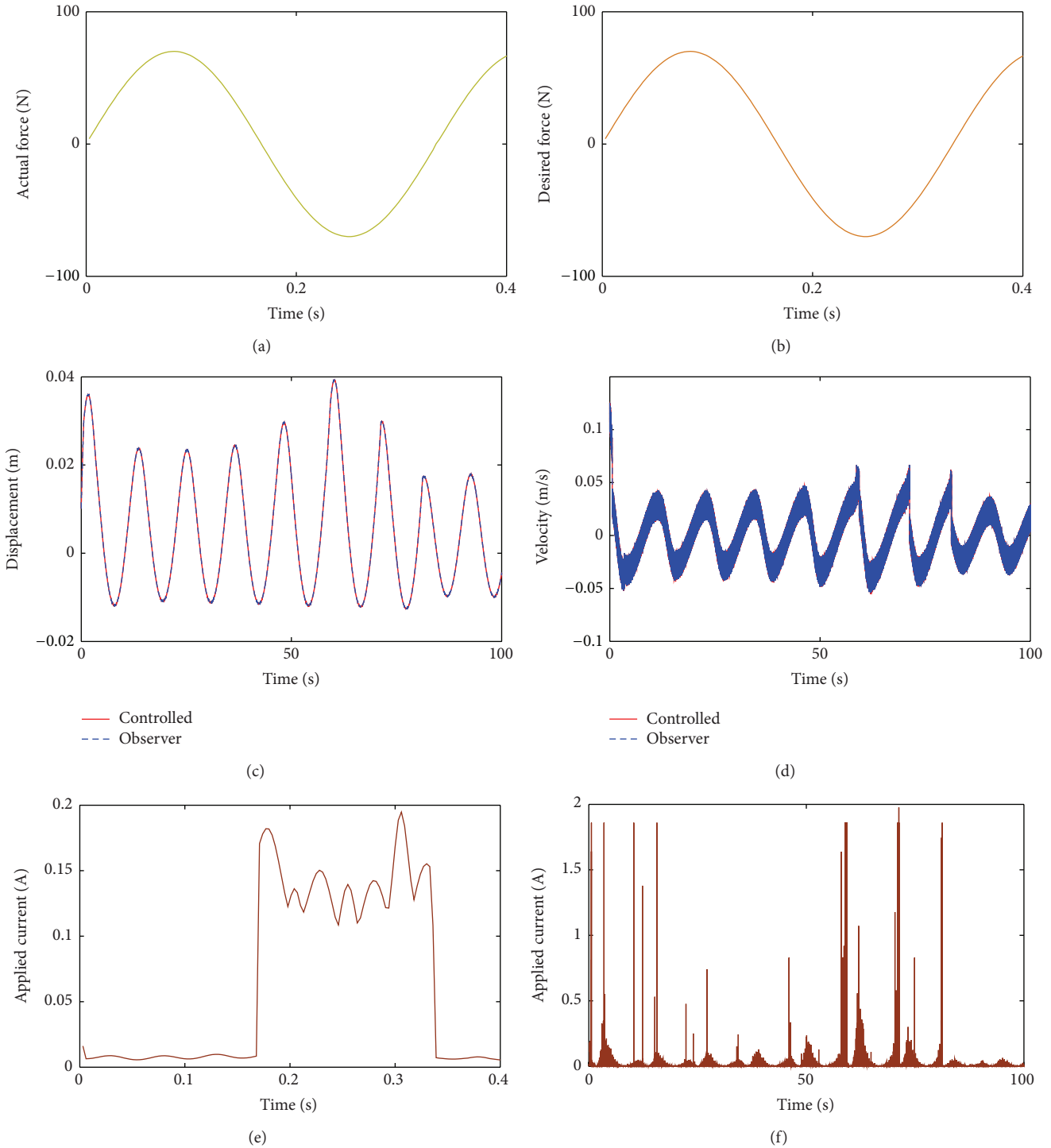


FIGURE 9: Simulation results at desired force 70 N and excited frequency 3 Hz (Chen et al’s controller): (a) actual force, (b) desired force, (c) displacement, (d) velocity, (e) applied current at 1 cycle (for 0.4 s), and (f) applied current for 100 s.

controller are almost the same as the Tong et al. controller. The applied currents of Tong et al. controller and Chen et al. controller are similar and the current magnitudes are lower than the proposed controller. This directly indicates that the energy consumption of the proposed controller is larger than the others. However, the proposed controller can guarantee

the robustness of the stability during control action, while Tong et al. controller and Chen et al. controller are not sufficient to retain the stability of the system due to the lack of the control robustness. From the above observations, the proposed controller provides much better tracking control performance than Tong et al. controller and Chen et al.

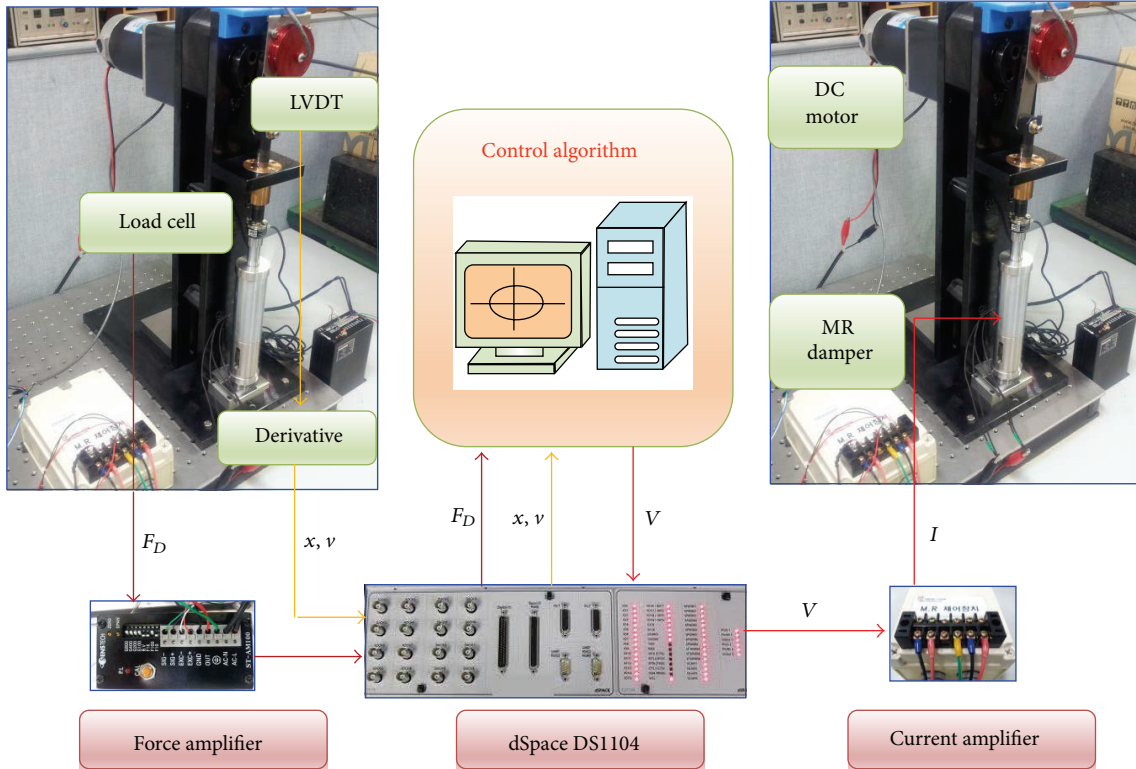


FIGURE 10: Experimental setup for damping force control of MR damper. V : voltage, v : velocity, and I : current.

controller. The proposed controller especially strongly and effectively ensures the robustness against the disturbances resulting in high control performance.

5.2. Experiment Results. In order to more clearly investigate superior control performances of the proposed controller, an experimental apparatus is set up as shown in Figure 10. Force signal is collected by a load cell 20 kgf, and signal force is changed by an amplifier built in dSpace box (DS1104). A wired-type LVDT (Linear Variable Differential Transformer) sensor is used for measuring dynamical response such as displacement and velocity. Exciting vibration is generated by DC motor, and control input from computer system through current amplifier box is applied to MR damper. From (4), the values of c_{p0} , c_{pr} , v_0 , v_1 , v_2 are determined as 941.37 Ns/m, 946.15 Ns/m, 0.073 cm/s, 0.101 cm/s, and 7.436 cm/s, respectively. The control objective in experiment is also to control damping force to follow the desired value.

Control results obtained from experimental realization of the controllers are shown in Figures 11 and 12. The desired force is chosen as 70 N. It is noted that the uncontrolled force (no applied current) and maximal force (maximal applied current) of damper are measured as 21 N and 120 N, respectively. In Figure 11, control results of the proposed controller are shown at four different exciting voltages: 6 V (Voltage), 8 V, 10 V, and 12 V. The exciting frequencies correlative with four voltages are 1.6 Hz, 2.1 Hz, 2.6 Hz, and 3.1 Hz, respectively. It is noted that the exciting voltages indicate the input to be directly applied to the motor. It

is seen that controlled force takes nearly 0.04 s to reach the desired force at on-state and 0.08 s at off-state. These times are not changed at four different excited voltages. The positive maximal controlled damping force in Figures 11(a1), 11(b1), 11(c1), and 11(d1) are obtained by 70.998 N, 70.997 N, 70.992 N, and 70.987 N, respectively. The positive minimal controlled damping force in Figures 11(a1), 11(b1), 11(c1), and 11(d1) are 70.098 N, 70.088 N, 70.266 N, and 70.577 N, respectively. The enlarged view of damping forces and control input currents at four excited voltages are shown in Figures 11(a2), 11(a3), 11(b2), 11(b3), 11(c2), 11(c3), 11(d2), and 11(d3). In Figures 11(a2), 11(b2), 11(c2), and 11(d2), it is obviously observed that the stability of the system is not good and hence causes poor tracking performance. It is also seen that the variation of damping force is larger than the proposed controller. From control signals shown in Figures 11(a3), 11(b3), 11(c3), and 11(d3), it is observed that the variation of input current is not large and the maximal control current applied to MR damper is identified by 1.86 A.

For comparison, Tong et al. controller is experimentally realized at same conditions as the controller proposed in this work. The control results are shown in Figure 12. The excited voltages are the same as the proposed controller as 6 V, 8 V, 10 V, and 12 V. The positive maximal controlled damping force in Figures 12(a1), 12(b1), 12(c1), and 12(d1) are obtained by 74.941 N, 73.916 N, 73.964 N, and 73.914 N, respectively. The positive minimal controlled damping force in Figures 12(a1), 12(b1), 12(c1), and 12(d1) are identified by 62.051 N, 63.490 N, 61.758 N, and 62.458 N, respectively. The enlarged

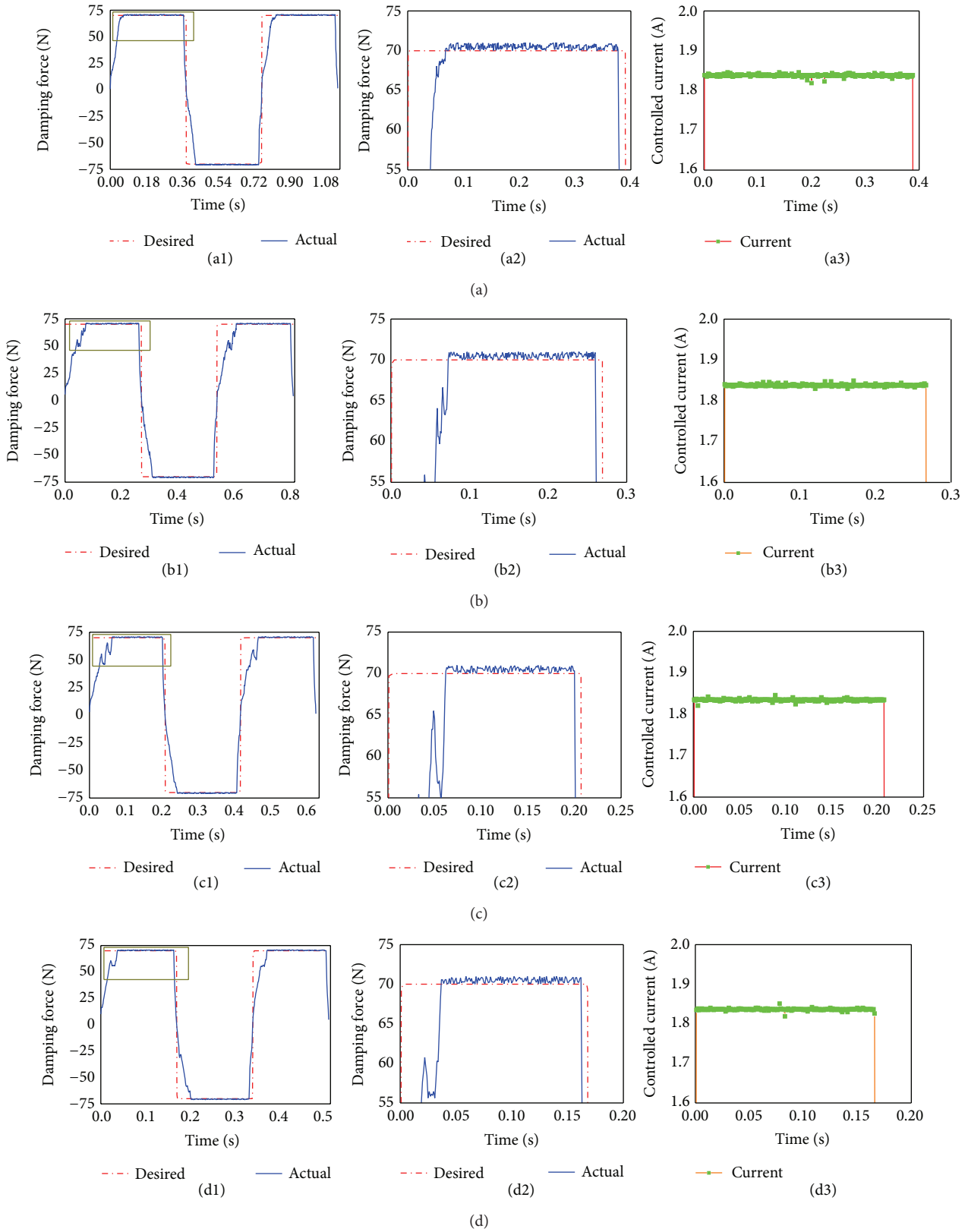


FIGURE 11: Experiment results of the proposed controller: (a1) damping force versus time at 6 V (Voltage), (a2) amplification of a's view, (a3) current at 6 V, (b1) damping force versus time at 8 V, (b2) amplification of b's view, (b3) current at 8 V, (c1) damping force versus time at 10 V, (c2) amplification of c's view, (c3) current at 10 V, (d1) damping force versus time at 12 V, (d2) amplification of d's view, and (d3) current at 10 V.

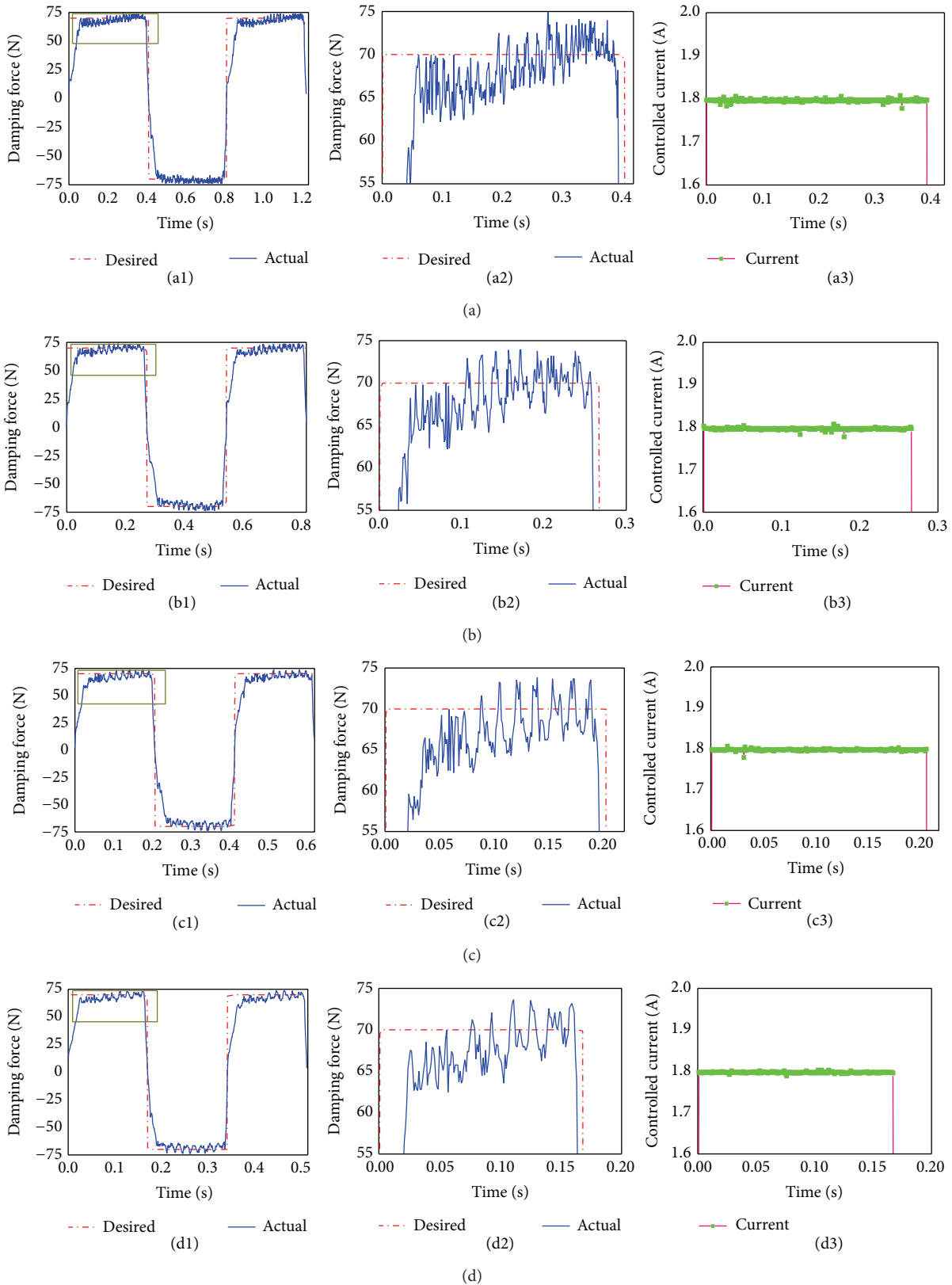


FIGURE 12: Experiment results of Tong et al. controller: (a1) damping force versus time at 6 V, (a2) amplification of a's view, (a3) current at 6 V, (b1) damping force versus time at 8 V, (b2) amplification of b's view, (b3) current at 8 V, (c1) damping force versus time at 10 V, (c2) amplification of c's view, (c3) current at 10 V, (d1) damping force versus time at 12 V, (d2) amplification of d's view, and (d3) current at 10 V.

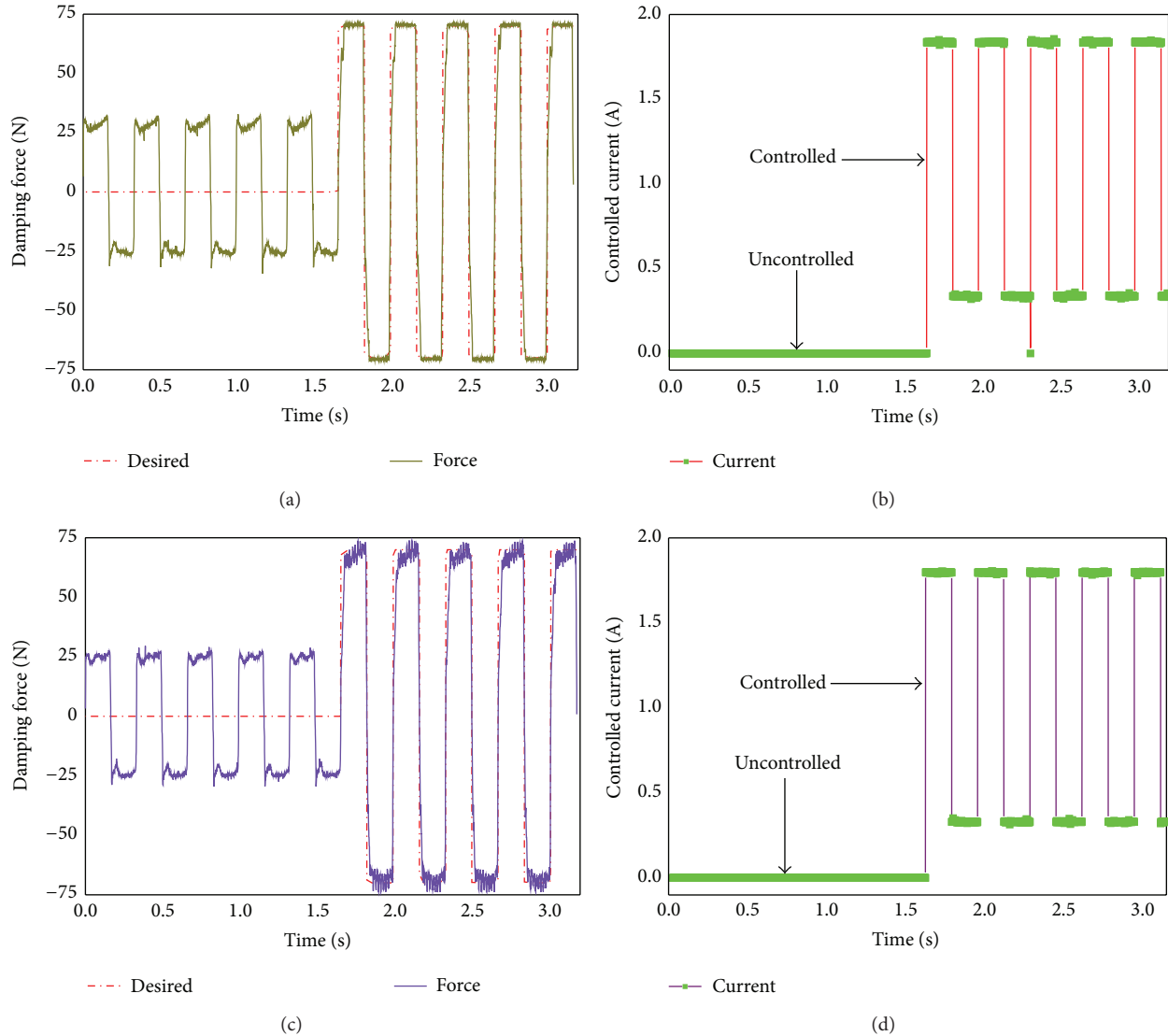


FIGURE 13: Damping force (DF) and controlled current (CR) of two controllers: (a) DF of proposed controller at 12 V, (b) CR of proposed controller at 12 V, (c) DF of Tong et al. controller at 12 V, and (d) CR of Tong et al. controller at 12 V.

view of damping forces and control input currents for four excited voltages are shown in Figures 12(a2), 12(a3), 12(b2), 12(b3), 12(c2), 12(c3), 12(d2), and 12(d3). In Figures 12(a2), 12(b2), 12(c2), and 12(d2), it is obviously observed that the stability of the system is not good, and hence this result in poor tracking performance. It is also seen that the variation of damping force is larger than the proposed controller. This indicates that Tong et al. controller cannot sufficiently control the disturbances and hence the robustness of the system is not fully guaranteed. From the input histories shown in Figures 12(a3), 12(b3), 12(c3), and 12(d3), it is seen that the variation of the control current is not large and the maximal control current is 1.83 A. Figure 13 presents tracking performance of damping force and corresponding applied control input. The positive force and negative force controlled with two different controllers are nearly 27 N and -27 N, respectively. It is clearly seen that the proposed controller is much better

than Tong et al. controller in term of tracking performance of damping force. This is because the proposed controller has adaptation law to overcome external disturbances, while Tong et al. controller does not have it.

6. Conclusion

In this work, a new direct adaptive fuzzy controller was developed and its superior control performance was verified through both simulation and experiment associated with MR damper system. The proposed controller was developed based on model of interval type 2 fuzzy and H^∞ tracking technique. For performance verification, MR damper containing plate-like iron particles was adopted and its damping force tracking was evaluated. In addition, two existing controllers of Tong et al. and Chen et al. were adopted and modified for comparative work with the proposed controller.

Control results achieved from simulation and experiment demonstrate that the proposed controller is much better than the others in terms of stability and robustness. This directly indicates the enhancement of damping force tracking performance of the filed-dependent damping force of MR damper of the proposed controller and hence excellent vibration control performance has been achieved. It has been also observed that Tong et al. controller and Chen et al. controller are not converged well and hence cannot sufficiently guarantee the robustness against the disturbance. It is finally remarked that the proposed direct adaptive fuzzy controller can be effectively utilized to numerous MR application control systems subjected to uncertainties or/and disturbances without significant modification.

Conflict of Interests

The authors declare that there is no conflict of interests.

Acknowledgment

This work was supported by a National Research Foundation of Korea (NRF) grant funded by the Korean Government (MEST) (no. 2010-0015090). This financial support is gratefully acknowledged.

References

- [1] S. Tong and H.-X. Li, "Direct adaptive fuzzy output tracking control of nonlinear systems," *Fuzzy Sets and Systems*, vol. 128, no. 1, pp. 107–115, 2002.
- [2] Y.-J. Liu and W. Wang, "Adaptive fuzzy control for a class of uncertain nonaffine nonlinear systems," *Information Sciences*, vol. 177, no. 18, pp. 3901–3917, 2007.
- [3] S. Sui, S. Tong, and Y. Li, "Observer-based adaptive fuzzy decentralized control for stochastic large-scale nonlinear systems with unknown dead-zones," *Information Sciences*, vol. 259, pp. 71–86, 2014.
- [4] Y. Li, S. Tong, and T. Li, "Adaptive fuzzy output-feedback control for output constrained nonlinear systems in the presence of input saturation," *Fuzzy Sets and Systems*, vol. 248, pp. 138–155, 2014.
- [5] F. Yang, R. Yuan, J. Yi, G. Fan, and X. Tan, "Direct adaptive type-2 fuzzy logic control of a generic hypersonic flight vehicle," in *Proceedings of the 4th International Conference on Intelligent Control and Information Processing (ICICIP '13)*, pp. 581–586, Beijing, China, June 2013.
- [6] C.-W. Chen, K. Yeh, K. F. Liu, and M.-L. Lin, "Applications of fuzzy control to nonlinear time-delay systems using the linear matrix inequality fuzzy Lyapunov method," *Journal of Vibration and Control*, vol. 18, no. 10, pp. 1561–1574, 2012.
- [7] D. X. Phu, N. V. Quoc, J.-H. Park, and S.-B. Choi, "Design of a novel adaptive fuzzy sliding mode controller and application for vibration control of magnetorheological mount," *Proceedings of the Institution of Mechanical Engineers Part C: Journal of Mechanical Engineering Science*, vol. 228, no. 13, pp. 2285–2302, 2014.
- [8] S. D. Nguyen and S.-B. Choi, "A novel minimum-maximum data-clustering algorithm for vibration control of a semi-active vehicle suspension system," *Proceedings of the Institution of Mechanical Engineers, Part D: Journal of Automobile Engineering*, vol. 227, no. 9, pp. 1242–1254, 2013.
- [9] N. M. Wereley, L. Pang, and G. M. Kamath, "Idealized hysteresis modeling of electrorheological and magnetorheological dampers," *Journal of Intelligent Material Systems and Structures*, vol. 9, no. 8, pp. 642–649, 1998.
- [10] S. J. Dyke, B. F. Spencer Jr., M. K. Sain, and J. D. Carlson, "Modeling and control of magnetorheological dampers for seismic response reduction," *Smart Materials and Structures*, vol. 5, no. 5, pp. 565–575, 1996.
- [11] F. Weber and M. Mašlanka, "Precise stiffness and damping emulation with MR dampers and its application to semi-active tuned mass dampers of Wolgograd Bridge," *Smart Materials and Structures*, vol. 23, no. 1, Article ID 015019, 2014.
- [12] R. Russo and M. Terzo, "Modelling, parameter identification, and control of a shear mode magnetorheological device," *Proceedings of the Institution of Mechanical Engineers. Part I: Journal of Systems and Control Engineering*, vol. 225, no. 5, pp. 549–562, 2011.
- [13] D. Wu, "Approaches for reducing the computational cost of interval type-2 fuzzy logic systems: overview and comparisons," *IEEE Transactions on Fuzzy Systems*, vol. 21, no. 1, pp. 80–99, 2013.
- [14] J. M. Mendel, "On KM algorithms for solving type-2 fuzzy set problems," *IEEE Transactions on Fuzzy Systems*, vol. 21, no. 3, pp. 426–446, 2013.
- [15] J. M. Mendel and X. Liu, "Simplified interval type-2 fuzzy logic systems," *IEEE Transactions on Fuzzy Systems*, vol. 21, no. 6, pp. 1056–1069, 2013.
- [16] Y. V. Orlov and L. T. Aguilar, *Advanced H_∞ Control Towards Nonsmooth Theory and Applications*, Birkhäuser, New York, NY, USA, 2014.
- [17] G. Ciccarella, M. Dalla Mora, and A. Germani, "A Luenberger-like observer for nonlinear systems," *International Journal of Control*, vol. 57, no. 3, pp. 537–556, 1993.
- [18] G. Bossis, S. Lacin, A. Meunier, and O. Volkova, "Magnetorheological fluids," *Journal of Magnetism and Magnetic Materials*, vol. 252, no. 1–3, pp. 224–228, 2002.
- [19] J.-I. Takimoto, K. Minagawa, and K. Koyama, "Numerical study of the response time of ER suspensions," *International Journal of Modern Physics B*, vol. 10, no. 23–24, pp. 3037–3044, 1996.
- [20] O. Volkova, G. Bossis, M. Guyot, V. Bashtovoi, and A. Reks, "Magnetorheology of magnetic holes compared to magnetic particles," *Journal of Rheology*, vol. 44, no. 1, pp. 91–104, 2000.
- [21] K. Shah, J.-S. Oh, S.-B. Choi, and R. V. Upadhyay, "Plate-like iron particles based bidisperse magnetorheological fluid," *Journal of Applied Physics*, vol. 114, no. 21, Article ID 213904, 2013.
- [22] K. Shah, D. X. Phu, and S. B. Choi, "Rheological properties of bi-dispersed magnetorheological fluids based on plate-like iron particles with application to a small-sized damper," *Journal of Applied Physics*, vol. 115, no. 20, Article ID 203907, 2014.
- [23] J. de Vicente, V. Fernando, J. P. Segovia-Gutiérrez, M. D. P. Morales, and R. Hidalgo-Álvarez, "Effect of particle shape in magnetorheology," *Journal of Rheology*, vol. 54, pp. 1337–1362, 2010.
- [24] B.-J. de Gans, H. Hoekstra, and J. Mellema, "Non-linear magnetorheological behaviour of an inverse ferrofluid," *Faraday Discussions*, vol. 112, pp. 209–224, 1999.
- [25] K. M. Passino, *Biomimicry for Optimization, Control, and Automation*, Springer, London, UK, 2005.
- [26] D. Wu, *Design and analysis of type 2 fuzzy logic systems [M.S. thesis]*, National University of Singapore, 2005.

Research Article

Adaptive Vibration Control System for MR Damper Faults

Juan C. Tudón-Martínez and Ruben Morales-Menendez

Tecnológico de Monterrey, Escuela de Ingeniería y Ciencias, Avenida Garza Sada No. 2501, 64849 Monterrey, NL, Mexico

Correspondence should be addressed to Juan C. Tudón-Martínez; jc.tudon.phd.mty@itesm.mx

Received 30 January 2015; Revised 29 April 2015; Accepted 4 May 2015

Academic Editor: Miao Yu

Copyright © 2015 J. C. Tudón-Martínez and R. Morales-Menendez. This is an open access article distributed under the Creative Commons Attribution License, which permits unrestricted use, distribution, and reproduction in any medium, provided the original work is properly cited.

Several methods have been proposed to estimate the force of a semiactive damper, particularly of a *magnetorheological* damper because of its importance in automotive and civil engineering. Usually, all models have been proposed assuming experimental data in nominal operating conditions and some of them are estimated for control purposes. Because dampers are prone to fail, fault estimation is useful to design adaptive vibration controllers to accommodate the malfunction in the suspension system. This paper deals with the diagnosis and estimation of faults in an automotive *magnetorheological* damper. A robust LPV observer is proposed to estimate the lack of force caused by a damper leakage in a vehicle corner. Once the faulty damper is isolated in the vehicle and the fault is estimated, an *Adaptive Vibration Control System* is proposed to reduce the fault effect using compensation forces from the remaining healthy dampers. To fulfill the semiactive damper constraints in the fault adaptation, an LPV controller is designed for vehicle comfort and road holding. Simulation results show that the fault observer has good performance with robustness to noise and road disturbances and the proposed AVCS improves the comfort up to 24% with respect to a controlled suspension without fault tolerance features.

1. Introduction

In general, a damper is characterized by [1] (a) the dimensional data, (b) operating factors, and (c) force characteristics. Dimensional data include the stroke, the length between mountings, diameters, and weight. Operating factors include the limitations on temperature, power dissipation, and cooling requirements, while the most fundamental characteristics are the magnitude and shape of the force; that is, force characteristics indicate how the force varies with respect to the velocity, production tolerances on these forces, friction effects, saturation, and so forth. When the damper fails, the force characteristics are modified.

According to the capability to adjust the force characteristics, the automobile dampers can be classified as *passive*, *active*, or *semiactive*. Passive dampers are only able to dissipate the energy and their damping characteristics are time invariant, while active ones are able to store, dissipate, and generate energy through a variable damping coefficient, but they are very expensive to apply because they require an external power supply. Semiactive dampers represent a good

solution to control the vertical vehicle dynamics using lower energy consumption and lower cost [2]. Different semiactive damper technologies have been examined, whose bandwidth oscillates from 0 to 30 Hz; the main technologies in the automotive industry are *electrohydraulic* dampers (EH), *pneumatic actuators* (PA), and *magneto/electrorheological* dampers (MR/ER).

In an automotive suspension control system, the damping force on a controllable shock absorber is adjusted to improve the comfort and/or safety of the passengers in a road vehicle, overcoming the weaknesses of passive suspensions. Because the cost-benefit ratio is better in semiactive suspensions than in active ones, the major interest of the control community related to automotive suspensions is focused on the semiactive suspension control. An extensive classification of different control strategies for semiactive dampers according to the type of manipulation (continuous or *on-off*), control goal (comfort, road holding, or both), type of control law to include the semiactiveness (*clipped*, *frequency adaptive*, *frequency switched*, and *measurement-based*), type of control design (model-based or free of model), and so forth is

presented in [3]. Indeed, without considering the nature of the control strategy, the interesting challenges of the semiactive suspension control problem are as follows [4]:

- (1) Realistic design according to the nonlinearities of the semiactive damper.
- (2) Constrained control according to the dissipativity and saturation of the damper to avoid impractical solutions, even if this actuator is partially faulty.
- (3) Multiobjective control design, that is, capable of improving the vehicle comfort with no compromise (and perhaps enhancement) for the road holding.
- (4) Feasibility of implementation: with adaptation to different damper technologies, small number of control inputs, and low computing cost to be programmed in microcontrollers.

An extensive work on semiactive suspension systems emphasizes that MR dampers are one of the best solutions to manage the compromise between the objectives of an automotive suspension control: comfort and road holding. MR dampers are as fast as the EH actuators with less power requirement than ER dampers and higher robustness to temperature variations; they are easier to manufacture and implement than EH dampers and to control than PA. Indeed, most of the existing work on semiactive damper modeling and control is based on the MR damping technology [1].

Several mathematical models are available to represent the nonlinear behavior of MR dampers. In general, they can be grouped as parametric and nonparametric models. Parametric models explain the physical phenomena in mathematical expressions, for instance, the classical viscoelastic-plastic models [5, 6], the phenomenological evolutive *Bouc-Wen* models [7–12], and the algebraic models [13–15]. On the other hand, coefficients of nonparametric structures do not have a physical meaning, for instance, fuzzy models [16, 17], statistical models [18], polynomial models [19–22], or models based on *artificial neural networks* (ANN) [23–29]. Usually, all aforementioned structures have presented good modeling results and/or good properties to design control modules; but when the damper is faulty, nothing can be said.

The most common fault in MR dampers is oil leakage [1]. There are different aspects that cause a damper leakage [30], which are related to bad installation, excessive use, damage by external devices, or bad design of control system that saturates the manipulation. The direct consequence of a faulty shock absorber is the loss of damping force that causes a performance reduction in the suspension capabilities (comfort and safety for passengers) at any driving situation. Recently, the *Linear Parameter-Varying* (LPV) control theory has been extended to *fault tolerant control* (FTC) systems to maintain the desired control goals as much as possible when a damper fault occurs. A scheduling parameter based on the load transfer is used to keep the equilibrium (comfort) when a semiactive damper fails in [31]; in [32], a supervisory system computes the compensation force that each healthy damper must add to reduce the fault effect, considering the semiactive constraints.

Recently, Tudón-Martínez [33] studied the effect of the oil leakage degree in the damping force using a commercial automotive shock absorber. Several degrees of oil leakage were implemented to analyze how the dynamic behavior of the MR damper is modified through the characteristic curves *force-velocity* (FV) and *force-displacement* (FD). Figure 1 shows that the friction effect is reduced proportionally to the oil leakage degree; the linear stiffness also is reduced when the oil leakage increases; the nonlinearity in the viscous damping is modified and evidently the saturation force decreases inversely proportional to the damper leakage.

Experimental data of a *Design of Experiments* (DoE) with central composite design [34] illustrate that the damper leakage can be represented as a fault model of multiplicative nature [33]. By using an extension of a parametric model structure, for instance, the algebraic model of Guo et al. [13], a faulty MR damper can be modeled by a parameter identification algorithm as a static equation. In this model representation, the nominal parameters do not change; only the fault parameter modifies the force characteristics.

Because the parameter estimation approaches are sensitive to noise measurements and their online adaptation can require many computational resources, a robust estimation of the faulty force is essential. Indeed, the accuracy of the fault estimation not only determines the damper condition; this information can be used also to design Adaptive Vibration Control Systems to accommodate the lack of force caused by the faulty MR damper [32, 35–37].

Most of the work in *Fault Detection and Isolation* (FDI) modules for automobile suspensions is based on analytical redundancy, such as the parity space theory [38, 39], robust filtering [40], and nonlinear-robust observers [35, 36, 41]. The above approaches perform well for sensor faults or even for actuator faults considering active dampers that do not have any constraint on the force characteristics, in contrast to an MR damper whose semiactiveness, friction, and force saturation constraint the actuator properties.

An *Adaptive Vibration Control System* (AVCS) based on a robust LPV observer used to estimate faults in an MR damper is proposed in this paper. By using an H_∞ design, the LPV-AVCS system is robust to the road disturbances and noisy measurements. The LPV approach enables embedding the nonlinearities of the vehicle dynamics into varying parameters such that the observer becomes linearly parameter dependent with internal stability and robust performance. The inclusion of the faulty damper constraints as scheduling parameters into the LPV/ H_∞ observer makes the fault estimation fulfill the semiactiveness of the shock absorber in a practical implementation. The AVCS, based also on the LPV framework, uses the fault estimation to compute the needed compensation force in the healthy MR shock absorbers of the vehicle to reduce the effect of lack of force caused by the faulty damper (comfort deterioration).

The outline of this paper is as follows: in the next section, the problem statement is formulated. Section 3 details the design of the FDI system used to diagnose damper faults and Section 4 describes the AVCS. Section 5 illustrates the case study to validate the proposed FDI strategy under different tests and discusses the results in the AVCS. Concluding

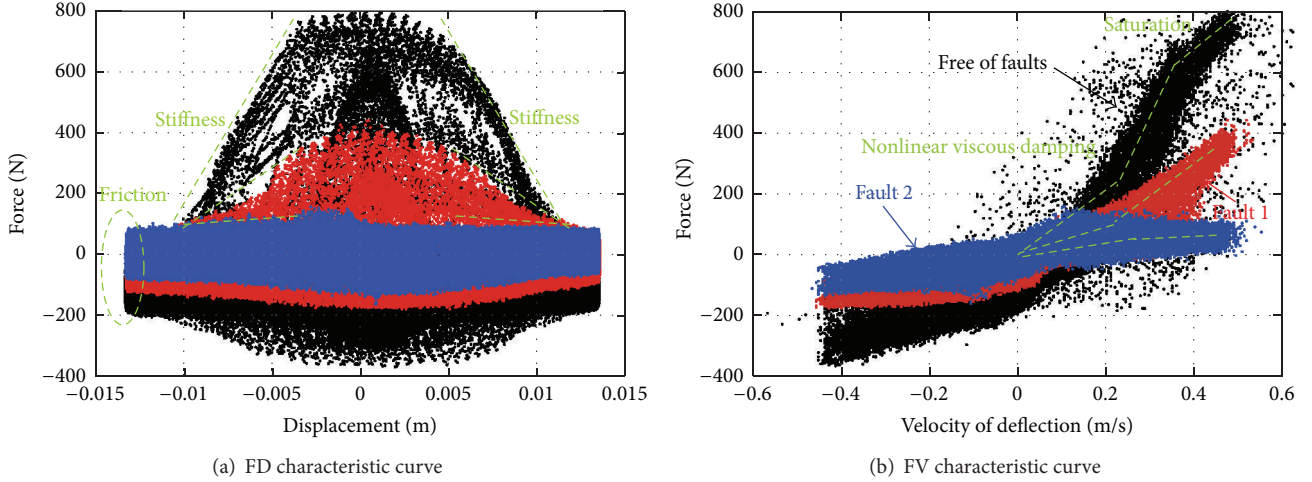


FIGURE 1: Experimental characteristic curves of a damper subject to leakages. Fault 1 represents 5% of oil leakage and fault 2 10%. The damper does not have control input value.

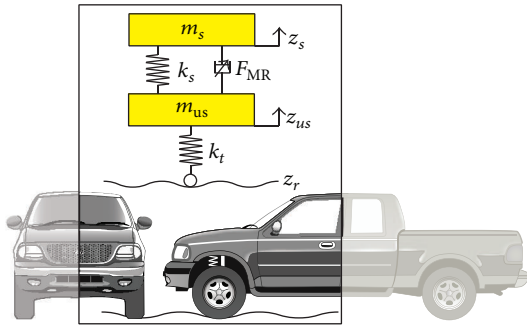


FIGURE 2: QoV model of an automotive semiactive suspension system.

remarks are presented in Section 6. The variables of this study are defined in the Abbreviations.

2. Problem Statement

The QoV model is the most basic system to represent an automotive suspension, Figure 2. Its use assumes an equivalent load distribution among the four corners and a linear dependency with respect to the translational and rotational chassis motions. The lateral and longitudinal wheel dynamics is not considered, while the wheel-road contact is ensured. The vertical dynamics of a QoV model is governed by

$$\begin{aligned} m_s \ddot{z}_s(t) &= -k_s [z_s(t) - z_{us}(t)] - F_{MR}(t), \\ m_{us} \ddot{z}_{us}(t) &= k_s [z_s(t) - z_{us}(t)] - k_t [z_{us}(t) - z_r(t)] \\ &\quad + F_{MR}(t). \end{aligned} \quad (1)$$

The system considers a sprung mass (m_s) and an unsprung mass (m_{us}). A spring with stiffness coefficient k_s and an MR shock absorber represent the suspension

between both masses. The spring is considered as linear because around 95% of its operating zone in an automotive application is linear; however, the MR damping force (F_{MR}) depends on a control input variable (electric current) and it is highly nonlinear with respect to the suspension motion. The stiffness coefficient k_t models the wheel tire. The vertical position of the mass m_s (m_{us}) is defined by z_s (z_{us}), while z_r corresponds to the unknown road disturbance. Because the MR damper represents the key element in the semiactive suspension control system, it is essential to model its nonlinearities and actuation properties with high accuracy to design model-based controllers, even more if the damper is faulty.

Consider an oil leakage on the MR damper in a QoV model, which induces a lack of force modeled as a multiplicative fault [33]; the faulty force expressed as a reduction of the nominal semiactive force F_{MR} is given by

$$\bar{F}_{MR}(t) = \alpha(t) F_{MR}(t), \quad (2)$$

where \bar{F}_{MR} is the reduced damping force and $\alpha \in (0, 1]$ is the fault parameter associated with the oil leakage degree; for example, $\alpha = 0.7$ means that the damping force will be of 70% of F_{MR} due to a lost force of 30%. Thus, if $\alpha = 1$, the semiactive damper is free of oil leakages. According to the nature of the oil leakage, the fault can be considered as abrupt (sudden leakage caused, e.g., by a seal worn out) or gradual (slow leakage caused, e.g., by wear).

To discriminate an operating change in the damping force (e.g., a change in the damper velocity, applied electric current, etc.) from a fault, a redundancy is needed (analytical or physical). In this paper the analytical redundancy consists in using a damper model and a nominal damper model, where both depend on the same variables except the fault. Another alternative is using redundant sensors (force, velocity, acceleration, pressure, etc.) to make the fault discrimination.

Inspired on the parametric damper model of Guo et al. [13], which has good balance between performance and complexity, the damper fault in (2) can be represented by

$$\begin{aligned}\bar{F}_{\text{MR}}(t) &= \alpha(t) \underbrace{[I(t) f_c \rho_1(t) + b_1 \dot{z}_{\text{def}}(t) + b_2 z_{\text{def}}(t)]}_{F_{\text{MR}}(t)} \\ &= F_{\text{MR}}(t) - F_{\delta}(t),\end{aligned}\quad (3)$$

where I is the electric current to control the MR force and $\rho_1(t) = \tanh[a_1 \dot{z}_{\text{def}}(t) + a_2 z_{\text{def}}(t)] \in [0, 1]$ represents the nonlinearities of the shock absorber. For $I = 0$, \bar{F}_{MR} reduces to the passive damping force of the suspension system. F_{δ} is then interpreted as the lack of damping force from the nominal one, caused by the oil leakage.

By using the degree of leakage α in an MR damper as a varying parameter in the QoV model dynamics, which is estimable by physical features of the shock absorber (pressure sensors, accelerometers, etc.), an LPV observer can be used to estimate the faulty force F_{δ} instead of using a parameter estimation algorithm for (3) that is sensitive to noise measurements.

By substituting (3) into the vertical model dynamics of (1), a state-space representation of the QoV model with a damper leakage can be obtained as

$$\begin{aligned}\begin{bmatrix} \dot{z}_s \\ \ddot{z}_s \\ \dot{z}_{us} \\ \ddot{z}_{us} \end{bmatrix} &= \underbrace{\begin{bmatrix} 0 & 1 & 0 & 0 \\ -\frac{h(\alpha)}{m_s} & -\frac{\alpha b_1}{m_s} & \frac{h(\alpha)}{m_s} & \frac{\alpha b_1}{m_s} \\ 0 & 0 & 0 & 1 \\ \frac{h(\alpha)}{m_{us}} & \frac{\alpha b_1}{m_{us}} & -\frac{h(\alpha) + k_t}{m_{us}} & -\frac{\alpha b_1}{m_{us}} \end{bmatrix}}_A \begin{bmatrix} z_s \\ \dot{z}_s \\ z_{us} \\ \dot{z}_{us} \end{bmatrix} \\ &+ \underbrace{\begin{bmatrix} 0 & 0 \\ 0 & -\frac{\alpha \cdot \rho_1 f_c}{m_s} \\ 0 & 0 \\ \frac{k_t}{m_{us}} & \frac{\alpha \cdot \rho_1 f_c}{m_{us}} \end{bmatrix}}_B \begin{bmatrix} z_r \\ I \\ u \end{bmatrix}, \\ \begin{bmatrix} z_{\text{def}} \\ \dot{z}_{\text{def}} \end{bmatrix} &= \underbrace{\begin{bmatrix} 1 & 0 & -1 & 0 \\ 0 & 1 & 0 & -1 \end{bmatrix}}_C \begin{bmatrix} z_s \\ \dot{z}_s \\ z_{us} \\ \dot{z}_{us} \end{bmatrix}\end{aligned}\quad (4)$$

with $h(\alpha) = k_s + \alpha b_2$.

By defining a generalized LPV plant $\Sigma(\theta)$ of the form of (5) using the faulty system matrices in (4), with $\theta : \{\alpha, \rho_1\}$, and augmented by the weighting function states as

$$\begin{aligned}\Sigma(\theta) &:= \begin{bmatrix} \dot{\xi} \\ z_{\infty} \\ y \end{bmatrix} \\ &= \begin{bmatrix} \mathcal{A}(\theta) & \mathcal{B}_1(\theta) & \mathcal{B}_2(\theta) \\ \mathcal{C}_1(\theta) & \mathcal{D}_{11}(\theta) & \mathcal{D}_{12}(\theta) \\ \mathcal{C}_2(\theta) & \mathcal{D}_{21}(\theta) & \mathcal{D}_{22}(\theta) \end{bmatrix} \begin{bmatrix} \xi \\ w \\ u_c \end{bmatrix},\end{aligned}\quad (5)$$

it is possible to design an LPV/ H_{∞} observer of F_{δ} asymptotically stable in all variations of θ , whose robust performance (estimation error) is defined as a control approach.

On considering that only one MR damper is faulty, the other three healthy MR dampers can be used for the fault compensation. Using the fault estimation (e.g., F_{δ_1} if the front-left MR damper is faulty), it is possible to determine the compensation forces F_{c_j} , $j = 2, 3, 4$, from the vertical vehicle dynamics in the center of gravity of a 7-DOF model, such that

$$\begin{aligned}m_{s_c} \ddot{z}_{s_c} &= -\left(F_{k_1} + F_{\text{MR}_1} - F_{\delta_1} + F_{k_2} + F_{\text{MR}_2} + F_{c_2} + F_{k_3} \right. \\ &\quad \left. + F_{\text{MR}_3} + F_{c_3} + F_{k_4} + F_{\text{MR}_4} + F_{c_4}\right), \\ I_{xx} \ddot{\theta} &= \left(F_{k_1} + F_{\text{MR}_1} - F_{\delta_1} - F_{k_2} - F_{\text{MR}_2} - F_{c_2}\right) t_f + \left(F_{k_3} \right. \\ &\quad \left. + F_{\text{MR}_3} + F_{c_3} - F_{k_4} - F_{\text{MR}_4} - F_{c_4}\right) t_r, \\ I_{yy} \ddot{\phi} &= \left(F_{k_4} + F_{\text{MR}_4} + F_{c_4} + F_{k_3} + F_{\text{MR}_3} + F_{c_3}\right) l_r - \left(F_{k_2} \right. \\ &\quad \left. + F_{\text{MR}_2} + F_{c_2} + F_{k_1} + F_{\text{MR}_1} - F_{\delta_1}\right) l_f,\end{aligned}\quad (6)$$

where $F_{k_i} = k_{s_i}(z_{s_i} - z_{us_i})$ are the stiffness forces of the springs and F_{MR_i} , with $i = \in [1, 4]$, are the nominal MR damping forces used in a free-fault case, and the compensation forces are specifically used to keep the balance in the vertical vehicle dynamics once a damper fails, such that

$$F_{\delta_1} - F_{c_2} - F_{c_3} - F_{c_4} = 0, \quad (7a)$$

$$-t_f F_{\delta_1} - t_f F_{c_2} + t_r F_{c_3} - t_r F_{c_4} = 0, \quad (7b)$$

$$l_r F_{c_4} + l_r F_{c_3} - l_f F_{c_2} + l_f F_{\delta_1} = 0; \quad (7c)$$

that is, the equilibrium only depends on the vehicle dimension parameters to make the load distribution.

The controlled force with fault adaptive features in a QoV is then composed by a nominal actuation ($I_n(F_{\text{MR}})$, free-fault case) and by a compensation actuation ($I_c(F_{\delta})$, at presence of faults). Using an LPV controller, it is possible to design an AVCS that fulfills the semiactiveness and saturation constraints of the damper when the compensation force F_{c_j} is added, such that the closed-loop system is

$$\dot{x} = \mathcal{A}_{\text{CL}}(\rho) \cdot x + \underbrace{\mathcal{B}_{1\text{CL}} \cdot (I_n + I_c)}_{K(\rho) \cdot x} + \mathcal{B}_{2\text{CL}} \cdot z_r, \quad (8)$$

$$y = \mathcal{C}_{\text{CL}}(\rho) \cdot x + \mathcal{D}_{1\text{CL}} \cdot (I_n + I_c) + \mathcal{D}_{2\text{CL}} \cdot z_r$$

with $K(\rho) = \sum_{i=1}^N \xi_i(\rho)K_i$ by appropriately choosing the gains K_i , $i = 1, \dots, N$, such that the closed-loop system $(\mathcal{A}_{CL}, \mathcal{B}_{1CL}, \mathcal{B}_{2CL}, \mathcal{C}_{CL}, \mathcal{D}_{1CL}, \mathcal{D}_{2CL})$ is asymptotically stable for all parameter variations. Two varying parameters are used in the controller design: ρ_1^* represents the semiactiveness of the MR damper and ρ_2^* its saturation that depends on the maximum damping force available for the compensation.

3. LPV/ H_∞ Fault Observer

On using the bounded parameter α , which represents a multiplicative damper fault in (2), it is possible to design an LPV/ H_∞ observer to determine the lack of force caused by the damper leakage.

3.1. LPV Modeling. From (4), an LPV model structure can be expressed as

$$\begin{aligned} \dot{x} &= A(\alpha) \cdot x + B(\alpha, \rho_1) \cdot u, \\ y &= C \cdot x. \end{aligned} \quad (9)$$

However, the model of (9) does not respect the polytopic solution because the system is parameter dependent on the input. In order to make B parameter independent and get a proper structure for the LPV based controller synthesis [22], the model in (9) is a state-augmented system by adding a low-pass filter $W_{\text{filter}} = \omega_f/(s+\omega_f)$ with state x_f and matrices (A_f, B_f, C_f) , such that the new LPV model is given by

$$\begin{aligned} \underbrace{\begin{bmatrix} \dot{x} \\ \dot{x}_f \end{bmatrix}}_{\dot{x}_p} &= \underbrace{\begin{bmatrix} A(\alpha) & B_1(\alpha, \rho_1) & C_f \\ 0_{1 \times 4} & A_f & \end{bmatrix}}_{A_p(\alpha, \rho_1)} \underbrace{\begin{bmatrix} x \\ x_f \end{bmatrix}}_{x_p} + \underbrace{\begin{bmatrix} B_2 \\ 0 \end{bmatrix}}_{B_{p1}} z_r \\ &+ \underbrace{\begin{bmatrix} 0_{4 \times 1} \\ B_f \end{bmatrix}}_{B_{p2}} I, \\ y &= \underbrace{\begin{bmatrix} C & 0_{2 \times 1} \end{bmatrix}}_{C_p} \begin{bmatrix} x \\ x_f \end{bmatrix}, \end{aligned} \quad (10)$$

where B_1 is the column matrix of B associated with I and B_2 is the column matrix of B associated with the road profile z_r in (4).

Scheduling Parameters. The LPV system in (10) includes 2 time-varying parameters, assuming that both can be estimated directly from measurements or by additional sensors. The formed polytope represents a quadrilateral polygon, whose vertices are given by the bounded values of $\rho_1 \in [-1, 1]$ and $\alpha \in (0, 1]$.

By defining the set of four *Linear Time-Invariant* (LTI) systems, the main idea is to design an LPV observer of the missing force caused by the damper leakage, whose convex combination is stable for all trajectories of the varying parameters by solving an LMI problem.

3.2. LPV/ H_∞ Observer Design. Based on the LPV model of (10), an LPV/ H_∞ observer is designed to estimate the damping force lost by the oil leakage in the shock absorber, adding robustness to unknown road disturbances. The frequency specification performance is to reduce the estimation error of the faulty force ($e = F_{\delta_{\text{model}}} - \widehat{F}_\delta(y)$); W_e represents the weighting function used to minimize the estimation error in the frequency range of interest for the suspension motion, while W_{z_r} shapes the road irregularities in the observer design in a frequency band of interest, even narrow-banded:

$$W_r = \frac{K_r \omega_r s}{s + \omega_r} \quad (11)$$

to add robustness to road disturbances,

$$W_e = \frac{K_e (s^2 + 2\zeta_{e_1} \omega_{e_1} s + \omega_{e_1}^2)}{s^2 + 2\zeta_{e_2} \omega_{e_2} s + \omega_{e_2}^2} \quad (12)$$

to add robustness to noisy measurements.

By considering the filtering specifications, the generalized plant $\Sigma(\alpha, \rho_1)$ used for the synthesis of the H_∞ observer is given by (13). Figure 3 shows the structure of its design:

$$\begin{aligned} \Sigma(\alpha, \rho_1) &:= \begin{bmatrix} \dot{\xi} \\ z_\infty \\ y \end{bmatrix} \\ &= \begin{bmatrix} \mathcal{A}(\alpha, \rho_1) & \mathcal{B}_1 & \mathcal{B}_2 & \mathbf{0} \\ \mathcal{C}_\infty(\alpha, \rho_1) & \mathbf{0} & \mathbf{0} & \mathcal{D}_\infty \\ \mathcal{C} & \mathbf{0} & \mathcal{C}_I & \mathbf{0} \end{bmatrix} \begin{bmatrix} \xi \\ w \\ I \\ u_c \end{bmatrix} \end{aligned} \quad (13)$$

with

$$\begin{aligned} \mathcal{A}(\alpha, \rho_1) &= \begin{bmatrix} A_p(\alpha, \rho_1) & \mathbf{0} \\ \mathbf{0} & A_w \end{bmatrix}, \\ \mathcal{B}_1 &= \begin{bmatrix} B_{p1} W_r \\ \mathbf{0} \end{bmatrix}, \\ \mathcal{B}_2 &= \begin{bmatrix} B_{p2} \\ \mathbf{0} \end{bmatrix}, \\ \mathcal{C}_\infty &= \begin{bmatrix} C_p & \mathbf{0} \\ \mathbf{0} & \mathbf{0} \end{bmatrix}, \\ \mathcal{C}_I &= \begin{bmatrix} \mathbf{0} \\ 1 \end{bmatrix}, \end{aligned} \quad (14)$$

where $\xi = [x_p \ x_w]^T$ such that x_p are the states in the vertical dynamics of the augmented QoV model of (10) and x_w are the vertical weighting functions states, $\mathcal{C}_\infty(\alpha, \rho_1)$ and \mathcal{D}_∞ represent the controlled output z_∞ with frequency specifications in W_e to minimize the estimation error $e(t)$ in the frequency band of interest, $y = [z_{\text{def}} \ \dot{z}_{\text{def}} \ I]^T$ is

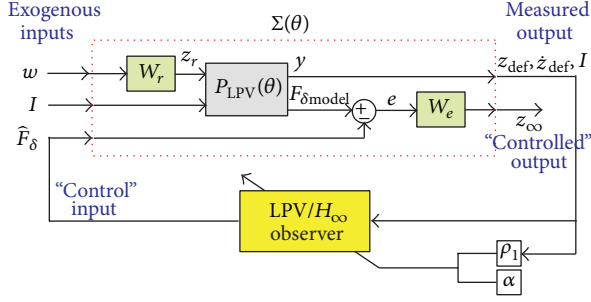


FIGURE 3: LPV/ H_∞ observer design in a QoV model to estimate the faulty force caused by a damper leakage (inspired as a control approach).

the measured output, w is the unknown disturbance, I is the electric current (manual actuation in open-loop), and $u_c = u^{H_\infty}$ is the observer output, in this case the estimated faulty force \hat{F}_δ which is considered as control input into the observer design, Figure 3.

The LPV/ H_∞ observer is given by

$$\begin{bmatrix} \dot{x}_o(t) \\ \hat{F}_\delta(t) \end{bmatrix} = \begin{bmatrix} A_o(\theta(t)) & B_o(\theta(t)) \\ C_o(\theta(t)) & D_o(\theta(t)) \end{bmatrix} \begin{bmatrix} x_o(t) \\ y(t) \end{bmatrix} \quad (15)$$

and is quadratically stable by solving an optimization problem with LMI techniques [42]. The observer reduces the effect of the road disturbances and avoids drifting in the estimation of the missed force by decreasing asymptotically the error dynamics.

Remark 1. Let $\Sigma(\theta_1, \dots, \theta_r)$ be the generalized plant of an LPV faulty model with matrices $\mathcal{A}(\theta_1, \dots, \theta_r)$, \mathcal{B}_i , \mathcal{C}_j , and \mathcal{D}_{ij} as in (13), where the input matrices are parameter independent as well as the output matrices; then it is possible to build a set of LMIs by applying the *Bounded Real Lemma*. To reduce the optimization problem into a finite number of LMIs, the solution is reached at each vertex of the polytope given by (16), by ensuring quadratic and robust stability in the closed-loop system [42, 43]:

$$\begin{aligned} \Sigma(\theta) &: \left[\begin{array}{c|c} A(\theta) & B(\theta) \\ \hline C(\theta) & D(\theta) \end{array} \right] \\ &= \sum_{i=1}^N \delta_i(\theta) \left[\begin{array}{c|c} A(\omega_i) & B(\omega_i) \\ \hline C(\omega_i) & D(\omega_i) \end{array} \right] \\ &\in Co \left\{ \left[\begin{array}{c|c} A_1 & B_1 \\ \hline C_1 & D_1 \end{array} \right], \dots, \left[\begin{array}{c|c} A_N & B_N \\ \hline C_N & D_N \end{array} \right] \right\}, \end{aligned} \quad (16)$$

where ω_i are the 2^r vertices of the polytope given by all combinations of the limit values of the varying parameters

and $\delta_i(\theta)$ is the weighting parameter among the LTI systems, defined by

$$\delta_i(\theta) = \frac{\prod_{j=1}^r |\theta_j - \underline{\mathcal{C}}(\omega_i)_j|}{\prod_{j=1}^r (\bar{\theta}_j - \underline{\theta}_j)}, \quad (17)$$

$$i = 1, \dots, N \text{ where } \delta_i(\theta) > 0, \sum_{i=1}^N \delta_i(\theta) = 1,$$

where $\underline{\mathcal{C}}(\omega_i)_j$ is the j th component of the vector $\underline{\mathcal{C}}(\omega_i)$ given by

$$\underline{\mathcal{C}}(\omega_i)_j = \begin{cases} \theta_j = \bar{\theta}_j & \text{if } (\omega_i)_j = \underline{\theta}_j \\ \theta_j = \underline{\theta}_j & \text{otherwise.} \end{cases} \quad (18)$$

By defining the performance criterion as the minimization of the estimation error of the faulty force ($e = F_{\delta_{\text{model}}} - \hat{F}_\delta(y)$) in terms of an H_∞ problem, the global LPV/ H_∞ observer will be the convex combination of 2^r local observers of the form of (19) by solving the set of LMI problems, whose solution is the extended result from the LTI systems, proposed by [42]

$$L(\theta) : \begin{bmatrix} \dot{x}_o \\ \hat{F}_\delta \end{bmatrix} = \begin{bmatrix} A_o(\theta) & B_o(\theta) \\ C_o(\theta) & D_o(\theta) \end{bmatrix} \begin{bmatrix} x_o \\ y \end{bmatrix}. \quad (19)$$

4. Adaptive Vibration Control System

Once a damper leakage affects the vehicle suspension, the first step is to determine as soon as possible which corner has suffered the lack of force. Afterwards, this fault must be estimated to compute the required compensation force in the healthy dampers.

By using an LPV/ H_∞ observer at each vehicle corner, it is possible to monitor online the behavior of the four MR dampers. If there are no faults on the dampers, $F_{\delta_i} \sim 0$, and consequently all compensations forces $F_{c_j} \sim 0$ for $i \neq j$. However, when a fault occurs in one MR damper, the fault isolation, detection, and estimation are naturally possible because the four LPV observers are decoupled thanks to the vehicle dynamics.

Since F_{δ_i} is not measured but estimated from an LPV observer using (19), this allows the straightforward computation of the compensation forces $F_{c_{j \neq i}}$ according to (7a), (7b), and (7c), such that the full matrix of compensation obtained by the equilibrium of the load distribution when one MR damper fails is given by

$$\begin{bmatrix} F_{c_1} \\ F_{c_2} \\ F_{c_3} \\ F_{c_4} \end{bmatrix} = \begin{bmatrix} 0 & 1 & \frac{t_r}{t_f} & -\frac{t_r}{t_f} \\ 1 & 0 & -\frac{t_r}{t_f} & \frac{t_r}{t_f} \\ \frac{t_f}{t_r} & -\frac{t_f}{t_r} & 0 & 1 \\ -\frac{t_f}{t_r} & \frac{t_f}{t_r} & 1 & 0 \end{bmatrix} \begin{bmatrix} \hat{F}_{\delta_1} \\ \hat{F}_{\delta_2} \\ \hat{F}_{\delta_3} \\ \hat{F}_{\delta_4} \end{bmatrix}. \quad (20)$$

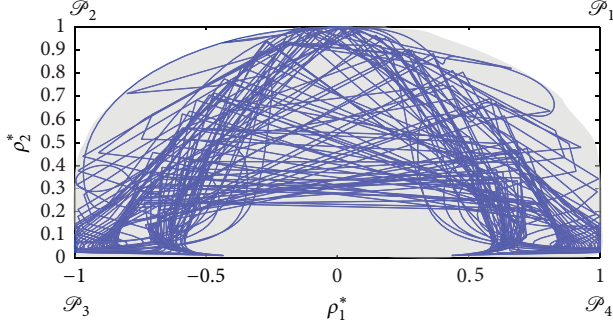


FIGURE 4: Operating region of the scheduling parameters ρ_1^* and ρ_2^* .

For multiple faults, that is, faults in two or three dampers of the vehicle, two aspects must be considered:

- (1) The equilibrium of the load transfer in the chassis, including the simultaneous faults, must be guaranteed using the compensation force matrix of (20).
- (2) Mechanically, the MR damper must be designed with enough damping force (plus the nominal force used in the fault-free case) in order to have faculty to accommodate the lack of damping force of two or more faulty actuators.

4.1. Fault Tolerant Control Based on LPV. The control of the vertical dynamics, adaptive to the damper fault, can be ensured by the LPV control theory to achieve frequency specification performances [44]. Based on [45] that embeds into the control design the constraints of dissipativity and saturation of a semiactive damper with two scheduling parameters, here an LPV/ H_∞ controller is designed at each corner for (a) compensation of lack of damping force of a faulty damper (fault accommodation) and (b) performances of comfort and road holding against road disturbances and uncertainties when a damper leakage occurs.

Scheduling Parameters. Two varying parameters are used in the LPV controller synthesis for each corner: ρ_1^* includes the nonlinearities of the damper and is given by

$$\rho_1^* = \tanh(a_1 \dot{z}_{\text{def}} + a_2 z_{\text{def}}) \cdot \frac{\tanh(I_f / (I_{n0} + I_{c0}))}{I_f / (I_{n0} + I_{c0})} \quad (21)$$

$$\in [-1, 1],$$

where I_{n0} and I_{c0} are the average of electric currents dedicated for the nominal suspension control and compensation. $I_f = I_n + I_c$ is the electric current (controller output) bounded by the saturation constraint:

$$0 \leq I_{\min} < I_f \leq I_{\max} \quad (22)$$

ρ_2^* is used directly to saturate the controller output, given by

$$\rho_2^* = \frac{\tanh(a_1 \dot{z}_{\text{def}} + a_2 z_{\text{def}})}{a_1 \dot{z}_{\text{def}} + a_2 z_{\text{def}}} \cdot (I_{n0} + I_{c0}) \in \left[0, \frac{I_{\max}}{2}\right]. \quad (23)$$

Figure 4 shows the operating region for both scheduling parameters when the QoV model of one corner is subject to a *chirp* road signal with enough frequency content. The operating region of the polytope is similar to a half ellipsoid; note that there are some areas where the varying parameters are not contained (close to the polytopes \mathcal{P}_1 and \mathcal{P}_2), which could be used to reduce the conservatism.

Because the polytopic LPV controller is defined by the scheduling parameters, whose limit values are associated with the minimum and maximum damping force, the transient response of the damper in an online operation is inside of the polytope region such that the response speed of the MR fluid does not affect the frequency specification performances in the controller.

Note that there is a compromise between the control performances and the compensation because $I_{n0} + I_{c0} = I_{\max}/2$; the capability to compensate for a faulty damper is limited by

$$I_c = \begin{cases} I_c = 2 \cdot I_{c0} & \text{if } I(F_c) \geq I_{c_{\max}} \\ 0 < I_c < 2 \cdot I_{c0} & \text{if } I_{c_{\min}} < I(F_c) < I_{c_{\max}} \\ I_c = 0 & \text{if } I(F_c) < I_{c_{\min}}, \end{cases} \quad (24)$$

where $I(F_c) = [F_c \cdot \coth(a_1 \dot{z}_{\text{def}} + a_2 z_{\text{def}})]/f_c$ is the inverse dynamics of the MR damper model, (3) with $\alpha = 1$, which depends on the compensation force, (20), and $I_{c_{\max}} = 2 \cdot I_{c0}$ is the maximum electric current available for compensation. If the faulty damper requires a greater force than the one that could be generated by $I_{c_{\max}}$, the fault will not be well accommodated. In the fault-free case, $I_c = 0$, and the nominal suspension controller works inside the saturation constraint $[I_{n_{\min}}, I_{n_{\max}}]$. Figure 5 shows a scheme to represent the electric current used for the compensation and its interaction with the nominal control actuation.

LPV Modeling Formulation. Following [45], an LPV controller for each healthy MR damper is designed to accommodate the fault of other dampers. The LPV controller is able to handle the nonlinearity of the semiactive damper model and the saturation constraint (represented by the maximum limit of the input electric current I_f). The considered LPV model in this study also is a state-augmented system by adding a low-pass filter to get a proper structure for the LPV controller synthesis [22]. The new LPV QoV model is given by

$$\begin{aligned} \begin{bmatrix} \dot{x} \\ \dot{x}_f \end{bmatrix} &= \underbrace{\begin{bmatrix} A + \rho_2^* B_{I0} C_{I0} & B_1(\rho_1^*) C_f \\ 0_{1 \times 4} & A_f \end{bmatrix}}_{A_s(\rho_1^*, \rho_2^*)} \begin{bmatrix} x \\ x_f \end{bmatrix} \\ &+ \underbrace{\begin{bmatrix} B_2 \\ 0 \end{bmatrix}}_{B_{s1}} z_r + \underbrace{\begin{bmatrix} 0_{4 \times 1} \\ B_f \end{bmatrix}}_{B_{s2}} u_c, \\ y &= \underbrace{\begin{bmatrix} C & 0_{2 \times 1} \end{bmatrix}}_{C_s} \begin{bmatrix} x \\ x_f \end{bmatrix} \end{aligned} \quad (25)$$

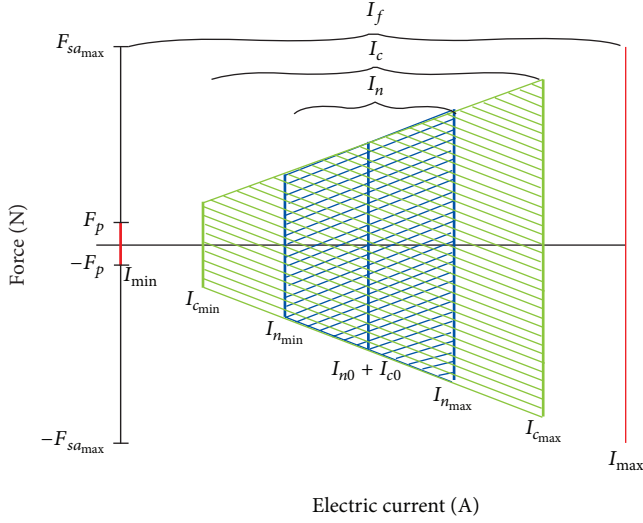


FIGURE 5: Force-electric current diagram in a healthy MR damper used for the adaptive control.

with

$$B_{I0} = \begin{bmatrix} -\frac{I_{n0} + I_{c0}}{m_s} & 0 & \frac{I_{n0} + I_{c0}}{m_s} & 0 \end{bmatrix}^T, \quad (26)$$

$$C_{I0} = [a_1 \ a_2 \ -a_1 \ -a_2],$$

where B_1 is the column matrix of B associated with I and B_2 is the column matrix of B associated with the road profile z_r in (4). Note that the matrix A does not depend on α because the compensation purpose is based on healthy dampers.

LPV/ H_∞ Control Design. The extension to the method in [45] lies into the parameter ρ_2^* that incorporates the damping force used to compensate the faulty damper. The control design satisfies the actuator constraints. Indeed, depending on the value of the fault, the semiactive suspension is adapted to meet the required robust performances in comfort and road holding, according to the following frequency specifications:

$$W_r = \frac{K_r \omega_r s}{s + \omega_r} \quad \text{to add robustness to road disturbances,}$$

$$W_{\dot{z}_s} = \frac{K_s (s^2 + 2\zeta_{1s} \omega_{1s} s + \omega_{1s}^2)}{s^2 + 2\zeta_{2s} \omega_{2s} s + \omega_{2s}^2} \quad (27)$$

to reduce the vertical acceleration of m_s in its natural frequency,

$$W_{z_{us}} = \frac{K_{us} (s^2 + 2\zeta_{1us} \omega_{1us} s + \omega_{1us}^2)}{s^2 + 2\zeta_{2us} \omega_{2us} s + \omega_{2us}^2}$$

to reduce the vertical displacement of m_{us} at high frequencies,

where $W_{\dot{z}_s}$ is a high-pass filter with cut-off frequency greater than the natural frequency of the sprung mass, $W_{z_{us}}$ is a low-pass filter with cut-off frequency lower than the natural frequency of the unsprung mass, and W_r can be a first-order filter to shape the road disturbances or a band pass filter to increase the sensitivity in a frequency band of interest.

Taking into account the control specifications, the generalized system $\Sigma(\rho_1^*, \rho_2^*)$ used for the LPV control synthesis is given by

$$\begin{aligned} \Sigma(\rho_1^*, \rho_2^*) &:= \begin{bmatrix} \dot{\xi} \\ z_\infty \\ y \end{bmatrix} \\ &= \begin{bmatrix} \mathcal{A}(\rho_1^*, \rho_2^*) & \mathcal{B}_1 & \mathcal{B}_2 \\ \mathcal{C}_\infty & \mathbf{0} & \mathbf{0} \\ \mathcal{C} & \mathbf{0} & \mathbf{0} \end{bmatrix} \begin{bmatrix} \xi \\ w \\ u_c \end{bmatrix} \end{aligned} \quad (28)$$

with

$$\begin{aligned} \mathcal{A}(\rho_1^*, \rho_2^*) &= \begin{bmatrix} A_s(\rho_1^*, \rho_2^*) & \mathbf{0} \\ \mathbf{0} & A_w \end{bmatrix}, \\ \mathcal{B}_1 &= \begin{bmatrix} B_{s1} W_{z_r} \\ \mathbf{0} \end{bmatrix}, \end{aligned} \quad (29)$$

$$\mathcal{B}_2 = \begin{bmatrix} B_{s2} \\ \mathbf{0} \end{bmatrix},$$

$$\mathcal{C} = [C \ \mathbf{0}],$$

where $\xi = [x_s \ x_w]^T$ such that x_s are the states in the vertical dynamics of the augmented QoV model of (25) and x_w are the vertical weighting functions states with dynamics A_w , $z_\infty = [z_1 \ z_2]^T$ is the controlled output with dynamics \mathcal{C}_∞ , $y = [z_{\text{def}} \ \dot{z}_{\text{def}}]^T$ is the measured output with dynamics C that represents the state feedback, and $u_c = u^{H_\infty}$ is the controller output.

Problem Solution. The LPV/ H_∞ controller is synthesized in the LMI framework for polytopic systems according to [42]; all varying parameters are bounded in $\rho_1^* \in [-1, 1]$ and $\rho_2^* \in [0, I_{\text{max}}/2]$ with $I_{\text{max}} = 6$ A. The resulting global LPV/ H_∞ controller is a convex combination of the local controllers obtained by solving the set of LMIs only on each vertex of the polytope formed by the limit values of the varying parameters. Since 2 varying parameters are used, each QoV considers a polytope of 4 vertices; that is, 4 local LTI controllers are obtained, such that

$$\begin{aligned} K(\rho) &: \begin{bmatrix} A_c(\rho) & B_c(\rho) \\ C_c(\rho) & D_c(\rho) \end{bmatrix} \\ &= \sum_{i=1}^2 \xi_i(\rho) K_i = \sum_{i=1}^2 \xi_i(\rho) \begin{bmatrix} A_{c_i} & B_{c_i} \\ C_{c_i} & D_{c_i} \end{bmatrix}. \end{aligned} \quad (30)$$

The controller stability is guaranteed for all trajectories of the varying parameters, even if an extra compensation force is demanded, by solving the LMI problem at each vertex expressed by the *Bounded Real Lemma* [42, 46] as

$$\begin{bmatrix} \mathcal{A}(\rho)^T K(\rho) + K(\rho) \mathcal{A}(\rho) & K(\rho) \mathcal{B} & \mathcal{C}_\infty^T \\ \mathcal{B}^T K(\rho) & -\gamma_\infty^2 I & \mathbf{0} \\ \mathcal{C}_\infty & \mathbf{0} & -I \end{bmatrix} < 0. \quad (31)$$

5. Simulation Results

The evaluation of the proposed AVCS for MR damper faults has been separated into two sections: (a) firstly, the performance of the fault observer is analyzed using different simulation tests, and then it is compared with respect to a parameter estimation method considering noise on the measurements; (b) secondly, the fault tolerant controller is evaluated when one damper fails and the other three MR dampers are used for the fault compensation.

5.1. Estimation of MR Damper Faults. To evaluate the performance of the LPV/ H_∞ observer, the front-left corner of a medium payload pickup truck has been used as test-bed, Figure 2, whose experimental parameters obtained by a test of kinematics and compliance are $m_s = 630$ Kg, $m_{us} = 81.5$ Kg, $k_s = 43,500$ N/m, and $k_t = 230,000$ N/m.

Experimental data obtained from a commercial MR damper are used to model the nonlinearities of this actuator by considering $\alpha = 1$ in (3), according to the methodology of characterization of MR dampers in [34]. De-J Lozoya-Santos et al. [34] present a discussion about the required experimentation to characterize MR dampers exclusively to describe the physical phenomena, or according to a target application (control design purposes, study of the vehicle dynamics, mechanical configuration, etc.). In this study, the used experiments were chosen to describe the different physical MR phenomena of the shock absorber (stiffness, nonlinear viscous damping, friction, and saturation) in the full range of frequencies of interest with common rod displacements in a car. The *Design of Experiments* (DoE) used to characterize the hysteresis loops and nonlinear transient response of the MR damping force includes different sequences of displacement (suspension deflection) and electric current (manipulation variable) in a composite design.

The commercial MR damper used to perform different experimental tests of identification was manufactured by *Delphi MagneRide* for SUVs. The range of force is $\pm 8,000$ N (peak to peak); the stroke is around 40 mm with a time constant of 14 ms and settling time of 84 ms. This shock absorber has continuous actuation (from 0 to 6 A) and considerable hysteresis at high frequencies with high deflections. Figure 6(a) shows the FV curve of the MR damper using an experiment with excitation of displacement up to 15 Hz at different I values; note that the yield stress of the MR fluid reaches the saturation of 8,000 N when $I = 6$ A and the frequency of motion is 15 Hz.

Figure 6(b) shows the performance of the MR damper model used in the simulations, (3), whose parameters were obtained from a standard ISO road profile type D: $f_c = 600.9$, $a_1 = 37.8$, $a_2 = 22.1$, $b_1 = 2,830.8$, and $b_2 = -7,897.2$.

In the simulation tests to evaluate the FDI module based on the LPV observer, the road profile is composed of a *chirp* signal from 0 to 8 Hz. *Gaussian* noise is assumed in the z_{def} and \dot{z}_{def} measurements. Two fault scenarios have been studied:

- (i) An abrupt damper leakage from $t = 5$ to 10 s with 20% of lack of force ($\alpha = 0.8$) and from $t = 13$ to 18 s

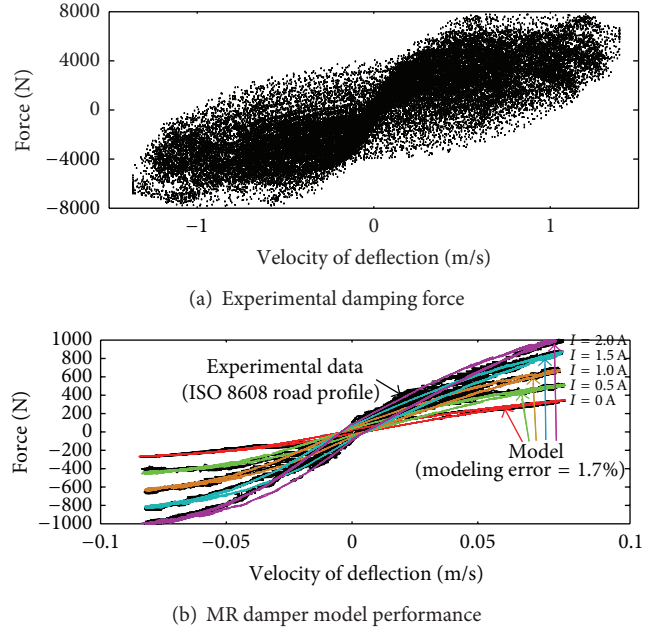


FIGURE 6: (a) Experimental data of the commercial MR damper when the damper rod is excited by a *chirp* signal from 0.5 to 15 Hz at different stepped values of electric current from 0 to 6 A. (b) MR damper modeling for different I values, when $\alpha = 1$.

with 50% of lack of force ($\alpha = 0.5$): during whole test, the electric current on the MR damper is constant, $I = 1$ A. This test studies the property of the LPV observer to schedule the fault estimation according to the α value.

- (ii) A gradual damper leakage from 0% of lack of force ($\alpha = 1$) at $t = 5$ s until 50% of lack of force ($\alpha = 0.5$) at $t = 20$ s: in this test, the electric current is a random signal from 0 to 2.5 A that mimics a controller output on the MR damper. This test studies the transient response of the fault estimation and its insensitivity to the manipulation variable.

The robust fault estimation of the LPV observer was compared with respect to a static fault estimation using (3), which depends on the reliability of the model parameters and it can be affected by the noise in the measurements of z_{def} and \dot{z}_{def} .

Figure 7 shows the performance of the LPV/ H_∞ observer in both tests. Note that the transient response of the fault estimation with the LPV observer is robust to the noise of measurements; however, the static estimation is noisy at all frequencies even when the damper is free of faults. Indeed, the fault estimation with the static equation has more amplitude than the correct one, as the frequency increases.

Because the transient response of the LPV observer represents correctly the implemented fault in both tests, the proposed observer can estimate abrupt or gradual damper leakages of any magnitude for all trajectories bounded by α that belong to a convex LMI solution. Also, Figure 7 illustrates that the LPV/ H_∞ observer is robust to road

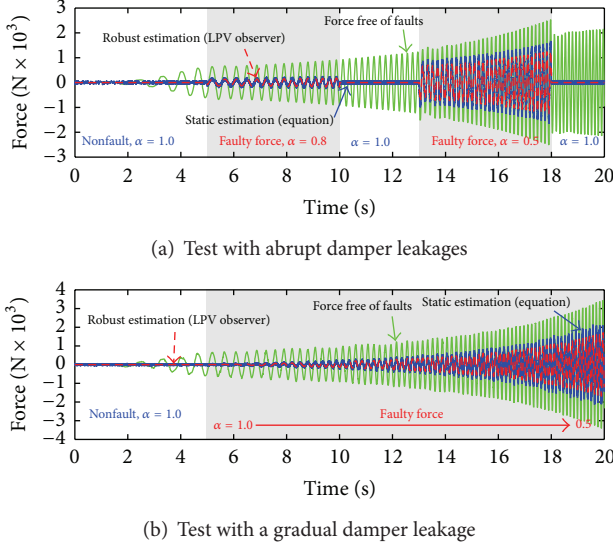


FIGURE 7: Fault estimation performance with the LPV/ H_∞ observer.

disturbances (road profile at different sinusoidal frequencies and amplitudes), and the fault estimation is insensitive to the value of electric current on the MR damper; that is, a closed-loop implementation does not affect the FDI performance. Indeed, I is only a gain in the semiactive force, such that

$$F_\delta = F_{MR}(I) - \alpha F_{MR}(I), \quad (32)$$

where both terms in right side are dependent on I and its difference has only dependence on α .

A correct estimation of F_δ in the FDI module avoids unrealistic control reconfigurations or fault accommodations for fault tolerant control purposes. For instance, the static estimation of the fault in Figure 7 overshoots around 800 N from the real fault in some frequencies; this incorrect fault information will demand more damping force of compensation than the required one by the actuator or by external actuators (other healthy dampers in the vehicle) to reduce the fault effect.

5.2. Control Adaptation for MR Damper Faults. When an oil leakage occurs in one of the dampers and the car is moving, the lack of damping force increases the vertical vehicle body motion. To reduce the fault propagation into the vertical dynamics, the obtained FDI information is used by the AVCS to compensate for the faulty damper and thus maintain the comfort in the vehicle.

Figure 8 schematizes the proposed AVCS, in particular the interaction between the FDI module and the LPV controller. Once a damper leakage is detected and estimated, the load distribution analysis determines the compensation force that the healthy dampers must deliver. Finally, at each corner, the LPV based controller is adapted to accommodate the fault through F_c , fulfilling the MR damper constraints (semiactiveness and saturation).

A vehicle *CarSim* model was used to evaluate the proposed AVCS; the suspension model was characterized from

real data curves (camber angles, caster angles, damping force, jounce/rebound stops, spring, tire stiffness, etc.), structural parameters (mechanical ratios, compliance coefficients, Kingpin geometry, etc.), and physical dimensions (weight, length, width, height, wheel base, front and rear track, and so on) obtained by a *K&C* test on a commercial pickup truck of medium payload. Figure 9 illustrates some of the physical parameters used in the vehicle model characterization in *CarSim*; more parameters and data curves used in the vehicle customization are in [33].

In *CarSim*, the model was customized as a generic full-size load vehicle model, which is used as *Software-in-the-Loop* (SiL) in a *Matlab/Simulink* environment. The customization of the suspension system considers independent wheel stations at the front side and a rear solid axle at the back. Since *CarSim* is well accepted in the automotive control community (research and manufacturing), the customized model is a very useful tool to analyze the vehicle dynamics and evaluate the performance of the proposed control prototype.

Two simulation tests have been used to evaluate the performance of the AVCS. In both tests, an oil leakage with $\alpha = 0.5$ at $t = 0$ has been implemented in the MR damper of the front-left corner of the vehicle.

Test #1, Two Bumps in Series. The vehicle is driven straightforwardly at constant speed of $v_x = 30$ Km/h. The road profile is composed of two bumps in series of 5 cm height, Figure 10(a). This test allows studying the AVCS performance when the vehicle is driven over abrupt (sudden) road disturbances.

Figure 11 shows the performance of the proposed AVCS versus an *uncontrolled suspension* (US), considered as a passive system, and versus a controlled suspension that does not include the adaptation strategy to the fault (LPV *nominal control*, LPV NC); SFF (*Suspension Free of Faults*) refers to the simulation of the LPV/ H_∞ suspension control when no fault is considered. By using the *Root Mean Square* (RMS) value of the pitch rate ($\dot{\phi}$), sprung mass acceleration (\ddot{z}_{s_c}), and heave (z_{s_c}) motion of the vehicle as comfort performance indexes, normalized with respect to the uncontrolled suspension, the proposed AVCS improves $\dot{\phi}$ 28%, \ddot{z}_{s_c} 17%, and z_{s_c} 9%. Note that the LPV nominal control has better comfort performance than US; however, the AVCS improves the comfort up to 10% when a damper fault occurs in comparison to the LPV NC.

Test #2, Bounce Sine Sweep (BSS) Test. Chirp road sequence with decreasing road elevation (10 to 1 cm) and span of frequency (0.5 to 10 Hz): the vehicle velocity is 30 Km/h, Figure 10(b). This test allows the excitation of the automobile suspension system in the frequency band of interest for ride comfort. The test allows the monitoring of the vehicle behavior at each particular frequency in contrast to a random standard road profile (ISO 8608).

Figure 12 illustrates the pitch angle and the chassis vertical acceleration as performance indexes of comfort. In both signals, the AVCS has better comfort performance than the LPV NC: improvement of 24% in the pitch angle and 10% in the chassis vertical acceleration according to the RMS index. With respect to the US, the AVCS increases

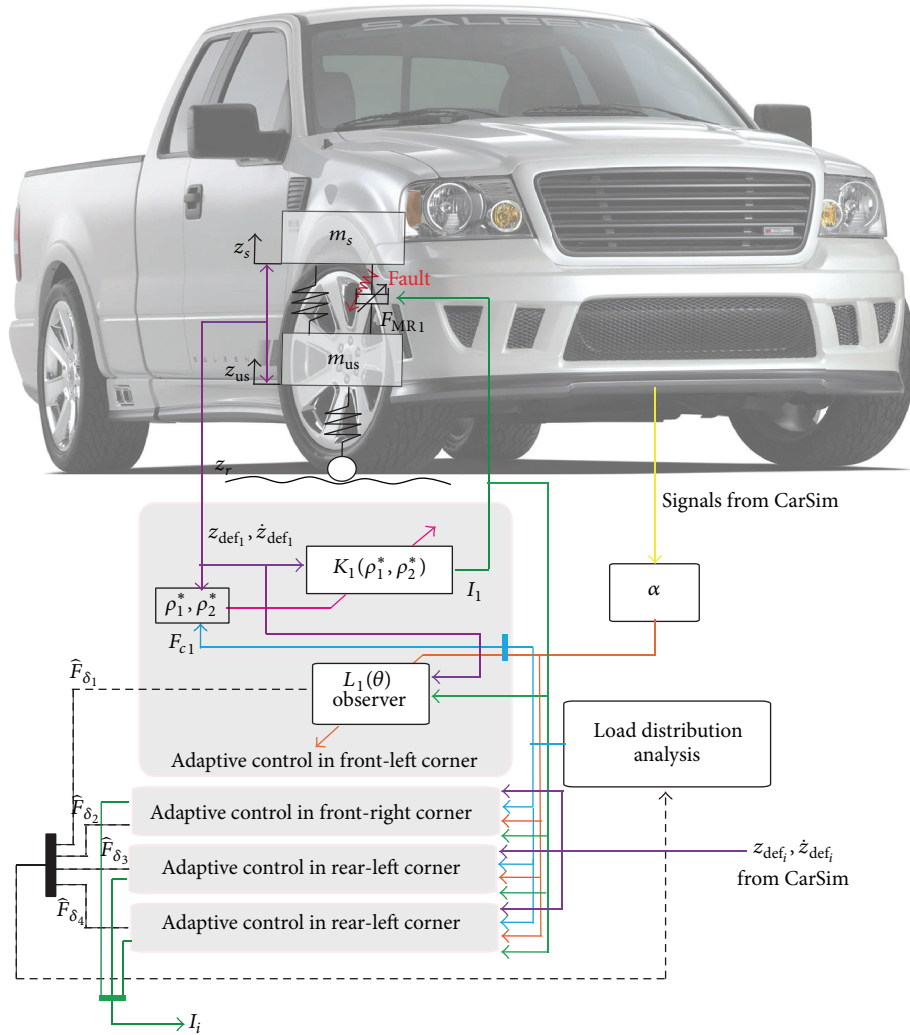


FIGURE 8: Adaptive suspension control system for MR damper faults.

the passenger comfort up to 64%. Indeed in both signals, the AVCS presents similar comfort performance than the SFF case; see bar graphs in Figure 12. Qualitatively, the US has the worst comfort performance below the 15 s (from 0.5 to 5 Hz), that is, around the first frequency of resonance of the chassis. Figure 12(b) shows that the main differences between AVCS and the nominal control are in the resonance frequencies; that is, the AVCS seeks to keep, as much as possible, the same vibrations like the SFF system, mainly in the natural frequencies of the suspension system.

Figure 13(a) shows how the MR damping force increases in a healthy damper, for example, at the front-right actuator, to compensate for the missing force of the faulty damper. The semiactiveness constraint of the MR damper is then ensured with the proposed AVCS. Figure 13(b) shows that the nominal LPV controller, whose performance is good when the suspension is free of faults, operates between 0 and 2 A without the compensation; when the compensation is used, the LPV controller utilizes the full range of actuation to generate more damping force and satisfies the saturation constraint of the MR damper.

Remark 2. The most important restriction to implement the proposed AVCS approach is the extra damping force available to compensate the lack of force caused by oil leakages. Mechanically, the semiactive damper must be designed with enough damping force (plus the nominal force used in the fault-free case) in order to have faculty to accommodate the lack of force of other faulty actuators.

In an implementation, the fault estimation and its compensation depend on the sample frequency. Usually, the most important bandwidth of control in automotive suspensions is from 0 to 25 Hz, such that the microcontroller must use at least 100 Hz as sample frequency. Although at high car velocities the frequency of motion is greater than 20 Hz, at these frequencies the vehicle body filters the road disturbances such that there is no difference in the vertical vehicle dynamics when a damper is faulty. Indeed, the fault estimation is frequency dependent such that the best frequency to estimate this malfunction is around the resonance frequency of the sprung mass [47].

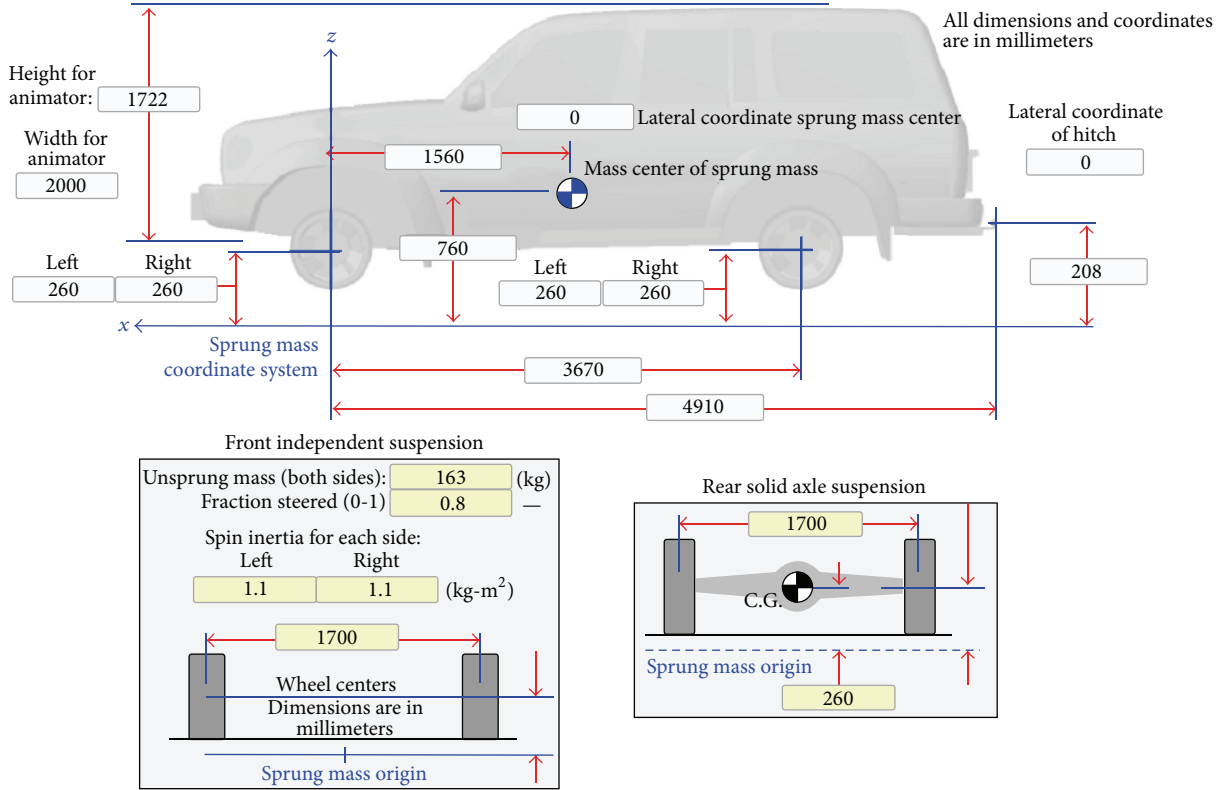


FIGURE 9: Parameters for the pickup vehicle model in *CarSim*.



FIGURE 10: Simulation tests in *CarSim* used in the evaluation of the AVCS.

6. Conclusions

Based on a full vehicle suspension model, a new *Adaptive Vibration Control System (AVCS)* based on the *Linear Parameter-Varying (LPV)* control theory has been presented for a *magnetorheological (MR)* damper leakage. The main idea is to use the damping force of the remaining three healthy shock absorbers to avoid the fault propagation into the vertical dynamics of the vehicle; the control algorithm is two levels. Firstly the faulty *Quarter of Vehicle (QoV)* is isolated and the lack of force is estimated. Secondly, the load distribution analysis determines the compensation force that each healthy MR damper must add to reduce the effect of the lack of force of the faulty damper. This AVCS is based on the LPV framework to include the semiactiveness and saturation constraints of an MR damper into the controller design.

Inspired on the H_∞ control problem, an LPV robust observer is proposed to estimate the missed force caused by an MR damper leakage; the polytopic LPV approach is used to solve a finite number of linear matrix inequalities where the leakage degree is a varying parameter, together with another varying parameter used to represent the MR nonlinearities. Simulation results show that this fault observer has good performance, with robustness to noisy measurements and road disturbances, in contrast with a static equation used to model the damping force obtained from the least squares estimation algorithm. The estimation error of the fault was decreased up to 20% in some frequencies using the fault observer. Indeed, the LPV observer can diagnose and estimate the faulty force caused by an abrupt or gradual damper leakage without considering the degree of the oil leakage.

Because the proposed *Fault Detection and Isolation (FDI)* system is based on a QoV model, four LPV robust observers

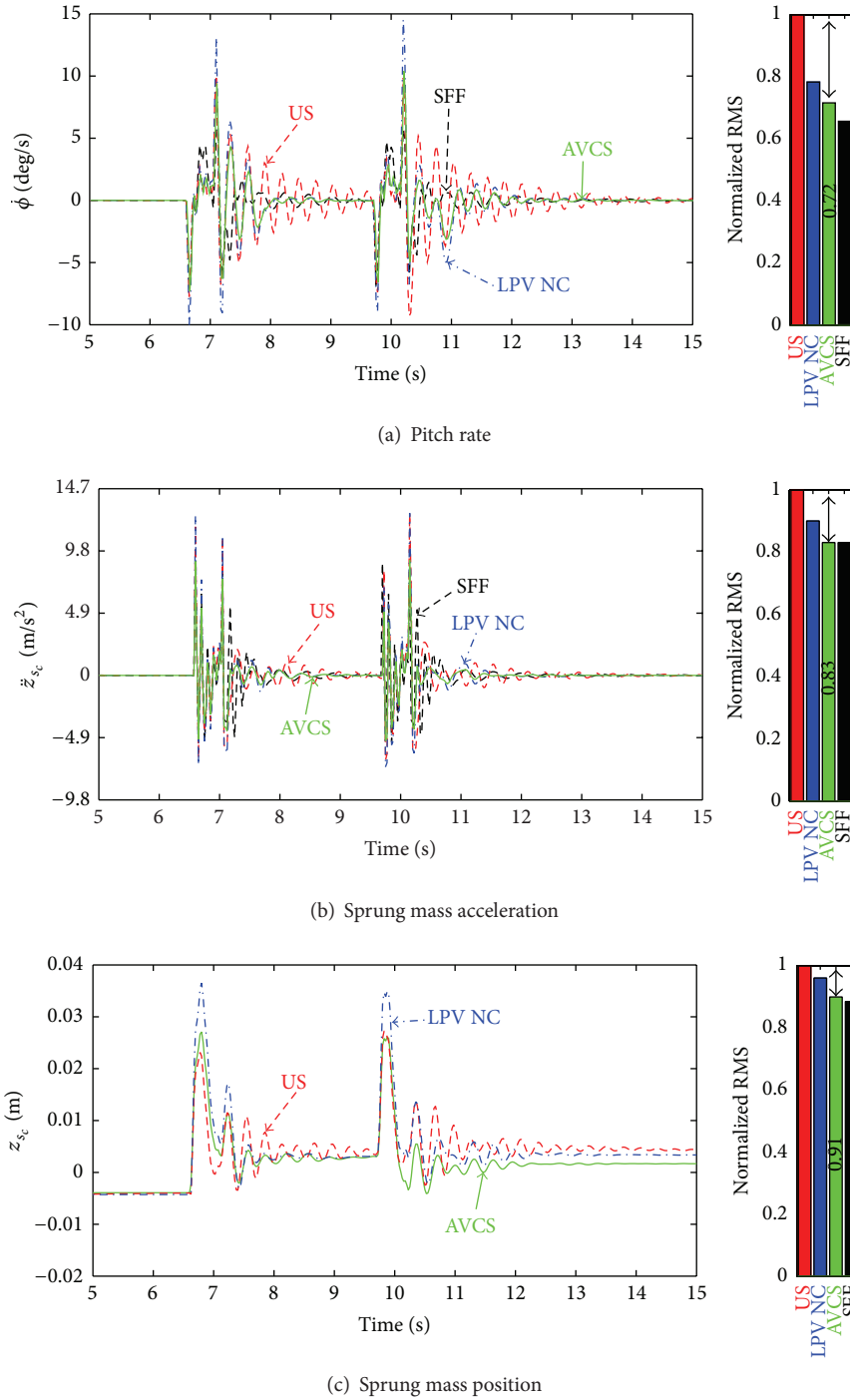


FIGURE 11: Performance of the AVCS and comparison with other suspension systems in test #1, by using a normalized RMS with respect to the uncontrolled suspension.

can be used to develop a global FDI strategy with independent corners. When a fault occurs in one vehicle corner, the associated observer estimates the lack of force caused by the damper leakage, which is used to compute the compensation forces that the healthy dampers must add. Simulation results in

CarSim, used as Software-in-the-Loop, show that when an oil leakage in the front-left MR damper is present the proposed AVCS improves the comfort up to 24% and 64% with respect to a nominal controlled (without fault compensation) and uncontrolled suspension system, respectively.

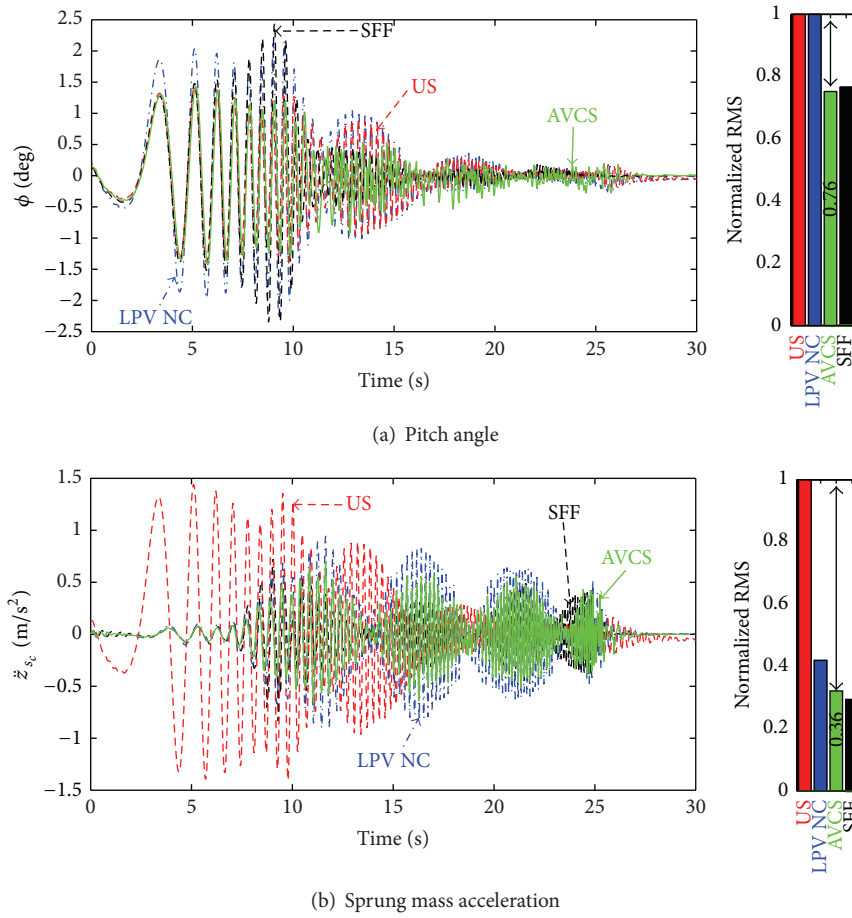


FIGURE 12: Performance of the AVCS and comparison with other suspension systems in test #2, by using a normalized RMS with respect to the uncontrolled suspension.

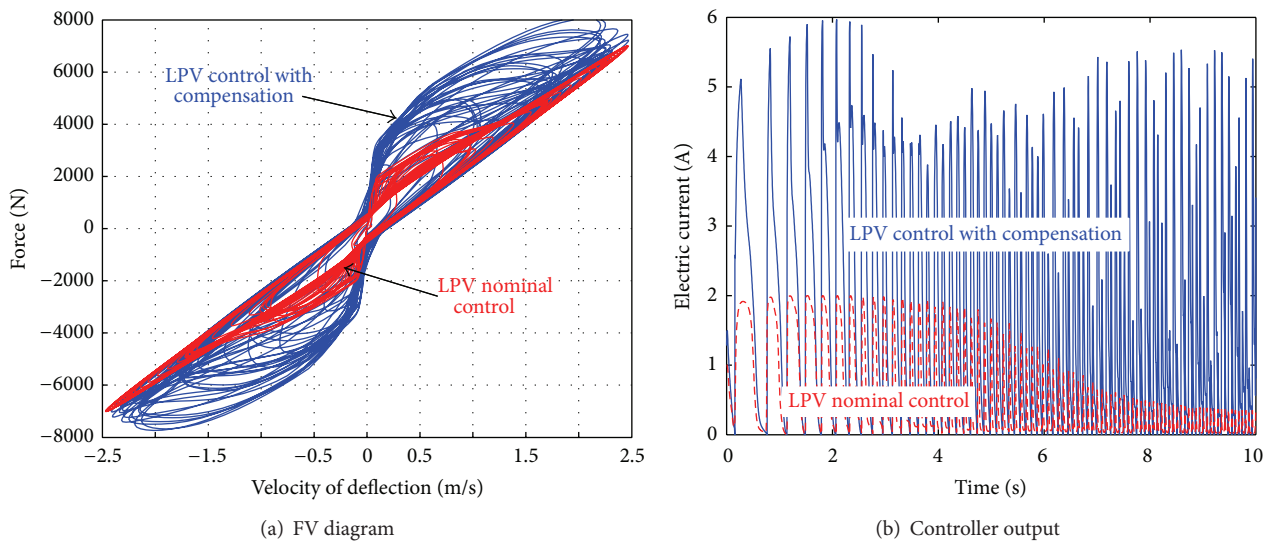


FIGURE 13: (a) Semiactive damping force in the front-right corner with and without fault compensation and (b) the corresponding controller output.

Abbreviations

α :	Ratio of the faulty force and the nominal force
ζ_i :	Damping factor of a second order filter (weighting function)
$\theta, \dot{\theta}$, and $\ddot{\theta}$:	Roll angle, roll rate, and roll acceleration (rad, rad/s, and rad/s ²)
ρ_1 :	Nonlinear part of the damper model
$\phi, \dot{\phi}$, and $\ddot{\phi}$:	Pitch angle, pitch rate, and pitch acceleration (rad, rad/s, and rad/s ²)
$\Sigma(\theta)$:	Generalized LPV plant in an H_∞ control problem
ω_i :	Cut-frequency of the filter (weighting function) (rad/s)
a_1, a_2 :	Preyield viscous damping coefficients of Guo model (s/m, 1/m)
b_1 :	Viscous damping coefficient of Guo model (Ns/m)
b_2 :	Stiffness coefficient of Guo model (N/m)
e :	Estimation error of the fault (N)
f_c :	Dynamic yield force of Guo model (N)
F_δ :	Loss of force (N)
F_{MR} :	Force of an MR (healthy) damper (N)
\bar{F}_{MR} :	Force of a faulty MR damper (N)
I :	Control effort of an MR damper (electric current) (A)
I_{xx}, I_{yy} :	Roll and pitch inertia (Kg-m ²)
$K(\rho)$:	LPV controller
k_s :	Spring stiffness in a QoV (N/m)
k_t :	Tire stiffness in a QoV (N/m)
$L(\theta)$:	LPV fault observer
l_f :	Distance from center of gravity (CoG) to front track (m)
l_r :	Distance from CoG to rear track (m)
m_s :	Sprung mass in a QoV (Kg)
m_{s_c} :	Total sprung mass (chassis mass) (Kg)
m_{us} :	Unsprung mass in a QoV (Kg)
t_f :	Distance from CoG to front-left tire (m)
t_r :	Distance from CoG to rear-left tire (m)
v_x :	Longitudinal vehicle velocity (m/s, Km/h)
W_i :	Weighting function
z_{def}, \dot{z}_{def} :	Displacement and velocity of the damper piston in a QoV (m, m/s)
z_{∞} :	Controlled variables in an H_∞ control problem
z_r :	Road profile (m)
z_s, \dot{z}_s , and \ddot{z}_s :	Sprung mass displacement, velocity, and acceleration in a QoV (m, m/s, and m/s ²)
z_{s_c}, \dot{z}_{s_c} , and \ddot{z}_{s_c} :	Chassis displacement, velocity, and acceleration in the CoG (m, m/s, and m/s ²)
z_{us}, \dot{z}_{us} , and \ddot{z}_{us} :	Unsprung mass displacement, velocity, and acceleration in a QoV (m, m/s, and m/s ²).

Conflict of Interests

The authors declare that there is no conflict of interests regarding the publication of this paper.

Acknowledgments

The authors thank CONACyT (PCP Project 03/2010) for its partial support. Also, the authors thank Dr. Jorge de Jesu's Lozoya-Santos for sharing his experience and knowledge to improve this paper along with some discussions; they thank him for his time.

References

- [1] J. Dixon, *The Shock Absorber Handbook*, Wiley, 2nd edition, 2007.
- [2] B. T. Fijalkowski, *Automotive Mechatronics: Operational and Practical Issues*, vol. 2, Springer, 2011.
- [3] J. Lozoya-Santos, *Control of automotive semiactive suspensions [Ph.D. thesis]*, Tecnológico de Monterrey, Campus Monterrey, 2013, chapter. 2–4.
- [4] T. Gillespie, *Fundamentals of Vehicle Dynamics*, chapter 5, Society of Automotive Engineers, 1992.
- [5] R. Stanway, J. L. Sproston, and N. G. Stevens, "Non-linear modelling of an electro-rheological vibration damper," *Journal of Electrostatics*, vol. 20, no. 2, pp. 167–184, 1987.
- [6] D. R. Gamota and F. E. Filisko, "Dynamic mechanical studies of electrorheological materials: moderate frequencies," *Journal of Rheology*, vol. 35, no. 3, pp. 399–425, 1991.
- [7] B. F. Spencer Jr., S. J. Dyke, M. K. Sain, and J. D. Carlson, "Phenomenological model for magnetorheological dampers," *ASCE Journal of Engineering Mechanics*, vol. 123, no. 3, pp. 230–238, 1997.
- [8] N. M. Wereley, L. Pang, and G. M. Kamath, "Idealized hysteresis modeling of electrorheological and magnetorheological dampers," *Journal of Intelligent Material Systems and Structures*, vol. 9, no. 8, pp. 642–649, 1998.
- [9] G. Yang, B. F. Spencer Jr., J. D. Carlson, and M. K. Sain, "Large-scale MR fluid dampers: modeling and dynamic performance considerations," *Engineering Structures*, vol. 24, no. 3, pp. 309–323, 2002.
- [10] S.-B. Choi and S.-S. Han, " H_∞ control of electrorheological suspension system subjected to parameter uncertainties," *Mechatronics*, vol. 13, no. 7, pp. 639–657, 2003.
- [11] D. Guo and H. Hu, "Nonlinear stiffness of a magnetorheological damper," *Nonlinear Dynamics*, vol. 40, no. 3, pp. 241–249, 2005.
- [12] L. X. Wang and H. Kamath, "Modelling hysteretic behaviour in magnetorheological fluids and dampers using phase-transition theory," *Smart Materials and Structures*, vol. 15, no. 6, pp. 1725–1733, 2006.
- [13] S. Guo, S. Yang, and C. Pan, "Dynamical modeling of magnetorheological damper behaviors," *Journal of Intelligent Material Systems and Structures*, vol. 17, pp. 3–14, 2006.
- [14] N. M. Kwok, Q. P. Ha, T. H. Nguyen, J. Li, and B. Samali, "A novel hysteretic model for magnetorheological fluid dampers and parameter identification using particle swarm optimization," *Sensors and Actuators A: Physical*, vol. 132, no. 2, pp. 441–451, 2006.

- [15] Ş. Çeşmeci and T. Engin, "Modeling and testing of a field-controllable magnetorheological fluid damper," *International Journal of Mechanical Sciences*, vol. 52, no. 8, pp. 1036–1046, 2010.
- [16] V. S. Atray and P. N. Roschke, "Design, fabrication, testing, and fuzzy modeling of a large magnetorheological damper for vibration control in a railcar," in *Proceedings of the IEEE/ASME Joint Rail Conference*, pp. 223–229, Chicago, Ill, USA, April 2003.
- [17] K. K. Ahn, M. A. Islam, and D. Q. Truong, "Hysteresis modeling of magneto-rheological (MR) fluid damper by self tuning fuzzy control," in *Proceedings of the International Conference on Control, Automation and Systems (ICCAS '08)*, pp. 2628–2633, October 2008.
- [18] A. C. Shivaram and K. V. Gangadharan, "Statistical modeling of a magneto-rheological fluid damper using the design of experiments approach," *Smart Materials and Structures*, vol. 16, no. 4, pp. 1310–1314, 2007.
- [19] S.-B. Choi, S.-K. Lee, and Y.-P. Park, "A hysteresis model for the field-dependent damping force of a magnetorheological damper," *Journal of Sound and Vibration*, vol. 245, no. 2, pp. 375–383, 2001.
- [20] K.-S. Hong, H.-C. Sohn, and J. K. Hedrick, "Modified skyhook control of semi-active suspensions: a new model, gain scheduling, and hardware-in-the-loop tuning," *Journal of Dynamic Systems, Measurement and Control*, vol. 124, no. 1, pp. 158–167, 2002.
- [21] H. Du, K. Y. Sze, and J. Lam, "Semi-active H_{∞} control of vehicle suspension with magneto-rheological dampers," *Journal of Sound and Vibration*, vol. 283, no. 3–5, pp. 981–996, 2005.
- [22] C. Poussot-Vassal, O. Sename, L. Dugard, P. Gáspár, Z. Szabó, and J. Bokor, "A new semi-active suspension control strategy through LPV technique," *Control Engineering Practice*, vol. 16, no. 12, pp. 1519–1534, 2008.
- [23] C.-C. Chang and L. Zhou, "Neural network emulation of inverse dynamics for a magnetorheological damper," *Journal of Structural Engineering*, vol. 128, no. 2, pp. 231–239, 2002.
- [24] S. M. Savaresi, S. Bittanti, and M. Montiglio, "Identification of semi-physical and black-box non-linear models: the case of MR-dampers for vehicles control," *Automatica*, vol. 41, no. 1, pp. 113–127, 2005.
- [25] H. Du, J. Lam, and N. Zhang, "Modelling of a magneto-rheological damper by evolving radial basis function networks," *Engineering Applications of Artificial Intelligence*, vol. 19, no. 8, pp. 869–881, 2006.
- [26] M. Zapateiro, N. Luo, H. R. Karimi, and J. Vehí, "Vibration control of a class of semiactive suspension system using neural network and backstepping techniques," *Mechanical Systems and Signal Processing*, vol. 23, no. 6, pp. 1946–1953, 2009.
- [27] H. Metered, P. Bonello, and S. O. Oyadiji, "The experimental identification of magnetorheological dampers and evaluation of their controllers," *Mechanical Systems and Signal Processing*, vol. 24, no. 4, pp. 976–994, 2010.
- [28] M. J. L. Boada, J. A. Calvo, B. L. Boada, and V. Díaz, "Modeling of a magnetorheological damper by recursive lazy learning," *International Journal of Non-Linear Mechanics*, vol. 46, no. 3, pp. 479–485, 2011.
- [29] J. C. Tudón-Martínez, J. J. Lozoya-Santos, R. Morales-Menendez, and R. A. Ramirez-Mendoza, "An experimental artificial neural-network-based modeling of magneto-rheological fluid dampers," *Smart Materials and Structures*, vol. 21, no. 8, Article ID 085007, pp. 1–16, 2012.
- [30] Sachs, "Shock absorbers leak, potential causes," Tech. Rep., Sachs, 2008.
- [31] S. Fergani, O. Sename, and L. Dugard, "A LPV/ \mathcal{H}_{∞} fault tolerant control of vehicle roll dynamics under semi-active damper malfunction," in *Proceedings of the American Control Conference (ACC '14)*, pp. 4482–4487, IEEE, Portland, Ore, USA, June 2014.
- [32] J. C. Tudón-Martínez, S. Varrier, O. Sename, R. Morales-Menendez, J.-J. Martínez, and L. Dugard, "Fault tolerant strategy for semi-active suspensions with LPV accommodation?" in *Proceedings of the 2nd International Conference on Control and Fault-Tolerant Systems (SysTol '13)*, pp. 631–636, Nice, France, October 2013.
- [33] J. Tudón-Martínez, *Fault tolerant control in automotive semi-active suspensions [Ph.D. thesis]*, Tecnológico de Monterrey, Campus Monterrey, Monterrey, Mexico, 2014.
- [34] J. De-J Lozoya-Santos, R. Morales-Menendez, R. Ramirez-Mendoza, J. C. Tudón-Martínez, O. Sename, and L. Dugard, "Magneto-rheological damper—an experimental study," *Journal of Intelligent Material Systems and Structures*, vol. 23, no. 11, pp. 1213–1232, 2012.
- [35] A. Yetendje, M. Seron, and J. De Doná, "Diagnosis and actuator fault tolerant control in vehicle active suspension," in *Proceedings of the 3rd International Conference on Information and Automation for Sustainability (ICIAFS '07)*, pp. 153–158, Melbourne, Australia, December 2007.
- [36] A. Chamseddine and H. Noura, "Control and sensor fault tolerance of vehicle active suspension," *IEEE Transactions on Control Systems Technology*, vol. 16, no. 3, pp. 416–433, 2008.
- [37] P. Gáspár, Z. Szabó, and J. Bokor, "LPV design of fault-tolerant control for road vehicles," in *Proceedings of the 1st Conference on Control and Fault-Tolerant Systems (SysTol '10)*, pp. 807–812, Nice, France, October 2010.
- [38] D. Fischer and R. Isermann, "Mechatronic semi-active and active vehicle suspensions," *Control Engineering Practice*, vol. 12, no. 11, pp. 1353–1367, 2004.
- [39] J. Kim and H. Lee, "Sensor fault detection and isolation algorithm for a continuous damping control system," *Journal of Automobile Engineering*, vol. 225, no. 10, pp. 1347–1364, 2011.
- [40] H. Wang and G. Song, "Fault detection and fault tolerant control of a smart base isolation system with magneto-rheological damper," *Smart Materials and Structures*, vol. 20, no. 8, Article ID 085015, 9 pages, 2011.
- [41] Y. Vidal, L. Acho, F. Pozo, and J. Rodellar, "Fault detection in base-isolation systems via a restoring force observer," in *Proceedings of the Conference on Control and Fault-Tolerant Systems (SysTol '10)*, pp. 777–782, IEEE, Nice, France, October 2010.
- [42] C. Scherer, P. Gahinet, and M. Chilali, "Multiobjective output-feedback control via LMI optimization," *IEEE Transactions on Automatic Control*, vol. 42, no. 7, pp. 896–911, 1997.
- [43] P. Gahinet, P. Apkarian, and M. Chilali, "Affine parameter-dependent Lyapunov functions and real parametric uncertainty," *IEEE Transactions on Automatic Control*, vol. 41, no. 3, pp. 436–442, 1996.
- [44] S. Savaresi, C. Poussot-Vassal, C. Spelta, O. Sename, and L. Dugard, *Semi-Active Suspension Control for Vehicles*, Elsevier, Butterworth-Heinemann, 2010.
- [45] A.-L. Do, O. Sename, and L. Dugard, "LPV modeling and control of semi-active dampers in automotive systems," in *Control of Linear Parameter Varying Systems with Applications*, J. Mohammadpour and C. W. Scherer, Eds., pp. 381–411, Springer, New York, NY, USA, 2012.

- [46] P. Apkarian and P. Gahinet, "A convex characterization of gain-scheduled H_∞ controllers," *IEEE Transactions on Automatic Control*, vol. 40, no. 5, pp. 853–864, 1995.
- [47] J. Lozoya-Santos, J. Tudón-Martínez, R. Morales-Menendez, R. Ramírez-Mendoza, and L. Garza-Castañón, "A fault detection method for an automotive magneto-rheological damper," in *Proceedings of the 8th IFAC International Symposium on Fault Detection, Supervision and Safety for Technical Processes*, pp. 1209–1214, Mexico City, Mexico, 2012.

Research Article

Thermodynamic Behaviors of a Kind of Self-Decoupling Magnetorheological Damper

Guojun Yu,¹ Chengbin Du,² and Tiger Sun¹

¹Faculty of Civil Engineering and Mechanics, Jiangsu University, Zhenjiang, Jiangsu 212013, China

²Department of Engineering Mechanics, Hohai University, Nanjing 210098, China

Correspondence should be addressed to Tiger Sun; ts420@ujs.edu.cn

Received 8 January 2015; Accepted 27 March 2015

Academic Editor: Weihua Li

Copyright © 2015 Guojun Yu et al. This is an open access article distributed under the Creative Commons Attribution License, which permits unrestricted use, distribution, and reproduction in any medium, provided the original work is properly cited.

A theoretical model of temperature change on a kind of self-decoupling magnetorheological (SDMR) damper was established based on conservation of energy, and the constraint equation for structural design parameters of the SDMR damper was improved to satisfy heat dissipation requirements in this work. According to the theoretical model and improved constraint equation, the main structure parameters of SDMR damper were obtained and the damper was tested. The temperature performance test results indicate that the rising temperature makes the damping force decline, and the main affection factors of temperature variation are excitation methods and input current. The results also show that the improved constraint equation and design method introduced are correct and efficient in the engineering.

1. Introduction

The magnetorheological (MR) damper is an excellent and controllable damper based on MR intelligent materials [1–4]. Its biggest advantage is that a computer can be used to adjust the parameters automatically according to the structure's vibration response [5, 6], thus achieving the best effect for the intelligent control of structure vibration. MR dampers using civil engineering structure control have large stress amplitude and sudden change in work current [7, 8], therefore making the energy caused by an earthquake or wind vibration convert more internal heat. Thus, the working temperature of MR damper increases greatly in a short time, which is a topic rarely studied both in the country and abroad. Goncalves and Ahmadian [9] studied the energy dissipated in an MR damper for semiactive vehicle suspensions and recognized that there is a decline in the performance of the damper due to temperature changes. Liu et al. [10] studied semiactive suspension control of a High Mobility Multipurpose Wheeled Vehicle (HMMWV) using the fail-safe MR damper; the results indicate that temperature changes greatly influence the performance of the suspension system. Gordaninejad and Kelso [11] analysed the effect of heat transfer when the damper used in off-highway,

high-payload vehicles, and a fluid-mechanics-based theoretical model along with a 3D finite element electromagnetic analysis is utilized to predict the MRF damper performance. Dogrouz et al. [12, 13] presented a lumped system model for predicting the heat transfer from fail-safe MR fluid dampers, and the results show that the model slightly overpredicts the temperature rise when compared to experimental data, the heat transfer can be considerably enhanced with the use of the fins, and both the mechanical and electrical power input contribute substantially to the temperature rise. Ramos et al. [14] presented a model to predict the thermal performance of automotive twin-tube shock absorbers simulating a thermal stability test. To get a better correlation between the model and the experimental results, it was proposed that the temperatures of the internal components of the shock absorber are measured to adjust the coefficients of the internal convection correlations. Batterbee and Sims [15] considered temperature sensitive controller performance of MR dampers. A dynamic temperature-dependent model of an MR damper was first developed and validated. Wilson and Wereley [16] presented a physically motivated model to capture the MR damper behavior, including the contributions of fluid and pneumatic stiffness of the damper realized at high piston velocity. The effect of damper self-heating

on the model parameters was investigated and the trends with temperature variation are presented. Marr et al. [17] developed a nonlinear, temperature-dependent model, which demonstrates the ability to capture trends in both frequency and dynamic displacement for both the storage and loss moduli over a range of frequencies (0.35 Hz–15 Hz), a range of displacements (0.005 in–0.3 in), and a range of temperatures (−40°F–140°F). The model is able to predict the more pronounced nonlinearities at the higher frequencies, higher displacements, and large temperature changes. Black and Makris [18] summarized the results from a comprehensive experimental program in an effort to better understand the phenomenon of viscous heating of fluid dampers under small-stroke (wind loading) and large-stroke (earthquake loading) motions. The study presents a valuable formula that can be used in practice to estimate the internal fluid temperature of the damper given the external shell temperature.

The existing MR dampers are designed for the linear vibration of structures; the damping effect is obvious for the structure of weak nonlinearity. When MR dampers are installed within the skeleton of buildings to suppress the low degree earthquakes or wind-induced vibrations, the piston displacements and velocities are relatively small. In contrast, there are a lot of the strong nonlinear behaviors in actual structures when strong earthquakes occur; the MR dampers are incorporated either in the seismic isolation system of structures or between the towers/peers and the deck of bridges; the piston displacements and velocities can be large [18]. The damper design for the application of nonlinear structure has become an important research field. MR dampers suppress the kinetic energy of structures into heat. When the dampers undergo large displacement histories and small but prolonged displacement histories, the temperature rise within the MR fluid of the damper might be appreciable to the extent that it may damage the damper.

This work presents a comprehensive experimental study on the problem of viscous heating of MR dampers. We developed a self-decoupling magnetorheological (SDMR) damper with a 360 kN maximum damping force and the SDMR damper is suitable for the vibration control of nonlinear civil engineering structures, and it consists of self-decoupling device which is activated depending on the structure displacement [19]. The paper explored the influence of temperature changes on the damper performance. We analyzed the temperature change when the damper is at work to provide theoretical basis for valuable formula modeling and simulation and for further experimental research.

2. Design Principle and Thermodynamics of SDMR Damper

The damping force equation of the SDMR damper is given [19]. Consider

$$F = \frac{3\eta L [\pi (D_i^2 - d^2)]^2}{4\pi D_i h^3} \dot{x} + \frac{3L\pi (D_i^2 - d^2) [1 + J(x)]}{4h} \tau_y \operatorname{sgn}(\dot{x}) + K(x), \quad (1)$$

where

$$J(x) = \begin{cases} \frac{x \operatorname{sgn}(\dot{x}) + S - 2x_0}{x_0}, & -S \leq x \operatorname{sgn}(\dot{x}) \leq x_0 - S \\ -1, & x_0 - S \leq x \operatorname{sgn}(\dot{x}) \leq x_0 + x_1 - S \\ \frac{x \operatorname{sgn}(\dot{x}) + S - 2x_0 - x_1}{x_0}, & x_0 + x_1 - S \leq x \operatorname{sgn}(\dot{x}) \leq 2x_0 + x_1 - S \\ 0, & 2x_0 + x_1 - S \leq x \operatorname{sgn}(\dot{x}) \leq S \end{cases}$$

$$K(x) = \begin{cases} kx \operatorname{sgn}(x) \operatorname{sgn}(\dot{x}), & S \leq C \\ -kx, & x \operatorname{sgn}(\dot{x}) < C - S, S > C \\ kx, & C - S < x \operatorname{sgn}(\dot{x}) < 2C - S, S > C \\ 0, & x \operatorname{sgn}(\dot{x}) > 2C - S, S > C, \end{cases} \quad (2)$$

where F is the damping force, L is the effective length of the piston, D_i is the cylindrical inner diameter, d is the diameter of the rod, h is the size of the working space, v is the piston velocity, τ_y is the yield stress of the MRF, and η is the off-state viscosity of the MRF. S is the amplitude, x_0 is the absolute value of the critical displacement for the delay, x_1 is the empty trip of the damper, C is the maximum compression of the spring, and k is the spring elastic constant. $\eta = \eta_0 e^{-\lambda(T-T_0)}$, where η and η_0 are the viscosity of the MR fluid at T and T_0 and λ is the viscosity-temperature coefficient. The changes in the damping magnetic field depend on the changes in the current, relative magnetic conductance, resistivity, and the material's specific heat while the temperature is changing [20].

For the MR damper, the main sources of heat are liquid damping, friction, and magnetic coil. When used under general conditions, the heat caused by friction is usually lesser than that caused by liquid damping, and we assume that the energy dissipation in the MR damper work process includes only the liquid damping and magnetic coil. The energy balance equation of MR damper is given by

$$W_1 + W_2 - Q = \Delta U. \quad (3)$$

The work done when the damper dissipates external input energy is

$$W_1 = F \cdot X(t). \quad (4)$$

Using (4), (1) becomes

$$W_1 = \left\{ \frac{3\eta L [\pi (D_i^2 - d^2)]^2}{4\pi D_i h^3} \dot{x} + \frac{3L\pi (D_i^2 - d^2) [1 + J(x)]}{4h} \cdot \tau_y \operatorname{sgn}(\dot{x}) + K(x) \right\} \cdot X(t). \quad (5)$$

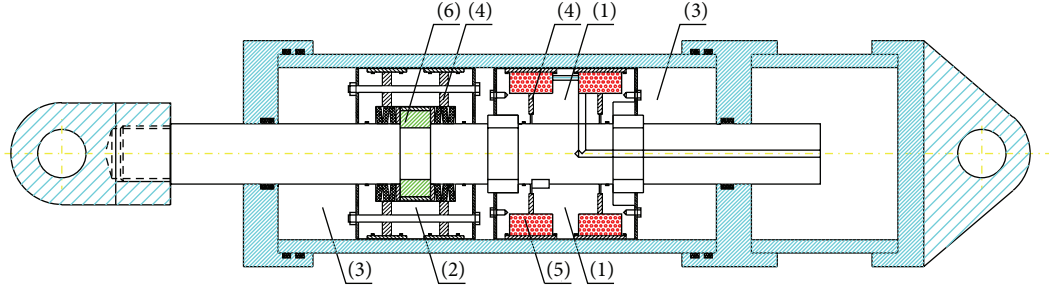


FIGURE 1: Structure of the SDMR damper.

According to Ohm's Law, the heat generated by the damper field coil is

$$W_2 = I^2(t) R t, \quad (6)$$

where t is time.

According to the theory of heat conduction, the heat exchange between the damper and the environment outside the damper is

$$Q = \alpha A (T - T_0) t, \quad (7)$$

where A is the damper's total heat area given by

$$A = \left(\frac{\pi D^2}{2} + \pi D l \right). \quad (8)$$

And α is the damper's coefficient of total heat dissipation. Considering comprehensively the convection, radiation, and effect of heat transfer, α can be written as [21]

$$\alpha = \frac{4v_0^{0.7}}{D^{0.3}} + \varepsilon\sigma_b \left(\frac{T_a^4 - T_{a0}^4}{T_a - T_{a0}} \right). \quad (9)$$

Using (5)–(9), (3) becomes

$$\left\{ \frac{3\eta L [\pi (D_i^2 - d^2)]^2}{4\pi D_i h^3} \dot{x} + \frac{3L\pi (D_i^2 - d^2) [1 + J(x)]}{4h} \tau_y \operatorname{sgn}(\dot{x}) + K(x) \right\} \cdot X(t) + I^2(t) R t - \left[\frac{4v_0^{0.7}}{D^{0.3}} + \varepsilon\sigma_b \left(\frac{T_a^4 - T_{a0}^4}{T_a - T_{a0}} \right) \right] \cdot \left(\frac{\pi D^2}{2} + \pi D l \right) \cdot (T - T_0) t = \Delta T \cdot C_{\text{sum}}, \quad (10)$$

where ΔU is the internal energy dissipation that causes temperature changes in the damper, X is the exerting displacement, v_0 is the relative velocity of air, ε is the blackening coefficient of the outside wall, l is the length of the work cylinder, $\sigma_b = 5.67 \times 10^{-8}$ is the radiation constants of the absolute blackbody [21], T_a and T_{a0} are the absolute temperatures at T and T_0 , respectively, C_{sum} is the entire heat capacity of the damper, and ΔT is the temperature change of the damper.

3. Design of SDMR Damper

3.1. Structural Design. The SDMR damper in this paper, as shown in Figure 1, is a kind of damper used in civil engineering structures for antivibration, specifically an antivibration device with damping force decoupling characteristics and protection from self-invalidation. The damper's stiffness and damping characteristics are very sensitive to the incentive's frequency and amplitude. It has a relatively small damping force in the case of small amplitudes and a large damping force in the case of large amplitudes, and the damping force can be adjusted; thus, the damper can effectively reduce the structure's reaction to various vibration excitations and has good stability and invalidation protection. The core work parts are the main piston (1) and the two subpistons (2), the work cylinder filled with MR fluid (3), the main piston ring with a permanent magnet (4) and magnetic coil (5), and the permanent magnet self-decoupling baffle in the subpiston magnetizer (6).

The SDMR damper is mainly used in building structures; therefore, large and small displacements in the damper design are 60 mm and 5 mm, respectively. The existing MR dampers are designed for the linear vibration of structures; the damping effect is obvious for the structure of weak nonlinearity. When MR dampers are installed within the skeleton of buildings to suppress the low degree earthquakes or wind-induced vibrations, the piston displacements and velocities are relatively small. Therefore, a damper with a small damping force is required for vibration control. The core work part of the SDMR damper is the main piston (1). In contrast, there are a lot of the strong nonlinear behaviors in actual structures when strong earthquakes occur; the MR dampers are incorporated either in the seismic isolation system of building structures or between the towers/peers and the deck of bridges; the piston displacements and velocities can be large. Therefore, a damper with a large damping force is better for vibration control. The core work parts of the SDMR damper are the main piston (1) and the two subpistons (2).

3.2. Magnetic Circuit Design. The basic principle of a SDMR damper can be described as the permanent magnet and magnetic coil in the main piston magnetic circuit with the excitation magnetic field and the permanent magnetic field. The coil used winds inwards, and two coils are placed in parallel. The current magnetic field of the coil can strengthen

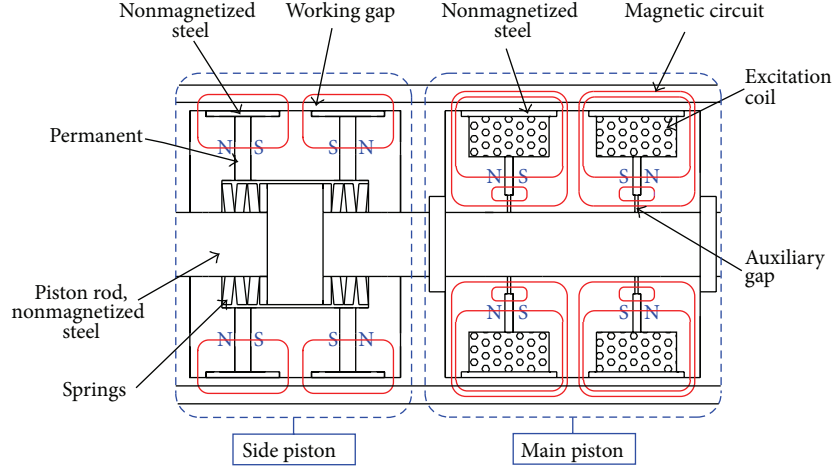


FIGURE 2: Flux lines of the SDMR damper.

or weaken the magnetic field of the permanent magnet in the damping channel [22]. In the subpiston, we set only the permanent magnet. The distribution of magnetic flux lines is shown in Figure 2.

The permeable magnetic material adopted is steel 45#, and the permanent magnetic material adopted is no. 30 NdFeB. In addition, with the introduction of a permanent magnet in the magnetic structure, even in the case of a loss of external energy, the damper can still guarantee a larger damping force. It overcomes the dependence of the traditional MR damper on the external energy. As mentioned previously, the damper is suitable for vibration control of civil engineering structures.

3.3. Temperature Effect on MR Viscosity and Magnetic Circuit.

To achieve the purpose of reducing the vibration, the vibration energy of the SDMR damper translates into heat energy stored in the interior of the damper. Parts of the heat dissipate through the cylinder wall into the air through convection, conduction, and radiation, whereas other parts remain and increase the temperature in the form of internal energy to obtain a balance temperature.

The damping force includes the viscous damping force and the Coulomb damping force. The viscous damper is only related to the speed and viscosity of the MR fluid, $\eta = \eta_0 e^{-\lambda(T-T_0)}$, where λ is the viscosity-temperature coefficient. The trend of the SDMR damper's viscosity is presented in Figure 3. The changes in the Coulomb damping force depend mainly on the magnetic field changes, whereas the changes in the magnetic field depend on the changes in current, relative magnetic conductance, resistivity, and the material's specific heat during temperature changes. The relationship curve between the MR fluid shear yield strength and the magnetic field intensity is shown in Figure 4, whereas the relationship among the relative magnetic conductance, specific heat, and resistivity of 45# steel with the temperature changes is shown in Table 1 [23].

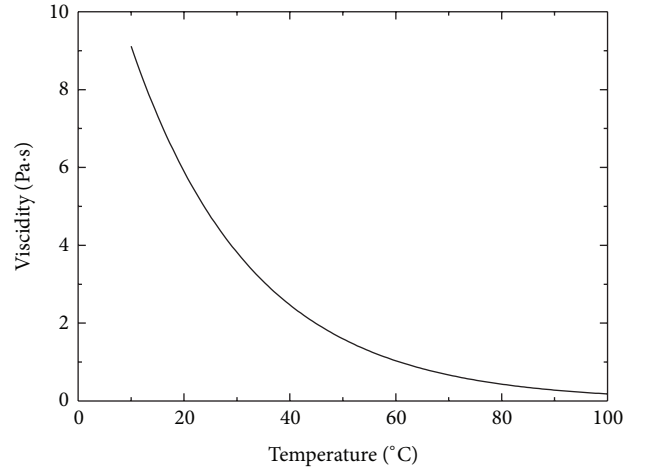


FIGURE 3: Variety trend of SDMR damper's viscosity.

3.4. Optimization Parameter. The temperature increase of the MR fluid is not unlimited when the MR damper is at work. The damper needs to obtain thermal balance when the temperature is critical. Therefore, in the damper design, the allowable working temperature must be considered to prevent exorbitant temperature that leads to failure.

The allowable temperature of the MR damper depends on the following three aspects: (1) flash points of the temperature of the MR fluid, (2) stable boundary temperature of the damper sealing material, and (3) allowable temperature that satisfies the damper performance requirements, namely, the temperature when the damper's rated typical set-point damping force declines to the limit because of the increase in working temperature. The temperature should no longer increase when the damper reaches the allowable temperature, and at this time the heat dissipation and outside work should be the same as in (3). The dissipated heat when the damper reaches its allowable temperature, T_x , is $\Delta T \cdot C_{\text{sum}}$.

TABLE 1: Temperature properties of 45# steel.

Temperature (°C)	Resistivity ($\times 10^{-7} \Omega \cdot m$)	Permeability	Specific heat ($J \cdot (kg \cdot K)^{-1}$)
0	1.84	300	470
80	2.35	295	480
160	2.86	290	500
240	3.84	282	520
320	4.72	275	540
400	5.58	268	550

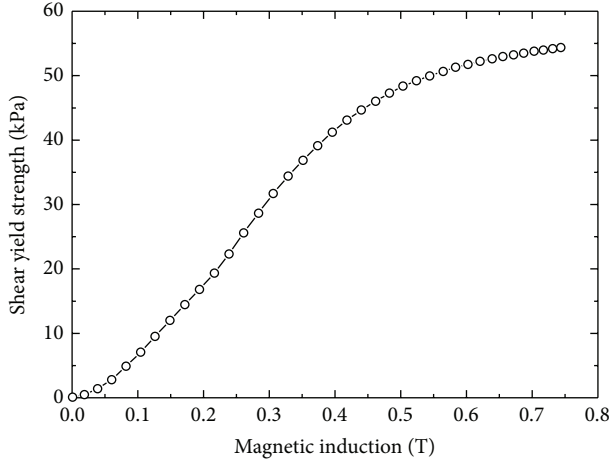


FIGURE 4: Curve between shear stress and magnetic induction.

Considering the effect of viscosity-temperature coefficient on the viscous damping force and that of temperature on the relative magnetic conductance resistivity of the damper magnetic materials, which influence the magnetic induction intensity of damping clearances, we can define the Coulomb force attenuation coefficient ζ , resistance coefficient δ , and heat coefficient φ . Thus, with (10), we can calculate the allowable temperature using the following equation:

$$\left\{ \begin{aligned} & \frac{3\eta_0 e^{-\lambda(T_x - T_0)} L [\pi (D_i^2 - d^2)]^2}{4\pi D_i h^3} \dot{x} \\ & + \frac{3\zeta L \pi (D_i^2 - d^2) [1 + J(x)]}{4h} \tau_y \operatorname{sgn}(\dot{x}) + K(x) \end{aligned} \right\} \quad (11)$$

$$\cdot X(t) + \delta I^2(t) R t - \left[\frac{4v_0^{0.7}}{D^{0.3}} + \varepsilon \sigma_b \left(\frac{T_a^4 - T_{a0}^4}{T_a - T_{a0}} \right) \right]$$

$$\cdot \left(\frac{\pi D^2}{2} + \pi D l \right) \cdot (T_x - T_0) t = \Delta T \cdot \varphi \cdot C_{\text{sum}}.$$

With these operating conditions, we can design the damper's heat-radiating parameters when the allowable temperature of the MR damper is decided. The improved constraint equations can also be used as constraint conditions for the heat dissipation factors in the structural design process. After repeatedly adjusting the design parameters, we finally



FIGURE 5: The photo of SDMR damper.

confirmed that the main thermal parameters of the damper include the damper outside wall thickness, ε , the cylinder's external diameter, D , and the cylinder length, l . The main parameters of the final damper design are shown in Table 2, $L = L_m + L_s$, and the SDMR damper is shown in Figure 5.

4. Temperature Characteristic Test of the SDMR Damper

To validate the rationality and feasibility of the SDMR damper design and study the one performance, we conducted a temperature characteristic test on the electrohydraulic servodynamic-static tester (SDS-300) at the Material Mechanics Laboratory of the Mechanics Experimental Centre of Hohai University. The experimental setup of the SDMR damper is shown in Figure 6. The test uses displacement control method, with the sine curve as the input. The test cases are presented in Table 3. When the current values of cases are 0 A, the damper can still guarantee a larger damping force under the magnetic field produced by the permanent magnet.

5. Results and Discussion

The test environment temperature is 28.8°C using the TES1327 K infrared thermometer to measure the temperature of the damper's external cylinder. Figures 7 and 8 show the time process of the SDMR damper temperature variation

TABLE 2: Main structural parameters of the SDMR damper.

Main structural parameters	Coefficient	Unit	Value
Initial MRF viscosity	η	Pa·s	4.7
MRF yield strength	τ_y	kPa	54
Work clearances	h	mm	1.2
Cylinder external diameter	D	mm	230
Cylinder inner diameter	D_i	mm	200
Piston pod diameter	d	mm	70
Spring effective itinerary	C	mm	5
Main piston work channel length	L_m	mm	40
Total length	l	mm	996
Force range of small itinerary	F	kN	16.1~195.7
Force range of large itinerary	F	kN	195.7~362.2
Coil circle number	n	—	800
Entirety heat capacity	C_{sum}	$\text{kJ}\cdot(\text{K})^{-1}$	427.5
Critical temperature	T	$^{\circ}\text{C}$	100
The maximum power	P	W	<100
Current range	I	A	-2~2
Subpiston work channel length	L_s	mm	40
Coil total resistance	R	Ω	23.8
Blackening coefficient of the outside wall	ε	—	0.95
The Coulomb force attenuation coefficient	ζ	—	0.93~0.95
Resistance coefficient	δ	—	0.98~0.99
Heat coefficient	φ	—	0.91~0.94



FIGURE 6: Experimental setup of a SDMR damper.

TABLE 3: MR damper temperature performance test cases.

Case	Current (A)	Amplitude (mm)	Frequency (Hz)
1	0	5	0.5
2	2	5	0.5
3	2	5	1.3
4	0	60	0.1

for the four cases. We selected case 4 to draw the hysteric curve of the damping force as it changed with temperature,

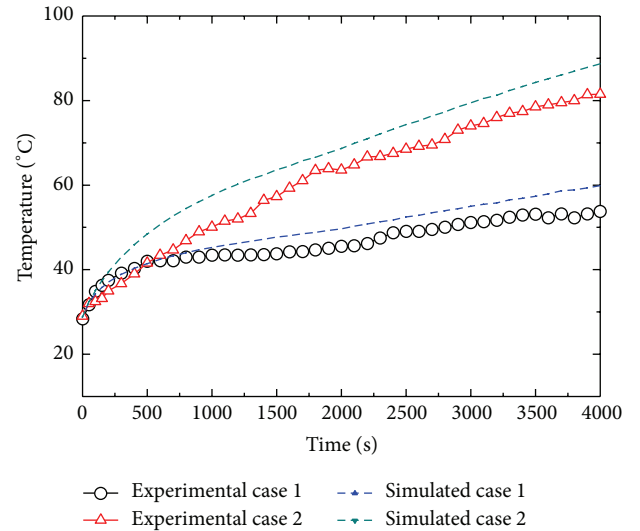


FIGURE 7: Various temperatures of an MR damper with case 1 and case 2.

as shown in Figure 9. Table 4 presents the test results of the damping characteristics affected by temperature.

From the above test results, we can obtain the following conclusions.

- (1) In Figures 7 and 8, the temperature of the MR damper changes while it is at work, which is roughly a linear change. The main influencing factors for the damper

TABLE 4: Test results of the MR damper characteristics.

Case	Highest temperature (°C)	Range of temperature (°C)	Damping force change (kN)	Damping reduction (%)
1	53.8	25.4	117.3~109.4.1	6.73
2	81.5	52.5	169.8~157.9	7.01
3	95.5	67.1	178.1~167.5	5.95
4	99.1	70.3	297.7~275.1	7.59

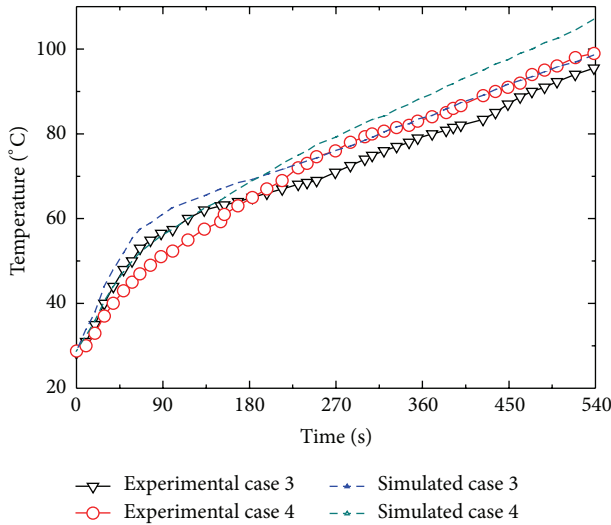


FIGURE 8: Various temperatures of an MR damper with case 3 and case 4.

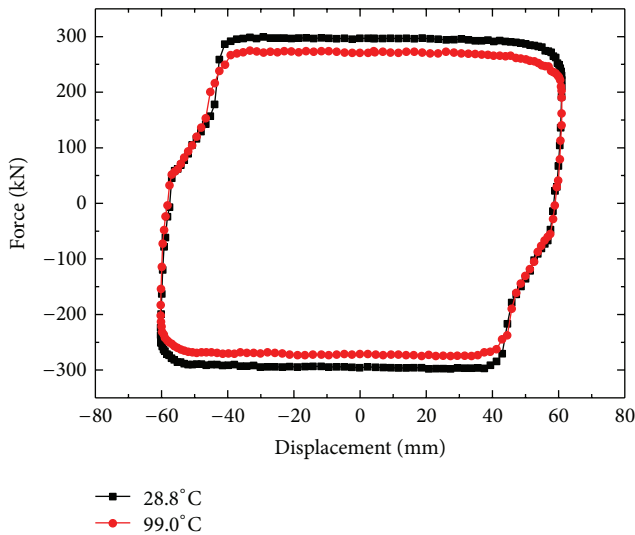


FIGURE 9: Curves of damper force changes with respect to temperature.

temperature changes are incentive methods and work current. Comparing the curves of the temperature changing with time for cases 1 and 2 in Figure 7, in certain frequencies and amplitudes, the temperature of case 2 that switches with the current rises faster than the temperature of case 1, which shows an obvious effect of the current.

- (2) Under the case of switching on the current and changing the incentive, the temperature curve of the damper becomes flat after 4000 s, consistent with the theoretical calculation. Comparing the theoretical and measured curves in Figures 7 and 8, the measured value is slightly lower than the theoretical value, due to the fact that the theoretical value is the internal temperature of the damper and the measured value is the surface temperature of the damper. Therefore, we can conclude that the MR damper balance temperature can be determined through the parameter design. As the wind excitation time on the building structure is much longer than the earthquake excitation time, the performance of the SDMR damper is important in the use of the wind vibration control in civil engineering.
- (3) Comparing the curves of cases 2 and 3 in Figures 7 and 8, the initial temperature rise of the damper in the case of high frequency incentive is faster than that in the case of low frequency incentive.
- (4) According to Figure 9 and Table 4, the damping force of the MR damper declines when the temperature rises. For civil engineering, seismic events only occur for dozens of seconds, and the temperature rises by 5°C. The damping force attenuation is so little that we can ignore its influence on civil engineering structures. Thus, the SDMR damper we designed has good temperature stability.

6. Conclusion

As the energy dissipation equipment designed SDMR damper's temperature is changing during the work time which caused damper capability decline. For this reason, the effect of temperature was studied and the following conclusions were obtained.

- (1) Based on conservation of energy theory, a theoretical model of temperature change of SDMR damper was established, and the constraint equation for structural design parameters of the MR damper was improved to satisfy heat dissipation requirements.
- (2) According to the theoretical model and improved constraint equation, main structure parameters of a SDMR damper were obtained and the damper was tested. The temperature performance test result indicates that the rising temperature makes the damping force decline, and the main affecting factors of

temperature variation are excitation methods and input current.

- (3) The key technology research on structure, heat dissipation, and heating behaviour tests of SDMR damper also show that the improved constraint equation and design method introduced are correct and efficient. The temperature of SDMR damper achieves a dynamic balance after 4000 s; the behavior of the SDMR damper is important in the use of the wind vibration control in civil engineering.
- (4) The key technology on structure, magnetic circuit, heat dissipation, and temperature characteristic tests of SDMR damper could provide reference for a large-tonnage MR damper in the aspects of reasonable parameter determination, design, and proper manufacturing. It also provides the basis for the nonlinear vibration control design of actual civil building structures that make use of MR dampers.

Conflict of Interests

The authors declare that there is no conflict of interests regarding the publication of this paper.

Acknowledgments

This work was supported by the Natural Science Foundation of Jiangsu Province of China (Grant no. BK20140560), the Research Foundation for Advanced Talents of Jiangsu University (Grant nos. 14JDG161, 14JDG162), and the Jiangsu Province Science and Technology Support Program, China (Grant no. BE2012180).

References

- [1] M. Zapateiro, H. R. Karimi, N. Luo, and B. F. Spencer Jr., "Real-time hybrid testing of semiactive control strategies for vibration reduction in a structure with MR damper," *Structural Control and Health Monitoring*, vol. 17, no. 4, pp. 427–451, 2010.
- [2] B. J. Park, F. F. Fang, and H. J. Choi, "Magnetorheology: materials and application," *Soft Matter*, vol. 6, no. 21, pp. 5246–5253, 2010.
- [3] H. W. Huang, L. M. Sun, and X. L. Jiang, "Vibration mitigation of stay cable using optimally tuned MR damper," *Smart Structures and Systems*, vol. 9, no. 1, pp. 35–53, 2012.
- [4] S. N. Madhekar and R. S. Jangid, "Seismic response control of benchmark highway bridge using variable dampers," *Smart Structures and Systems*, vol. 6, no. 8, pp. 953–974, 2010.
- [5] S. J. Dyke, B. F. Spencer Jr., M. K. Sain, and J. D. Carlson, "An experimental study of MR dampers for seismic protection," *Smart Materials and Structures*, vol. 7, no. 5, pp. 693–703, 1998.
- [6] S.-Y. Ok, D.-S. Kim, K.-S. Park, and H.-M. Koh, "Semi-active fuzzy control of cable-stayed bridges using magnetorheological dampers," *Engineering Structures*, vol. 29, no. 5, pp. 776–788, 2007.
- [7] G. Yang, B. F. Spencer Jr., J. D. Carlson, and M. K. Sain, "Large-scale MR fluid dampers: modeling and dynamic performance considerations," *Engineering Structures*, vol. 24, no. 3, pp. 309–323, 2002.
- [8] J. W. Tu, J. Liu, W. L. Qu, Q. Zhou, H. B. Cheng, and X. D. Cheng, "Design and fabrication of 500-kN large-scale MR damper," *Journal of Intelligent Material Systems and Structures*, vol. 22, no. 5, pp. 475–487, 2011.
- [9] F. D. Goncalves and M. Ahmadian, "Experimental investigation of the energy dissipated in a magneto-rheological damper for semi-active vehicle suspensions," *American Society of Mechanical Engineers*, vol. 72, no. 1, pp. 459–467, 2003.
- [10] Y. M. Liu, F. Gordaninejad, C. A. Evrensel et al., "Temperature-dependent skyhook control of HMMWV suspension using a fail-safe magnetorheological damper," in *Smart Structures and Materials 2003: Industrial and Commercial Applications of Smart Structures Technologies*, vol. 5054 of *Proceedings of SPIE*, pp. 332–340, San Diego, Calif, USA, August 2003.
- [11] F. Gordaninejad and S. P. Kelso, "Fail-safe magneto-rheological fluid dampers for off-highway, high-payload vehicles," *Journal of Intelligent Material Systems and Structures*, vol. 11, no. 5, pp. 395–406, 2000.
- [12] M. B. Dogrouz, F. Gordaninejad, and A. J. Stipanovich, "An experimental study on heat transfer from fail-safe magneto-rheological fluid dampers," in *Smart Structures and Materials 2001: Damping and Isolation*, vol. 4331 of *Proceedings of SPIE*, pp. 355–369, July 2001.
- [13] M. B. Dogrouz, E. L. Wang, F. Gordaninejad, and A. J. Stipanovich, "Augmenting heat transfer from fail-safe magneto-rheological fluid dampers using fins," *Journal of Intelligent Material Systems and Structures*, vol. 14, no. 2, pp. 79–86, 2003.
- [14] J. C. Ramos, A. Rivas, J. Biera, G. Sacramento, and J. A. Sala, "Development of a thermal model for automotive twin-tube shock absorbers," *Applied Thermal Engineering*, vol. 25, no. 11–12, pp. 1836–1853, 2005.
- [15] D. Batterbee and N. D. Sims, "Temperature sensitive controller performance of MR dampers," *Journal of Intelligent Material Systems and Structures*, vol. 20, no. 3, pp. 297–309, 2009.
- [16] N. L. Wilson and N. M. Wereley, "Analysis of a magnetorheological fluid damper incorporating temperature dependence," Technical Paper—51st AIAA/ASME/ASCE/AHS/ASC Structures, Structural Dynamics, and Materials Conference AIAA 2010-2993, 2010.
- [17] C. Marr, G. A. Lesieutre, and E. C. Smith, "Nonlinear, temperature-dependent, fluidlastic lead-lag damper modeling," in *Proceedings of the 2008 AHS Annual Forum Proceedings*, vol. 3, pp. 2370–2381, AHS International, 2008.
- [18] C. J. Black and N. Makris, "Viscous heating of fluid dampers under small and large amplitude motions: experimental studies and parametric modeling," *Journal of Engineering Mechanics*, vol. 133, no. 5, pp. 566–577, 2007.
- [19] C. B. Du, F. X. Wan, and G. J. Yu, "A magnetic flux leakage study of a self-decoupling magnetorheological damper," *Smart Materials and Structures*, vol. 20, no. 6, Article ID 065019, pp. 65–76, 2011.
- [20] G. Yu, C. Du, and F. Wan, "Numerical simulation of a self-decoupling magneto-rheological damper on electromagnetic-thermal coupling," *Advanced Materials Research*, vol. 139–141, pp. 2386–2390, 2010.
- [21] S. Q. Liu, K. K. Zhou, S. F. Yuan, B. Yao, and Y. S. Jia, "Temperature characteristic of one tube MR damper," *Tractor & Farm Transporter*, vol. 35, no. 2, pp. 14–16, 2008 (Chinese).

- [22] W.-M. Yan, J.-B. Ji, B. Dong, and H.-J. Ge, "Theoretical and experimental studies on a new reversible magnetorheological damper," *Structural Control and Health Monitoring*, vol. 18, no. 1, pp. 1–19, 2011.
- [23] A. R. Kiani-Rashid, G. I.-A. Bozchalooi, and H. R. Azzat-Pour, "The influence of annealing temperature on the graphitisation of CK 45 Steel," *Journal of Alloys and Compounds*, vol. 475, no. 1-2, pp. 822–826, 2009.

Research Article

Frequency Dependent Spencer Modeling of Magnetorheological Damper Using Hybrid Optimization Approach

Ali Fella Jahromi, Rama B. Bhat, and Wen-Fang Xie

Department of Mechanical and Industrial Engineering, Concordia University, Montreal, QC, Canada H3G 1M8

Correspondence should be addressed to Ali Fella Jahromi; fellajahromi@gmail.com

Received 23 December 2014; Revised 5 March 2015; Accepted 5 March 2015

Academic Editor: Weihua Li

Copyright © 2015 Ali Fella Jahromi et al. This is an open access article distributed under the Creative Commons Attribution License, which permits unrestricted use, distribution, and reproduction in any medium, provided the original work is properly cited.

Magnetorheological dampers have been widely used in civil and automotive industries. The nonlinear behavior of MR fluid makes MR damper modeling a challenging problem. In this paper, a frequency dependent MR damper model is proposed based on Spencer MR damper model. The parameters of the model are identified using an experimental data based hybrid optimization approach which is a combination of Genetic Algorithm and Sequential Quadratic Programming approach. The frequency in the proposed model is calculated using measured relative velocity and relative displacement between MR damper ends. Therefore, the MR damper model will be function of frequency. The mathematical model is validated using the experimental results which confirm the improvement in the accuracy of the model and consistency in the variation damping with the frequency.

1. Introduction

The semiactive control system provides both features of passive and active devices in terms of reliability and adaptability. Using semiactive system, the rate of energy dissipation becomes controllable, while, in active control devices, the energy can be added to the system to control the dynamic response. Magnetorheological (MR) damper is a semiactive control device which is commonly used in vehicle industries and structural applications. The MR damper contains MR fluid instead of regular oil. The MR fluid is a smart material which contains micron sized magnetic polarized metal particles which provide variable viscous damping with changing magnetic field [1]. The application of MR fluid is dependent on three different operational modes: flow, squeeze-flow, and shear [2]. For instance, MR dampers and servovalves are designed based on flow mode of MR fluid [3]. The squeeze-flow mode of MR fluid is utilized in the application of impact control dampers for large forces [3]. The shear mode can be used for brakes, clutches, and damping layer of sandwich structures [3]. In order to describe the dynamic behavior of the MR damper, different mathematical models have been proposed in both discrete and continuous time domain.

Modeling of MR damper by using black box nonlinear models is carried out in discrete time domain [4] where MR damper hysteresis, function of displacement, and velocity are modeled by Neural Network (NN). In this model, three parameters are indicated based on the collected experimental input and output data. However, the nonmodel based parameter identification is only valid for the system operation range during which the experimental data are collected and used for training the NN model. Therefore the accuracy of model cannot be guaranteed for extrapolating the range of operation.

The Bingham viscoplastic MR damper model [5] is built in continuous time domain and it describes the dynamic behavior of MR damper based on measuring the shear stress and the shear strain rate. The Bingham model consists of a Coulomb friction element parallel with viscous damping. Using Bingham model, the storage energy in the MR damper cannot be modeled. Moreover, the difference between the simulated force and the real force increases when the velocity is near zero.

The modified Bingham MR damper model proposed by Gamota and Filisko [6] is a viscoelastic-plastic model. The so-called Gamota and Filisko model is a Bingham model which

is in series with a parallel set of spring and viscous damper. The Gamota and Filisko MR damper model improves the accuracy of the model in describing the hysteresis loop and storage energy of the MR damper. However, the simulation of this modified Bingham model needs step size in the order of 10^{-6} which is the main drawback of this model [1].

The Bouc-Wen model [7] is a continuous, viscoelastic-plastic model which can describe a wide range of hysteresis behavior [1]. The hysteresis behavior of Bouc-Wen model is described by an evolutionary variable with three coefficients of velocity which results in smoothness of transition from the preyield to the postyield region. The roll-off effect cannot be simulated using Bouc-Wen model in the region of the small magnitude of the velocity where the velocity and acceleration have opposite directions [1].

In the Spencer MR damper model [1], a spring and a viscous damping element are added to the Bouc-Wen model to simulate the roll-off effect at small velocities. Therefore, the other pair of damping and stiffness elements can be adjusted for small velocities or high frequency region. The Spencer model is capable of simulating the roll-off effect in all velocity and acceleration regions. In the Spencer model, the assigned damping coefficients only depend on the changing current. However, the MR damper viscosity depends on the frequency of excitation [8] and temperature of MR fluid [9]. And in the literature, MR damper models cannot describe such frequency dependent behavior.

The present study deals with the variation of MR fluid viscosity with the frequency of the excitation in Spencer MR damper model. The viscosity of the MR damper is modeled using two viscous damping elements for large and small velocities. The MR model is identified by minimizing the error between the experimental data and simulated data of the proposed model. The hybrid optimization approach is used for the identification which is a combination of Genetic Algorithms (GA) and Sequential Quadratic Program (SQP). The excitation frequency in real application can be calculated by measuring the velocity and the displacement of the MR damper. Therefore, the viscosity of MR fluid in Spencer model is described by exponential and Gaussian equations which are the functions of velocity and displacement for small and large velocity regions, respectively.

The rest of the paper is organized as follows. The modeling of MR damper is presented in Section 2. The experimental set-up and procedure are explained in Section 3. The optimization approach and characterization of MR damper model are discussed in Section 4. A comparison between the proposed model and experimental data is presented in Section 5. Finally the conclusions and future work are presented in Section 6.

2. Spencer Magnetorheological Damper Model

Due to the nonlinearity in dynamic behavior of MR damper, the accuracy and validity of the Spencer MR damper model over wide range of frequencies are not consistent. The schematic of the Spencer MR damper model is shown in

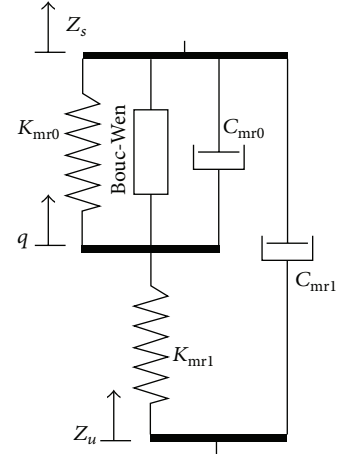


FIGURE 1: Schematic of Spencer model.

Figure 1. The governing equations of Spencer MR damper model are presented in the following [1]:

$$f_{MR} = C_{mr1} (\dot{q} - \dot{Z}_u) + K_{mr1} ((Z_s - Z_u) - Z_0), \quad (1)$$

$$\dot{q} = \frac{1}{C_{mr1} + C_{mr0}} (\alpha p + C_{mr0} \dot{Z}_s + C_{mr1} \dot{Z}_u + K_{mr0} (Z_s - q)), \quad (2)$$

$$\dot{p} = -\gamma |\dot{Z}_s - \dot{q}| |p|^{n-1} p - \beta (\dot{Z}_s - \dot{q}) |p|^n + A (\dot{Z}_s - \dot{q}), \quad (3)$$

where K_{mr1} and C_{mr1} are the MR damper accumulator stiffness and viscous damping coefficients for small velocities, respectively. Z_0 is the initial displacement associated with spring K_{mr1} . Further, K_{mr0} and C_{mr0} are accumulator stiffness and viscous damping coefficients for large velocities, respectively.

Equation (2) represents the internal state q which is used to define the roll-off due to the damping coefficient C_{mr1} . The MR damping force in (1) involves the nondimensional auxiliary variable p to define the hysteresis. The constants β and γ are the nondimensional values to present the hysteretic loop in the negative and positive slopes in (3). A describes the hysteresis loop size with respect to velocity. The scalar value n is used to represent the smoothness of transition of MR fluid from elastic to plastic [1, 10].

The α variable in (2) is a polynomial function of voltage to describe the MR fluid yield stress which is defined as a first order polynomial in (6). The variations of C_{mr1} and C_{mr0} with respect to the frequency of excitation are proposed by $C_{mr1}(\Delta Z, \Delta \dot{Z})$ and $C_{mr0}(\Delta Z, \Delta \dot{Z})$ in (4) and (5), respectively. The damping coefficients C_{mr1} and C_{mr0} are also functions of voltage as a first order polynomial in (4) and (5), respectively.

Equation (7) presents a filter to reach rheological equilibrium. Accordingly,

$$C_{mr1} = a_{c1} + b_{c1}u + C_{mr1}(\Delta Z, \Delta \dot{Z}), \quad (4)$$

$$C_{mr0} = a_{c0} + b_{c0}u + C_{mr0}(\Delta Z, \Delta \dot{Z}), \quad (5)$$

$$\alpha = a_\alpha + b_\alpha u, \quad (6)$$

$$\dot{u} = -\eta(u - V), \quad (7)$$

where η is constant for changing rate of magnetic field and V is the applied voltage. The peak value of relative velocity and peak to peak value of relative displacement of MR damper ends are $\Delta \dot{Z}$ and ΔZ , respectively.

3. Experimental Setup

In order to gather the experimental force, velocity, and displacement data of the MR damper, a MR damper RD 8041 manufactured by Lord Co. is connected to a hydraulic shaker in order to apply harmonic input at one end of MR damper at different frequencies. The experimental set-up consists of MR damper RD 8041, voltage controller kit UI 7000 manufactured by Lord Co., hydraulic pump controller, signal generator, voltmeter, oscilloscope, force sensor, and thermometer which are shown in Figures 2 and 3. The experimental data are gathered in two categories: displacement, velocity, and force for variation of frequency in range of 1.5 to 5 Hz in 0.5 (Hz) intervals.

The operating range of MR damper RD 8041 is 0 to 2 A and maximum temperature is 71°C. By increasing the frequency of excitation, the temperature of the MR fluid inside MR damper increases and is measured by a digital thermometer attached to the body of the MR damper as shown in Figure 3. Considering this constraint, the applicable maximum frequency is 5 Hz. The amplitude of the harmonic excitation is 0.00635 m.

4. Characterization of Magnetorheological Damper Model Using Hybrid Optimization Approach

In order to identify the parameters of Spencer model and to study the trend of viscosity versus frequency, the objective function is defined as the error between experimental data and mathematical data calculated using Spencer model. The objective function is defined in (8). The model variables defined in (1) to (7) are presented in (9):

$$f = \sum_{n=1}^m \frac{\|F_{MR}\| - |f_{MR}|}{m \times \max(|F_{MR}|)} \times 100, \quad (8)$$

$$x = K_{mr0}, K_{mr1}, a_{c0}, a_{c1}, b_{c0}, b_{c1}, a_\alpha, b_\alpha, A, \beta, \gamma, n, Z_0. \quad (9)$$

The constraints are defined to limit the search region. The linear constraints are defined as lower bounds and upper bounds in both GA and SQP optimization algorithms. The identification of the model parameters is carried out in two

TABLE 1: Parameters of MR damper [11].

Parameter	Quantity
K_{mr0}	3610 (N/m)
K_{mr1}	840 (N/m)
a_{c0}	784 (Ns/m)
a_{c1}	14649 (Ns/m)
b_{c0}	1803 (Ns/Vm)
b_{c1}	34622 (Ns/Vm)
a_α	12441 (N/m)
b_α	38430 (N/Vm)
A	58
β	205902 (1/m ²)
γ	136320 (1/m ²)
n	2
η	190 (1/s)
Z_0	0.0245 (m)

steps: (i) identifying ten parameters defined in (1) to (7) using experimental data at frequency of 2.5 Hz and zero volt and (ii) identifying $C_{mr1}(\Delta Z, \Delta \dot{Z})$ and $C_{mr0}(\Delta Z, \Delta \dot{Z})$ for frequency from 1.5 to 5 (Hz) in 0.5 (Hz) interval at zero current. Therefore, in the first step, the model has ten design variables and ten lower bounds and upper bounds as linear constraints which are presented in the following inequalities:

$$\begin{aligned} (K_{mr1})_l &\leq K_{mr1} \leq (K_{mr1})_u, \\ (K_{mr0})_l &\leq K_{mr0} \leq (K_{mr0})_u, \\ (a_{c1})_l &\leq a_{c1} \leq (a_{c1})_u, \\ (a_{c0})_l &\leq a_{c0} \leq (a_{c0})_u, \\ (a_\alpha)_l &\leq a_\alpha \leq (a_\alpha)_u, \\ (A)_l &\leq A \leq (A)_u, \\ (\beta)_l &\leq \beta \leq (\beta)_u, \\ (\gamma)_l &\leq \gamma \leq (\gamma)_u, \\ (n)_l &\leq n \leq (n)_u, \\ (Z_0)_l &\leq Z_0 \leq (Z_0)_u. \end{aligned} \quad (10)$$

The lower bound and upper bound of all design variables are given in Table 1 based on identified parameters for the MR damper in the same range of the force as in [11] considering $\pm 50\%$ variation.

A nonlinear constraint is defined in (11) to limit the feasible search region and to guarantee that the error between experimental data and mathematical model is less than 4%:

$$g = \left(\sum_{n=1}^m \frac{\|F_{MR}\| - |f_{MR}|}{m \times \max(|F_{MR}|)} \times 100 \right) \leq 4. \quad (11)$$

In order to identify the design variables $C_{mr1}(\Delta Z, \Delta \dot{Z})$ and $C_{mr0}(\Delta Z, \Delta \dot{Z})$, eight hybrid optimization algorithms are formulated based on eight experimental data sets in the range of

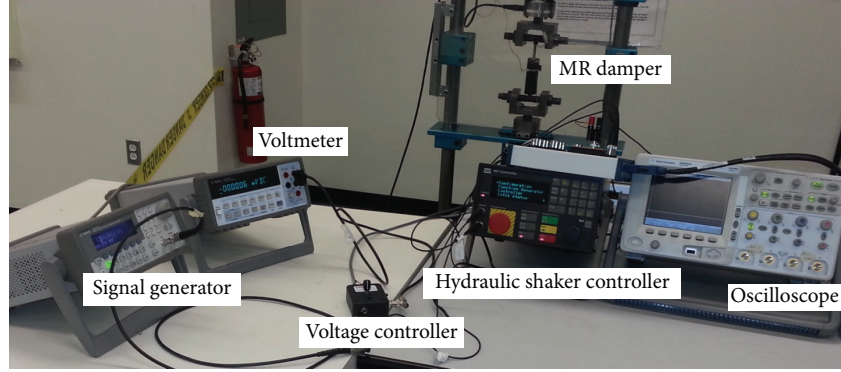


FIGURE 2: Experimental setup.

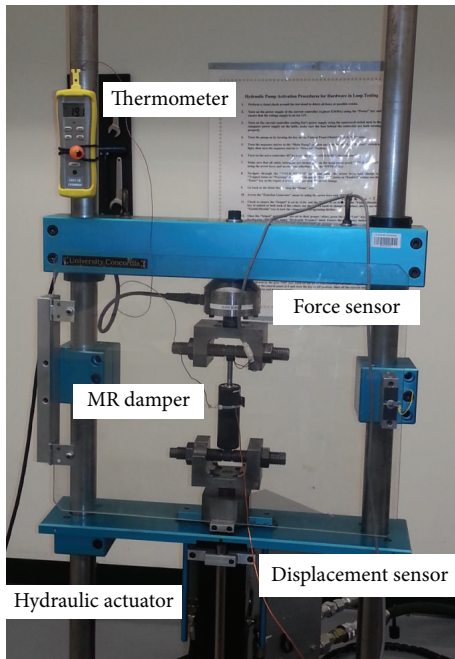


FIGURE 3: MR damper and hydraulic shaker.

1.5 Hz to 5 Hz in 0.5 (Hz) interval at zero current, respectively. The objective function is defined as the error between the experimental and mathematical model as presented in (8). Linear constraints are the lower bound and upper bound and nonlinear constraint is as defined in (11). The quantities of lower bound and upper bound are assigned based on the sensitivity of the objective function to the design variables. The contour plot of an optimization algorithm in Figure 4 presents the sensitivity of objective function to design variables.

The range of design variables in Figure 4 is considered to be $\pm 40\%$ from the identified parameters based on 2.5 Hz (first optimization step), in order to identify viscosity parameters of MR damper at frequency of 1.5 Hz. The lower bound and upper bound for data sets in other frequencies (in the range of 1.5 Hz to 5 Hz) are considered with $\pm 20\%$ variation with

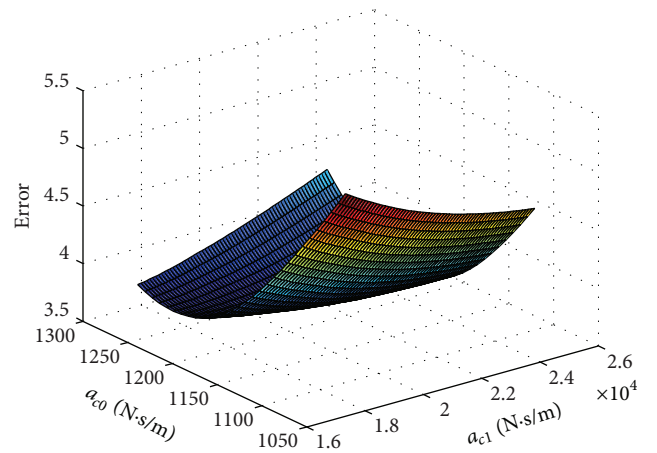


FIGURE 4: Sensitivity of objective function to variation of viscosity parameters of MR damper in 1.5 Hz.

respect to the assigned viscosities from previous data set. For example, the lower bound and upper bound of optimized algorithm for 2 Hz are defined based on $\pm 20\%$ from the identified $C_{mr1}(\Delta Z, \Delta \dot{Z})$ and $C_{mr0}(\Delta Z, \Delta \dot{Z})$ for 1.5 Hz.

Figure 4 shows that the variation of the objective function with respect to the design variable is convex, which guarantees that a global optimum point will be reached in the process of identification. It should be noted that the sensitivity of objective function with respect to viscosity parameters in 20% variation for all data sets is studied and convexity in the feasible region is checked.

4.1. Sequential Quadratic Programming Technique. The Sequential Quadratic Programming is a methodology for nonlinear optimization problems considering nonlinear equality and inequality constraints. The SQP is an iterative procedure based on Quadratic Programming (QP) to solve QP subproblems and to define new iterations [12]. The QP should be solved to satisfy feasibility of problem considering local properties of current iteration. Objective functions

and linear and nonlinear constraints of QP subproblems are defined in the following [12]:

$$\begin{aligned} f(x) &\approx \nabla f(x^k)^T (x - x^k) + \frac{1}{2} (x - x^k)^T Hf(x^k) (x - x^k), \\ h(x^k) + \nabla h(x^k)^T (x - x^k) &= 0, \\ g(x^k) + \nabla g(x^k)^T (x - x^k) &\leq 0. \end{aligned} \quad (12)$$

In nonlinear optimization problems, the SQP method may find one of the extremum points which is near the selected initial point. Therefore, the sensitivity of the initial point with respect to the optimized parameters should be studied. The presented objective function is nonlinear and it is not robust in variation of initial point. Therefore, the GA is employed to assign the initial point in SQP method which makes up the hybrid GA-SQP optimization algorithm.

4.2. Genetic Algorithm Optimization Technique. The GA is a multivariable optimization method for solving linear, nonlinear, discrete, continuous, differentiable, and nondifferentiable constrained problems by using stochastic search algorithms [12–15]. The Genetic Algorithms are a random search based method which can avoid stopping in local optimum point. However, using GA the globality of the optimum point cannot be proved or guaranteed. The optimization problem for identifying the MR damper parameters is highly dependent on the initial point. The combination of GA and SQP can solve the problem by using initial point obtained through GA based on random search in SQP algorithm [16, 17]. The hybrid of GA-SQP approaches can reach global optimum point. But, the globality cannot be proved mathematically. The GA operates based on random point selection in random generation [14]. Therefore, running the same algorithm each time may give different optimal points [14]. As a result, by increasing the number of populations and repeating the same algorithm, the relaxation of the obtained initial points is studied. The GA is designed based on the presented objective function (8) and constraints (10).

5. Results and Discussions

Two optimization approaches are employed to investigate the variation of viscosity of MR fluid with frequency. In the first algorithm, the parameters of MR damper are identified for 2.5 Hz and zero current. For the second part, the variations a_{c0} and a_{c1} are identified for the frequencies in the range of 1.5 Hz to 5 Hz at step of 0.5 Hz in eight suboptimization algorithms.

5.1. Parameter Identification for Constant Frequency. The parameters of Spencer MR damper model are identified using hybrid optimization of GA-SQP. The identified parameters are presented in Table 2 based on experimental data at 2.5 Hz and zero current. The initial values for SQP are assigned using GA. The GA algorithms are used for different number of populations from 80 to 360 in the interval of 80. Moreover,

TABLE 2: Identified parameters of MR damper in 2.5 Hz and zero current.

Parameter	Quantity of hybrid optimization (GA-SQP)
K_{mr0}	3361.58 (N/m)
K_{mr1}	420 (N/m)
a_{c0}	1176 (Ns/m)
a_{c1}	21973.50 (Ns/m)
a_{α}	6515.13 (N/m)
A	87
β	307269.41 (1/m ²)
γ	182842.99 (1/m ²)
n	2
Z_0	0.01225 (m)

to study the result of relaxation, the algorithms are repeated ten times for each population. The presented results in Table 2 are obtained based on 240 numbers of populations resulting in minimum error. The identified parameters in this table are used for second step optimization in order to find the viscosity variation of MR damper at different frequencies.

Figures 5 and 6 show the force velocity and force versus time, respectively. The objective function is defined as the absolute value of the error between the experimental measured force and the generated force in mathematical model. Figure 6 demonstrates that the mathematical model is fitted by experimental data with 2.85% error. However, due to the neglected effect of the velocity in objective function (7), the experimental and mathematical force-velocity curves have some discrepancies in Figure 5.

5.2. Parameter Identification for Variable Frequency. The variation of a_{c0} and a_{c1} for the frequencies in the range of 1.5 Hz to 5 Hz in interval 0.5 Hz is calculated by solving eight suboptimization problems. The optimization objective is to minimize the error between the experimental and mathematical data. The constraints are defined in the range of $\pm 40\%$ variation from the optimized values of a_{c0} and a_{c1} for each frequency from the assigned viscosities in 2.5 Hz. The other linear constraints are assigned considering $\pm 20\%$ variation with respect to the assigned viscosities in the previous step. The sensitivity of the objective function to a_{c0} and a_{c1} in the feasible search region is examined to guarantee the convexity of the function in feasible range defined by lower bound and upper bound. The suboptimization problems are solved using hybrid optimization technique.

Figures 7 and 8 show the variation of a_{c0} and a_{c1} for different frequencies by blue points. The variation of a_{c0} is modeled by an exponential function which can be used for extrapolation. Therefore, the variation of a_{c0} is defined as a function of frequency in (13). The frequency can be measured by displacement sensor, and the relation between velocity, displacement, and frequency is presented in (15).

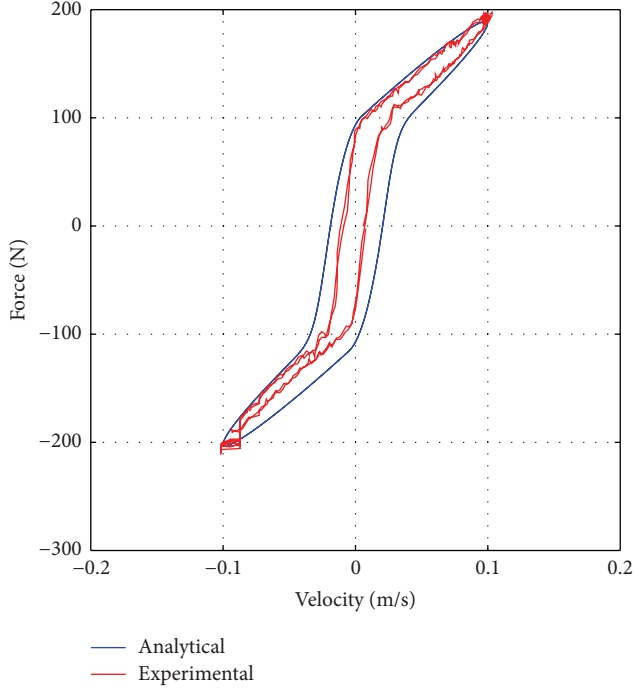


FIGURE 5: Force-velocity hysteresis in 2.5 Hz and zero current.

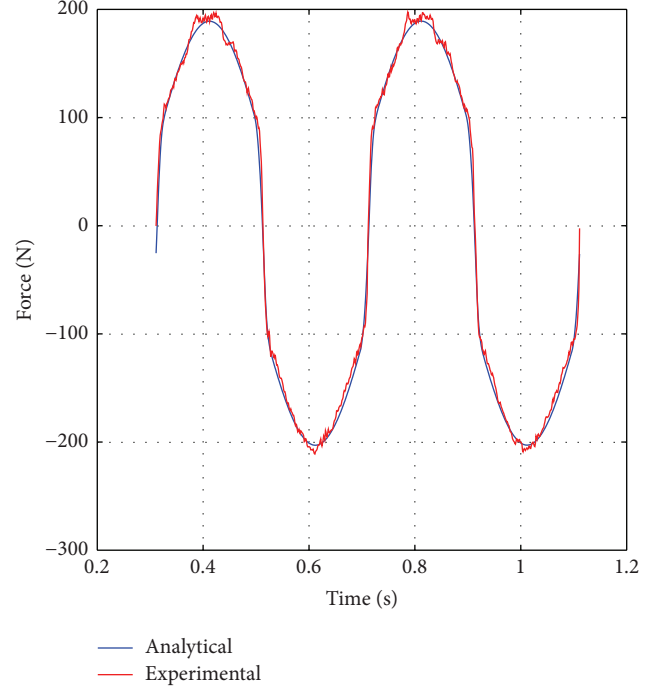


FIGURE 6: Experimental and mathematical MR damper force in 2.5 Hz and zero current.

The variation of a_{c1} with frequency in Figure 8 is modeled using the second order Gaussian function in (14):

$$a_{c0}(\omega) = 1410.71\omega^{-0.102} - 0.6182, \quad (13)$$

$$a_{c1}(\omega) = 7087e^{((4.282-\omega)/1.197)^2} + 18520e^{((1.783-\omega)/3.25)^2}, \quad (14)$$

$$\omega(\Delta Z, \Delta \dot{Z}) = \frac{\Delta \dot{Z}}{\pi \Delta Z}. \quad (15)$$

Figure 7 shows that parameter a_{c0} is sensitive in the low frequency region and becomes constant at high frequency, whereas parameter a_{c1} in Figure 8 is constant at low frequency and becomes variable in the high frequency region.

In order to compare the effect of frequency dependent model and frequency independent model (existing model), the error between the experimental and analytical models is presented in Table 3 for seven frequencies. The parameters of the frequency independent model are identified at frequency of 2.5 Hz. Therefore, the errors of both frequency independent and frequency dependent models for data samples near 2.5 Hz are close to each other. However, at high frequencies, the difference becomes significant. For example, for 5 Hz data sample, the error is decreased by 1.1%. The extrapolation of viscosity variation in Figure 8 shows that the difference at high frequencies would be significant.

Figure 9 shows that the existing independent frequency model has overestimation in modeling for hysteresis of MR damper in comparison with the proposed frequency dependent model. The main objective in modelling the MR damper is to simulate MR damper force at different frequencies of excitation and current. It shows that the proposed frequency dependent model improves the accuracy of force simulation.

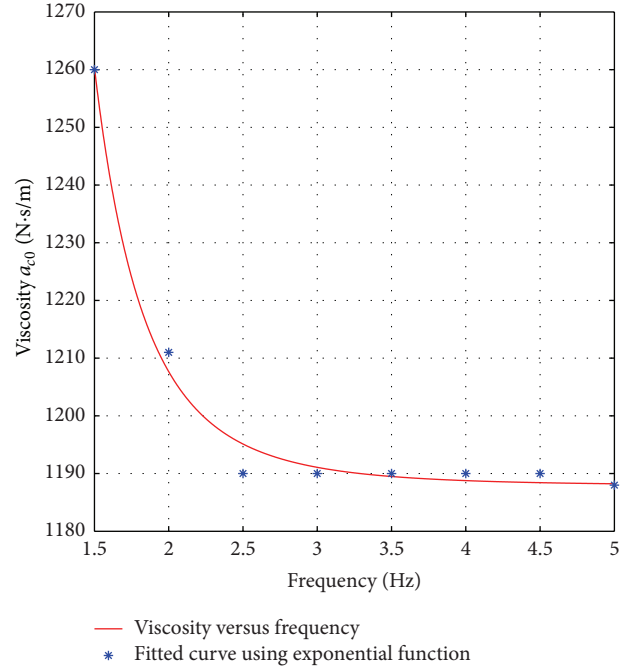


FIGURE 7: Variation MR damper viscosity a_{c0} versus frequency.

Moreover, the proposed model is in agreement with the force simulation in variable frequency and operating conditions of the MR damper.

TABLE 3: Comparison between frequency dependent and original Spencer model.

Frequency (Hz)	1.5	2	3	3.5	4	4.5	5
Error of frequency dependent model	3.13%	2.61%	2.35%	2.57%	2.63%	3.35%	3.75%
Error of frequency independent model	3.64%	2.67%	2.36%	2.58%	2.81%	3.95%	4.85%

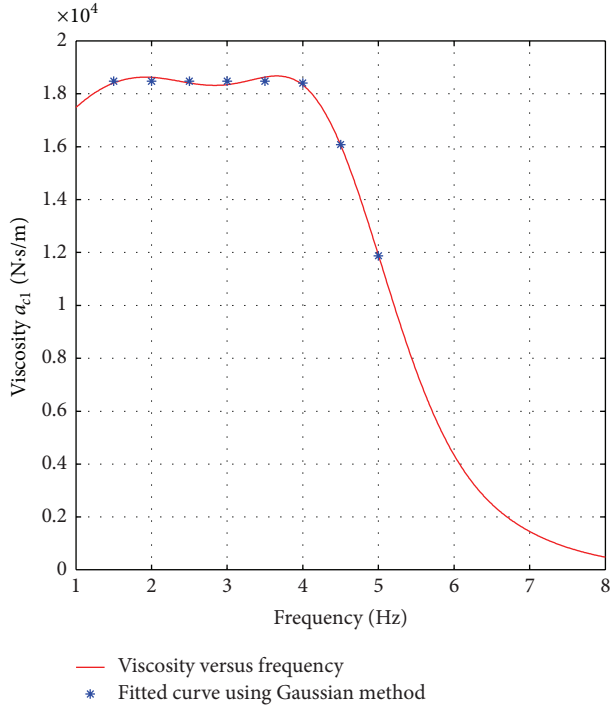
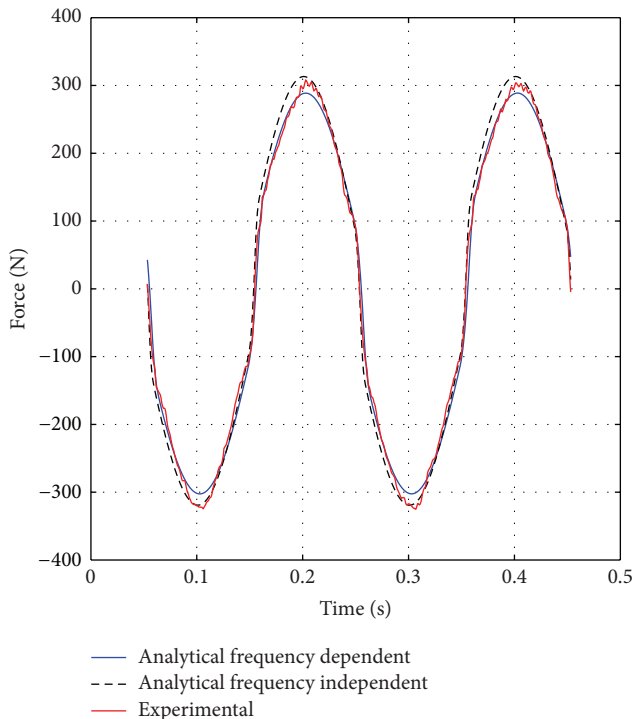
FIGURE 8: Variation MR damper viscosity a_{c1} versus frequency.

FIGURE 9: MR damper force in frequency 5 Hz and zero current.

6. Conclusions

In this study, the variation of MR damper viscosity at different frequencies has been studied using analytical and experimental approaches. The hybrid GA-SQP optimization techniques are used to identify the parameters of the MR damper based on experimental data. The variation of MR damper viscosity with frequency is studied for frequency range from 1.5 Hz to 5 Hz at 0.5 Hz interval using hybrid GA-SQP technique. A mathematical MR frequency dependent model is proposed based on Spencer MR damper model where the viscosity of MR damper is modeled by exponential and Gaussian functions. The results confirm that the frequency dependent MR damper model improves the accuracy of the model in force simulation at high frequency region and shows consistency in force simulation as well. The proposed MR damper model can be used in application of impact control and aircraft landing gear in which these operational conditions need high precision in high frequency region.

Conflict of Interests

The authors declare that there is no conflict of interests regarding the publication of this paper.

References

- [1] B. F. Spencer Jr., S. J. Dyke, M. K. Sain, and J. D. Carlson, "Phenomenological model for magnetorheological dampers," *Journal of Engineering Mechanics*, vol. 123, no. 3, pp. 230–238, 1997.
- [2] D. A. Brooks, "Design and development of flow based electro-rheological devices," *International Journal of Modern Physics B*, vol. 6, no. 15-16, pp. 2705–2730, 1992.
- [3] F. Mohammadi and R. Sedaghati, "Dynamic mechanical properties of an electrorheological fluid under large-amplitude oscillatory shear strain," *Journal of Intelligent Material Systems and Structures*, vol. 23, no. 10, pp. 1093–1105, 2012.
- [4] S. M. Savaresi, S. Bittanti, and M. Montiglio, "Identification of semi-physical and black-box non-linear models: the case of MR-dampers for vehicles control," *Automatica*, vol. 41, no. 1, pp. 113–127, 2005.
- [5] I. H. Shames and F. A. Cozzarelli, *Elastic and Inelastic Stress Analysis*, Prentice-Hall, Englewood Cliffs, NJ, USA, 1992.
- [6] D. R. Gamota and F. E. Filisko, "Dynamic mechanical studies of electrorheological materials: moderate frequencies," *Journal of Rheology*, vol. 35, no. 3, pp. 399–425, 1991.
- [7] Y.-K. Wen, "Method of random vibration of hysteretic systems," *ASCE Journal of Engineering Mechanics Division*, vol. 102, no. 2, pp. 249–263, 1976.
- [8] F. Donado, U. Sandoval, and J. L. Carrillo, "Viscosity enhancement in dilute magnetorheological fluids through magnetic

- perturbations,” *Revista Mexicana de Fisica*, vol. 57, no. 5, pp. 426–434, 2011.
- [9] N. M. Kwok, Q. P. Ha, M. T. Nguyen, J. Li, and B. Samali, “Bouc-Wen model parameter identification for a MR fluid damper using computationally efficient GA,” *ISA Transactions*, vol. 46, no. 2, pp. 167–179, 2007.
- [10] A. A. Gharapurkar, A. F. Jahromi, R. B. Bhat, and W.-F. Xie, “Semi-active control of aircraft landing gear system using H-infinity control approach,” in *Proceedings of the 2nd IEEE International Conference on Connected Vehicles and Expo (ICCVE '13)*, pp. 679–686, December 2013.
- [11] W. H. Liao and C. Y. Lai, “Harmonic analysis of a magnetorheological damper for vibration control,” *Smart Materials and Structures*, vol. 11, no. 2, pp. 288–296, 2002.
- [12] P. T. Boggs and J. W. Tolle, “Sequential quadratic programming,” in *Acta Numerica*, pp. 1–51, 1995.
- [13] J. H. Holland, *Adaptation in Natural and Artificial Systems*, MIT Press/Bradford Books Edition, Cambridge, Mass, USA, 1st edition, 1992.
- [14] J. S. Arora, “Optimum design concepts: optimality conditions,” in *Introduction to Optimum Design*, chapter 4, Academic Press, New York, NY, USA, 2nd edition, 2004.
- [15] M. Bagheri, A. A. Jafari, and M. Sadeghifar, “Multi-objective optimization of ring stiffened cylindrical shells using a genetic algorithm,” *Journal of Sound and Vibration*, vol. 330, no. 3, pp. 374–384, 2011.
- [16] A. F. Jahromi, W. F. Xie, and R. B. Bhat, “Ride control of passenger cars with semiactive suspension system using a linear quadratic regulator and hybrid optimization algorithm,” in *Proceedings of the International Conference on Aerospace, Mechanical, Automotive and Materials Engineering (ICAMAME '12)*, pp. 1083–1089, July 2012.
- [17] A. Hadadian, R. Sedaghati, and E. Esmailzadeh, “Design optimization of magnetorheological fluid valves using response surface method,” *Journal of Intelligent Material Systems and Structures*, vol. 25, no. 11, pp. 1352–1371, 2013.